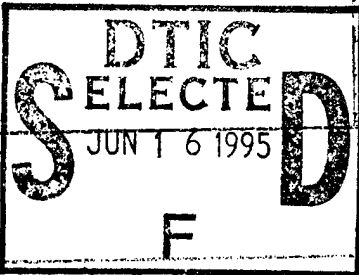


REPORT DOCUMENTATION PAGE

Form Approved
OMB No. 0704-0188

Public reporting burden for this collection of information is estimated to average 1 hour per response, including the time for reviewing instructions, searching existing data sources, gathering and maintaining the data needed, and completing and reviewing the collection of information. Send comments regarding this burden estimate or any other aspect of this collection of information, including suggestions for reducing this burden, to Washington Headquarters Services, Directorate for Information Operations and Reports, 1215 Jefferson Davis Highway, Suite 1204, Arlington, VA 22202-4302, and to the Office of Management and Budget, Paperwork Reduction Project (0704-0188), Washington, DC 20503.

1. AGENCY USE ONLY (Leave blank)		2. REPORT DATE	3. REPORT TYPE AND DATES COVERED FINAL REPORT 01 Feb 94 - 31 Jan 95		
4. TITLE AND SUBTITLE High Efficiency Vacuum and Plasma-Filled Backward-Wave Oscillators: A Critical Evaluation			5. FUNDING NUMBERS 61102F 2301/ES		
6. AUTHOR(S) Professor Schamiloglu					
7. PERFORMING ORGANIZATION NAME(S) AND ADDRESS(ES) Department of Electrical and Computer Engineering University of New Mexico Albuquerque, NM 87131			8. PERFORMING ORGANIZATION REPORT NUMBER AFOSR-TR 93-0409		
9. SPONSORING/MONITORING AGENCY NAME(S) AND ADDRESS(ES) AFOSR/NE 110 Duncan Avenue Suite B115 Bolling AFB DC 20332-0001			10. SPONSORING/MONITORING AGENCY REPORT NUMBER F49620-94-1-0087		
11. SUPPLEMENTARY NOTES					
12. DISTRIBUTION STATEMENT					
APPROVED FOR PUBLIC RELEASE: DISTRIBUTION UNLIMITED					
13. ABSTRACT (Maximum 200 words) This report describes the results of research during the first year of a proposed three year project to provide a critical evaluation of the attributes of plasma-filled high power backward-wave oscillators when compared with high efficiency vacuum backward-wave oscillators. Since the direction of the program at the University of New Mexico was altered by the newly initiated MURI triservices funding, only about one third of the originally proposed tasks were accomplished. Nevertheless, important new results have been obtained and will continue to be investigated under the auspices of the MURI program. were: DTIC QUALITY INSPECTED 3					
14. SUBJECT TERMS			15. NUMBER OF PAGES		
			16. PRICE CODE		
17. SECURITY CLASSIFICATION OF REPORT UNCLASSIFIED			18. SECURITY CLASSIFICATION OF THIS PAGE UNCLASSIFIED	19. SECURITY CLASSIFICATION OF ABSTRACT UNCLASSIFIED	20. LIMITATION OF ABSTRACT UNCLASSIFIED



The University of New Mexico

Department of Electrical and
Computer Engineering
Room 110, EECE Building
Albuquerque, NM 87131-1381
(505) 277-2436

**Final Technical Report Submitted to AFOSR:
High Efficiency Vacuum and Plasma-Filled Backward-Wave Oscillators:
a Critical Evaluation
(Grant AFOSR #F49620-94-1-0087)**

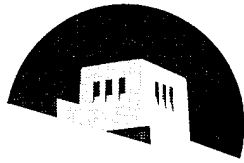
24 May 1995

Edl Schamiloglu, Associate Professor, Principal Investigator
Charles Fleddermann & John Gahl, Co-PIs
Pulsed Power & Plasma Science Laboratory

Department of Electrical and Computer Engineering
University of New Mexico
Albuquerque, NM 87131

DTIC QUALITY INSPECTED 3

19950614 058



The University of New Mexico

Department of Electrical and
Computer Engineering
Room 110, EECE Building
Albuquerque, NM 87131-1381
(505) 277-2436

**Final Technical Report Submitted to AFOSR:
High Efficiency Vacuum and Plasma-Filled Backward-Wave Oscillators:
a Critical Evaluation
(Grant AFOSR #F49620-94-1-0087)**

24 May 1995

Edl Schamiloglu, Associate Professor, Principal Investigator
Charles Fleddermann & John Gahl, Co-PIs
Pulsed Power & Plasma Science Laboratory

Department of Electrical and Computer Engineering
University of New Mexico
Albuquerque, NM 87131

Table of Contents

Section I. Executive Summary	3
Section II. Sinus-6 High Power BWO Theory and Experiments	6
Section III. Long Pulse Vacuum BWO	7
Section IV. Ferroelectric Cathode Development.....	9
Section V. Displacement Field Diagnostics and Calibrations	10
Section VI. Bibliography of Presentations and Papers During Grant Period.....	34
Section VII. References	36
Appendix A. Status of Personnel	37
Appendix B. Overview Paper Presented at AGARD Panel.....	38
Appendix C. Papers in Print Pertaining to Sinus-6 BWO.....	39
Appendix D. Paper in Print Pertaining to Long Pulse BWO.....	40
Appendix E. Papers in Print Pertaining to Ferroelectric Cathodes	41
Appendix F. Paper in Print Pertaining to Suppression of Vacuum Breakdown...	42

Accession For	
NTIS	CRA&I <input checked="checked" type="checkbox"/>
DTIC	IAB <input type="checkbox"/>
Unannounced	<input type="checkbox"/>
Justification	
By	
Distribution /	
Availability Codes	
Dist	Avail and/or Special
A-1	

I. Executive Summary

This report describes the results of research during the first year of a proposed three year project to provide a critical evaluation of the attributes of plasma-filled high power backward-wave oscillators when compared with high efficiency vacuum backward-wave oscillators. Since the direction of the program at the University of New Mexico was altered by the newly initiated MURI triservices funding, only about one third of the originally proposed tasks were accomplished. Nevertheless, important new results have been obtained and will continue to be investigated under the auspices of the MURI program. The important results achieved under this grant were:

Milestones Achieved

1. A clear exposition of the physical reasons for efficiency enhancement of high power vacuum backward-wave oscillators using nonuniform slow wave structures. Experiments and particle-in-cell simulations confirm that significant prebunching of the electron beam is caused by the zeroth harmonic of the waveguide mode. A tube designed to exploit this phenomenon can yield significant enhancement in microwave conversion efficiency.
2. Long pulse vacuum experiments confirm previous observations of the termination of microwaves after about 100 ns. In addition, TE_{11} -like modes have been observed instead of the expected TM_{01} modes.
3. Repeatable electron emission from $(Pb,La)(Zr,Ti)O_3$ ferroelectric cathodes using a direct-current reset has been observed. An application to patent this procedure has been submitted.
4. Thin-film metal and metal oxide coatings sputter-deposited onto the cathode electrode of a parallel-plate quasi-dc high voltage gap were found to suppress electron emission. These coatings may have applications in components of high power microwave tubes to achieve longer pulse operation.

5. *In situ* displacement field diagnostics were developed and calibrated for use in our high power backward-wave oscillator tubes.

Interactions

A hallmark of this research project is the continued interaction and collaboration with other groups. The following list represents scientists with whom significant active interaction has occurred during the course of this research. The subject of the interaction is also presented.

- (i) Sandia National Laboratories (Dr. Ray Lemke)—theoretical aspects of high efficiency BWO physics. Computational support. Dr. Lemke was also a committee member of one of the graduate students (Larald Moreland).
- (ii) Air Force Phillips Laboratory (Drs. Kyle Hendricks and Tom Spencer)—joint measurements of the output of the Sinus-6 backward-wave oscillator experiments. Dr. Hendricks is also a committee member of one of the graduate students (Tommy Cavazos).
- (iii) High Current Electronics Institute, Tomsk, Russia (Drs. Sergei Korovin, Vladislav Rostov, Sergei Polevin, Igor Pegel, and Albert Roitman)—experiments and theory of high efficiency vacuum backward-wave oscillators. Drs. Pegel and Roitman were visiting scientists in our laboratory during the 1993-1994 academic year under the auspices of funding from the U.S. National Research Council and the William and Mary Greve Foundation.
- (iv) Institute of Electrophysics, Ekaterinburg, Russia (Academician Gennady Mesyats) —ferroelectric cathodes: theory and experiment. Academician Mesyats visited our laboratory in the Summer of 1994 under the auspices of funding from the William and Mary Greve Foundation.
- (v) Mission Research Corporation, Newington, VA (Dr. Bruce Goplen). Our laboratory is now an official member of the MAGIC Users Group. Dr. Goplen presented a one week short course on the usage of MAGIC. This course was also attended by researchers from the Air Force Phillips Laboratory.

Finally, in response to a request from the Air Force Phillips Laboratory, Professors Gahl and Schamiloglu presented a Spring 1995 semester graduate-level University of

New Mexico course on High Power Microwaves. This was delivered by television to the Phillips Laboratory where 27 students were registered.

Outline of this Final Technical Report

Since a considerable number of papers have appeared in the literature describing the results of this research effort, the subsequent sections will only summarize the status of the projects. Section II will present an overview of the Sinus-6 experiments and theoretical accomplishments. Section III will summarize the status of the long pulse vacuum backward-wave oscillator. Section IV will describe the status of the ferroelectric cathode work. Section V describes the displacement field diagnostics and calibrations. Section VI presents a bibliography of all presentations and papers produced during the grant period. References for this report are contained in Sec. VII. Appendix A presents information on the status of faculty, staff and students funded by this grant. Appendix B contains a copy of a paper presented at the NATO AGARD Electromagnetic Wave Propagation Panel Symposium on High Power Microwaves (Ottawa, Canada, 2-5 May, 1994). Appendix C presents copies of papers pertaining to the Sinus-6 microwave experiments. Appendix D presents a copy of a paper pertaining to the long pulse microwave experiments. Appendix E presents copies of papers pertaining to the ferroelectric cathode work, and Appendix F presents a copy of a paper pertaining to the suppression of vacuum breakdown.

Sinus-6 High Power BWO Theory and Experiments

Significant advances have been made in the understanding of short pulse, high power, vacuum backward-wave oscillator (BWO) operation.^{1,2} A systematic study of high power BWOs was performed using the Sinus-6 repetitively pulsed relativistic electron beam accelerator. Peak output power of up to 550 MW was measured in a frequency range of 9.2 to 9.8 GHz with pulse lengths up to 10 ns. The experimental results were compared with numerical simulations using TWOQUICK, a 2.5 D, relativistic, fully electromagnetic, particle-in-cell code. It was observed that a significant increase in microwave efficiency can be obtained by using a BWO with a spatially varying coupling impedance instead of the traditional uniform distribution. Based on experiments using variations of a two stage nonuniform amplitude BWO in conjunction with TWOQUICK simulations, it was determined that the efficiency enhancement can be attributed to the prebunching of the electron beam.²

An important factor that affects BWO performance is the ratio of electron beam current to start current. The start current is a function of length for a given slow wave structure (SWS) geometry. Experiments were performed with varying SWS lengths to determine the changes in BWO performance with increasing ratios of beam current to start current. The decrease in BWO efficiency attributed to multifrequency operation at higher beam currents was not observed because of the short pulse lengths in the experiment.¹

The effects of end reflections and the influence of the forward traveling wave on BWO performance were explored through a set of experiments where the reflection characteristics at both ends of the the SWS were changed by introducing sections of smooth-walled waveguide. It was found that the BWO microwave conversion efficiency and the operating frequency varied periodically as a function of the length of sections added. The role of the forward propagating asynchronous harmonic becomes apparent as the reflection coefficient at the beginning of the SWS is changed. This is supported by theoretical calculations of the electron bunching and electric fields within the SWS.¹

The results of the short pulse high efficiency vacuum BWO work suggest a new method to change the BWO operating frequency by over 100 MHz while maintaining constant output power for constant beam parameters.¹

III. Long Pulse Vacuum BWO

During the past year, work on the UNM long pulse BWO experiment was directed towards diagnosing and correcting breakdown problems within the electron beam diode. In addition, considerable effort was invested towards developing reliable electrical diagnostics. The accelerator used is a modified Physics International Pulserad PI-110A. An 11-stage Marx bank with an energy storage capacity of 2.75 kJ is used as the main energy store and initial pulse forming device. The Blumlein transmission line originally contained in the accelerator was replaced by an LC filter network to provide long pulse capabilities. Initial experiments with the long pulse accelerator indicated considerable damage to the grating rings in the diode. After repairing the diode stack, shunt resistors were placed in the oil section to decrease current flow to the $A - K$ gap. Current for a matched load (76Ω) is now 7.5 kA, bringing the parameters of this accelerator very similar to the parameters of the Sinus-6 accelerator, although at considerably longer pulse lengths.

MAGIC simulations were performed of the injector region of this accelerator. The simulations revealed a component of back-streaming electrons which would impinge upon a capacitive voltage monitor. A new capacitive voltage divider was built and installed in a region impervious to electrons. The new monitor provides a reliable signal.

A new self-integrating Rogowski coil was developed for use as a current monitor. This was positioned after the slow wave structure and right before the electron beam dump. A new differentially monitored, counterwound \dot{B} coil was installed near the cathode for electron beam current monitoring.

A microwave diagnostic setup identical to that used on the Sinus-6 experiments was constructed. The microwave signal picked up by a small receiving antenna located in the far-field of the BWO's conical horn antenna is transmitted to a screen room where it is split using a power divider. Part of the signal is detected by a crystal diode and the other part is sent to be heterodyned with a local oscillator for precise output frequency determination.

To help accomodate long pulse microwave generation from a BWO using this driver a new electron beam dump and additional length of guide magnetic field were installed.

Vacuum microwave generation experiments have begun. Predominantly TE_{11} -like radiation is observed to buildup for about 100 ns before rapid termination. Occasional frequency “hopping” is observed as well. No conclusion can be drawn at this point. These experiments are continuing under funding from the triservices MURI program.

IV. Ferroelectric Cathode Development

During the course of this year's investigations we tested bulk 9/65/35 PLZT materials which exhibited "soft" ferroelectric behavior. (The ferroelectric test stand set-up is described in the papers in Appendix E.) The emission current (averaged over the pulse) was on the order of 100 mA and the charge emitted per shot was typically 40 nC. The emission life was limited by breakage of the ceramic material that was caused by piezoelectric forces.

The experiment was configured to reduce the stress on the ceramic and thicker bulk materials of PZT were subsequently tested. No emission was recorded with this configuration. Two problems have been identified: i) we have been unsuccessful in reversing the polarization in the PZT samples, and ii) because of the the strong piezoelectric coupling of this material, the occurrence of fractures has increased.

The experiment is presently being re-engineered to correct the above problems. A new ferroelectric holder is being built with a spring loaded contact. This feature will allow a degree of freedom in the axial direction to prevent the buildup of mechanical stresses. We are also using disk shaped ferroelectric samples instead of square ones. It is believed that the lateral strain in a square-shaped sample produces excessive stress at the corners.

Presently we are studying emission from three classes of polar dielectric ceramic materials: soft ferroelectric (8/65/35 PLZT), hard ferroelectric (PZT), and antiferroelectric (2/95/5). The emission area of these samples will be gridded using material with two different transparencies (20% and 50%) and we wil investigate the possibility of extracting electrons through solid metal electrodes 500-1000 Å-thick. Thin film ferroelectric materials (4-10 μm) will also be studied.

This program will also continue under the auspices of the MURI program.

V. Displacement Field Diagnostics and Calibrations

Attached are two memoranda in their entirety which describe the accomplishments on this task.

The University of New Mexico

EECE Department
Room 110, EECE Building
Albuquerque, NM 87131

Memorandum

To: UNM HPM Group
From: Mike Haworth *MH*
Date: 7/28/94
Subject: Calibration procedure for Burkhart-type D-dot probes used to measure TM_{01} -mode power in evacuated cylindrical waveguide.

This note describes how the E-field (or D-dot) probe technique of Burkhart [1] can be used to measure the power flow of TM_{01} waves in evacuated cylindrical waveguide. A Burkhart-type D-dot probe is simply a section of open-ended semi-rigid cable which is inserted no more than flush with the waveguide wall and in a direction parallel to the microwave electric field. The TM_{01} power is determined by measuring the power coupled into the D-dot probe, which is related to the magnitude of the radial E-field component of the TM_{01} mode, and hence the power, at the probe.

For our application, a short piece of 0.141-in. semi-rigid cable was used as the D-dot probe. The theoretical basis of this diagnostic technique is presented in Sect. I., the calibration procedure is described in Sect. II., and the D-dot probe measurement procedure is summarized in Sect. III. Use of this probe on the Sinus-6 BWO is imminent.

I. D-Dot Probe Theory

A. Power coupled into D-dot probe

Since the 0.141 cable diameter is a small fraction of the wavelength of interest, the power coupled from the TM_{01} mode in the cylindrical guide into the TEM mode of the coax cable forming the D-dot probe can be calculated using the quasistatic approximation [1]. Thus, the charge induced on the center conductor of the coax is found from Gauss' law to be

$$Q(t) = \epsilon_0 K E_{D\text{-dot}}(t) \quad (1)$$

where K is the effective area of the center conductor and $E_{D\text{-dot}}$ is the peak value of the E-field at the probe position. For a sinusoidally varying E-field, the power coupled into the probe is given by [1]

$$\begin{aligned}
 P_{D-dot} &= \frac{1}{2} |I|^2 Z_0 \\
 &= \frac{1}{2} |\dot{Q}|^2 Z_0 \\
 &= \frac{Z_0}{2} (\omega \epsilon_0 K E_{D-dot})^2
 \end{aligned} \tag{2}$$

where Z_0 is the characteristic impedance of the coax (i.e., 50Ω for 0.141 cable). Eq. (2) shows that if K is known through a calibration procedure, then measuring the power level coupled into the probe determines the E-field at the probe. The next step is to relate the E-field at the probe to the power in the TM_{01} mode propagating in the cylindrical guide.

B. Cylindrical waveguide power flow in the TM_{01} mode

The power flow in the TM_{01} mode for a cylindrical waveguide is given by

$$\begin{aligned}
 P_{01} &= \frac{1}{2} \text{Re} \left[\iint_S (\vec{E} \times \vec{H}^*) \cdot d\vec{S} \right] \\
 &= \pi \text{Re} \left[\int_0^{r_g} (\vec{E}_{r,01} \times \vec{H}_{\theta,01}^*) \cdot \hat{z} r dr \right]
 \end{aligned} \tag{3}$$

where r_g is the guide radius and the peak values of the field components are [2]

$$\begin{aligned}
 E_{r,01}(r) &= j A_{01} \frac{\beta_{01} x_{01}}{r_g k_{c,01}^2} J_1 \left(\frac{x_{01} r}{r_g} \right) \\
 H_{\theta,01}(r) &= j A_{01} \frac{x_{01} k_0}{r_g k_{c,01}^2 \eta} J_1 \left(\frac{x_{01} r}{r_g} \right)
 \end{aligned} \tag{4}$$

In the above equations, A_{01} is a normalization constant, x_{01} is the first zero of the zero-order Bessel function, $k_0 = \omega/c$ is the free-space wave number (or wave propagation constant), $k_{c,01} = x_{01}/r_g$ is the cutoff wave number, $\beta_{01} = (k_0^2 - k_{c,01}^2)^{1/2}$ is the guide wave

number, and $\eta = (\mu_0/\epsilon_0)^{1/2} \approx 377 \Omega$ is the impedance of free space. Using Eqs. (4) in Eq. (3), the TM_{01} mode power is found to be [3]

$$P_{01} = |A_{01}|^2 \frac{\pi k_0 \beta_{01} r_g^2}{2k_{c,01}^2 \eta} [J_1(x_{01})]^2 \quad (5)$$

The unknown normalization constant, A_{01} , can be evaluated in terms of the radial E-field at the wall radius. From the first of Eqs. (4), you get

$$A_{01} = -j \frac{r_g k_{c,01}^2}{\beta_{01} x_{01} J_1(x_{01})} E_{r,01}(r = r_g) \quad (6)$$

Finally, using the results from Eq. (6) in Eq. (5), the TM_{01} power is given by [3,4]

$$P_{01} = \frac{\pi}{2} \frac{k_0 r_g^2}{\beta_{01} \eta} |E_{r,01}(r_g)|^2 \quad (7)$$

In an actual experiment, $E_{r,01}(r_g)$ is calculated from the measured D-dot probe power via Eq. (2). Thus, for the case of the Sinus-6 BWO output guide with an I.D. of 1.965-in., the TM_{01} power is related to the measured D-dot probe power by

$$\begin{aligned} \frac{P_{01}}{P_{D-dot}} &= \frac{\pi}{Z_0} \left\{ \eta^2 \left[1 - \left(\frac{x_{01}}{r_g k_0} \right)^2 \right] \right\}^{-1/2} \left(\frac{r_g}{\omega \epsilon_0 K} \right)^2 \\ &= \frac{3.356 \times 10^{13}}{K^2 f^2} \left(1 - \frac{2.114 \times 10^{19}}{f^2} \right)^{-1/2} \end{aligned} \quad (8)$$

with f in Hz and K in m^2 . In order to use Eq. (8) to deduce the power in the TM_{01} mode, you must independently measure the frequency of the TM_{01} wave propagating down the guide, plus you must measure the effective area, K , of the probe. A method to determine this latter quantity is described in the next section.

Note that Eq. (8) assumes that the output guide is perfectly terminated, i.e. there is no reflected power. A D-dot probe has no directivity, but simply measures the net power flow. Also the D-dot technique assumes that only a single mode (the TM_{01} in this case) is

present. A single D-dot measures the net E-field at its position and cannot distinguish between the field of a single mode or of a superposition of fields from several modes.

II. Calibration Procedure to Determine Effective Area of D-Dot

From Eq. (2), the effective area of the center conductor of the D-dot is given by

$$K = \frac{1}{\epsilon_0 \omega E_{D-dot}} \sqrt{\frac{2P_{D-dot}}{Z_0}} \quad (9)$$

Thus, a calibration procedure is needed where the E-field at the probe is precisely known. One technique involves placing the probe flush with the outer conductor of a precision, air coax line [5]. The approach we used involves placing the probe flush with and centered on the broadwall of fundamental mode (TE₁₀) rectangular waveguide [1].

The E-field at the probe is related to the power in the TE₁₀ mode by [2]

$$\begin{aligned} E_{D-dot} &= E_{y,10}(x = a/2) \\ &= \sqrt{\frac{2k_0 \eta P_{10}}{ab\beta_{10}}} \end{aligned} \quad (10)$$

where a and b are the long and short dimensions of the guide, respectively, P₁₀ is the power in the TE₁₀ mode, and $\beta_{10} = (k_0^2 - k_{c,10}^2)^{1/2}$ is the guide wave number, with $k_{c,10} = \pi/a$ being the cutoff wave number for the TE₁₀ mode. Using the results of Eq. (10) in Eq. (9), then K is determined by

$$K = \frac{1}{\omega \epsilon_0} \sqrt{\frac{ab\beta_{10}}{k_0 Z_0 \eta}} \sqrt{\frac{P_{D-dot}}{P_{10}}} \quad (11)$$

The Sinus-6 BWO D-dot was calibrated using WR90 (X-band) waveguide, which has a = 0.90-in. and b = 0.40-in.. Power was launched into the guide from a HP83752B sweeper over the in-band frequency range (8.2-12.4 GHz) of WR90, and the reflected power from the guide as well as the power coupled into the D-dot probe was measured with a HP8757D scalar analyzer (see Fig. 1). The actual D-dot probe quantity measured is its power relative to the incident waveguide power, i.e. $\text{Atten} = 10 \log(P_{D-dot}/P_{10})$. For this case, Eq. (11) reduces to

$$K = \frac{1.798 \times 10^{10}}{f} \left[1.233 \times 10^{-8} \sqrt{1 - 4.30 \times 10^{19} / f^2} 10^{Atten/10} \right]^{1/2} \quad (12)$$

Typical analyzer data is shown in Fig. 2. This data was used in Eq. (11) to solve for K, which in turn was used in Eq. (8) to solve for P_{01}/P_{D-dot} . These results are presented in Fig. 3, where P_{01}/P_{D-dot} has been expressed as attenuation (in dB). The standing wave present in the data indicates a discontinuity approximately 4.5-in. to 7.0-in. from the open end of the probe. This is where SMA-to-N adapters were used in the calibration procedure.

The above measurements were repeated four times, with the D-dot withdrawn and replaced flush with the guide wall, in order to check its reproducibility. A linear best fit of the data yields the following formula for the Sinus-6 flush-mounted D-dot probe attenuation as a function of frequency:

$$10 \log \left(\frac{P_{01}}{P_{D-dot}} \right) [\text{dB}] = -0.962 f [\text{GHz}] + 55.4, \quad 8.2 \leq f [\text{GHz}] \leq 12.4 \quad (13)$$

An important consideration is whether the D-dot probe attenuation factor is sufficient to prevent its output connector from arcing. Field mapping and air breakdown results have shown that the Sinus-6 nonuniform BWO can generate around 500 MW of microwave power in the TM_{01} mode at 9.5 GHz [6], so the probe will develop 766 V at its output SMA connector. This should pose no problem for the 10-ns pulse from Sinus-6, but this is probably too high a voltage for pulse durations over 100 ns. The solution is to increase the D-dot probe attenuation by recessing it from the waveguide wall [1].

III. Summary

This note has shown how you can use a simple Burkhart-type D-dot probe to measure the power propagating in the TM_{01} mode in evacuated cylindrical waveguide. Although very useful just as a diagnostic to corroborate field mapping results of the radiated power, it is sometimes the only power diagnostic when using fully intercepting diagnostics such as calorimeters [7].

Use of the probe requires a two-step process given below:

- (1) Determine the effective area, K, of the D-dot center conductor by placing the probe in the center of and mounted flush (or recessed) with the broadwall of TE_{10} mode rectangular waveguide. Measure the power coupled into the probe and use Eq. (11) to calculate K.
- (2) Mount the D-dot flush [or recessed by the same distance as in step (1)] with the cylindrical waveguide wall. Measure the power received by the

probe as well as the frequency in the TM_{01} wave, and use Eq. (8) to compute the power in the TM_{01} mode.

This D-dot probe analysis assumes that there is no reflected power or higher-order modes present. Also, care must be exercised to ensure that the probe has sufficient attenuation to prevent arcing at its output connector. It is very important not to place the probe in the region of the beam dump, since if the electron beam itself does not damage or short out the probe, then the plasma formed in the dump region can distort the signal or even short out the probe.

The experimental setup to be used for the D-dot measurements on Sinus-6 is shown in Fig. 4. Notice that two back-to-back WR90 waveguide-to-coax adapters are placed before the crystal detector to serve as a highpass filter in order to filter out the low-frequency noise pickup to which the D-dot probe is susceptible. Ideally you would like to use an X-band bandpass filter to accomplish this and to suppress any high-frequency components which could contaminate your results, but none is available.

References

- [1] S. Burkhart, "Coaxial E-field probe for high-power microwave measurement," IEEE Trans. Microwave Theory Tech. MTT-33, 262 (1985).
- [2] R. E. Collin, Foundations for Microwave Engineering (McGraw-Hill, New York, 1966), Chap. 3.
- [3] R. A. Waldron, Theory of Guided Electromagnetic Waves (Van Nostrand Reinhold Co., London, 1969), Chap. 4.
- [4] A. L. Peratt *et al.*, "A high-power reflex triode microwave source," IEEE Trans. Plasma Sci. PS-13, 498 (1985).
- [5] Large diameter air coax line (called the "Tin Man") was designed by Don Voss for the Phillips Lab and has been used to calibrate both D-dots and B-dots.
- [6] L. D. Moreland *et al.*, "Efficiency enhancement of high power vacuum BWOs using nonuniform slow wave structures," submitted to IEEE Trans. Plasma Sci.
- [7] L. M. Earley *et al.*, "Comprehensive approach for diagnosing single-pulse microwave sources," Rev. Sci. Instrum. 57, 2283 (1986).

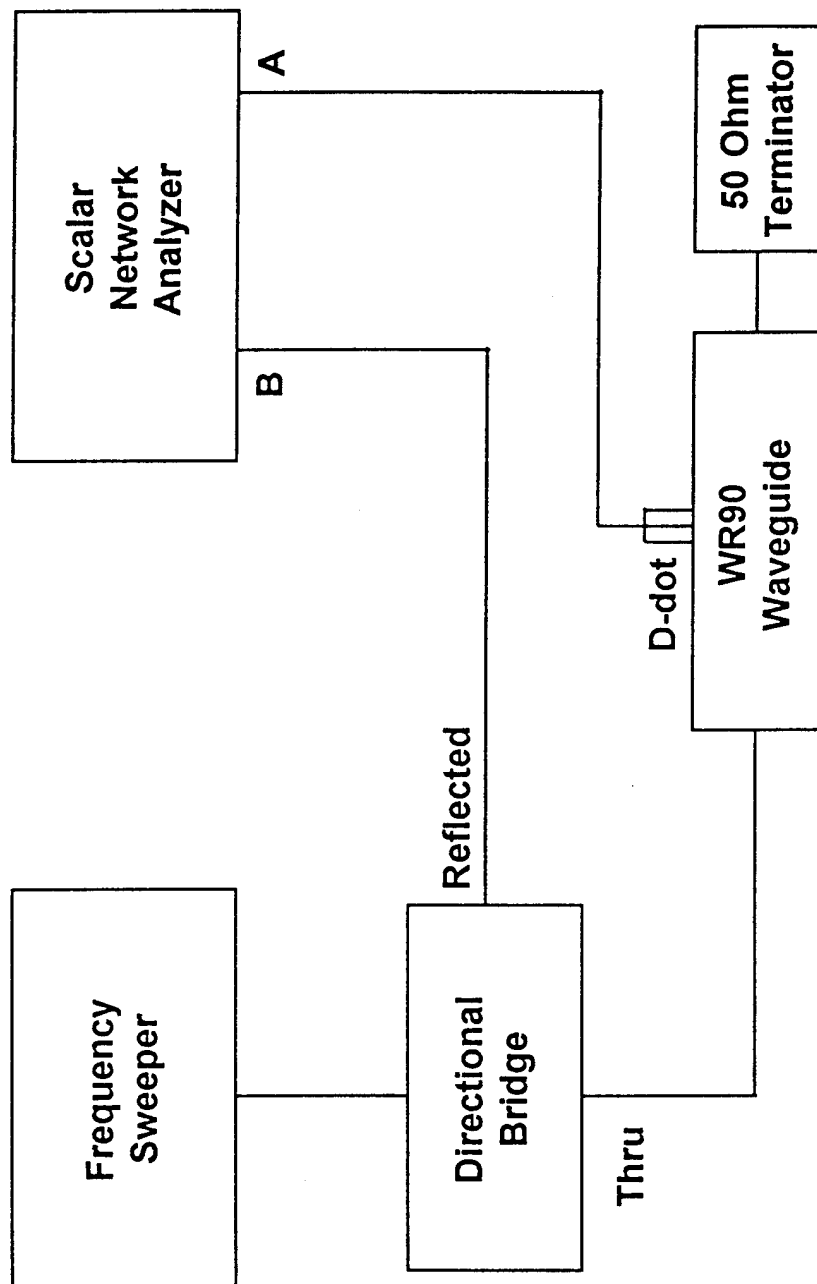


Fig.. 1. Calibration setup used to determine effective area, K, of D-dot probe.

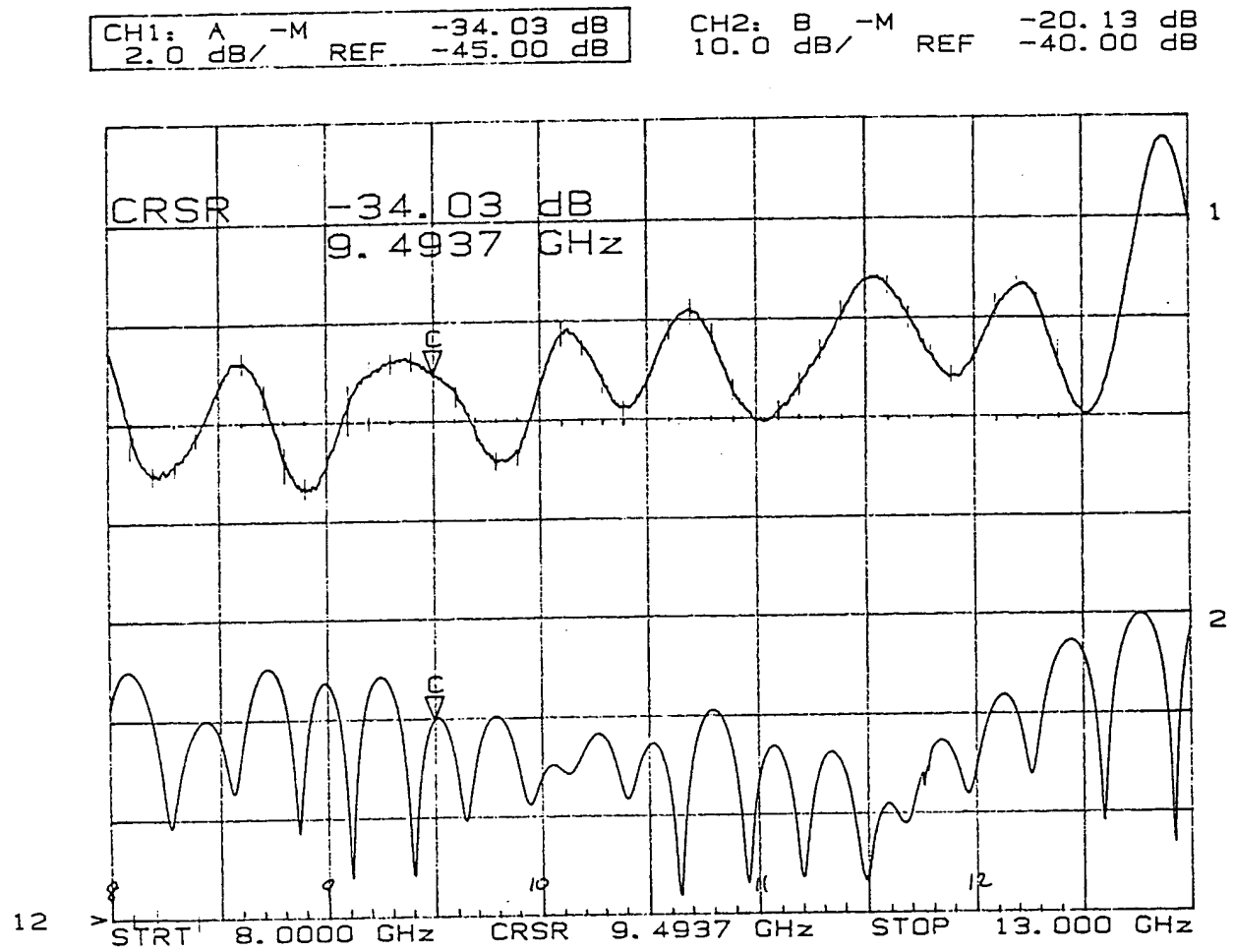


Fig. 2. Typical D-dot calibration data using the setup in Fig. 1.

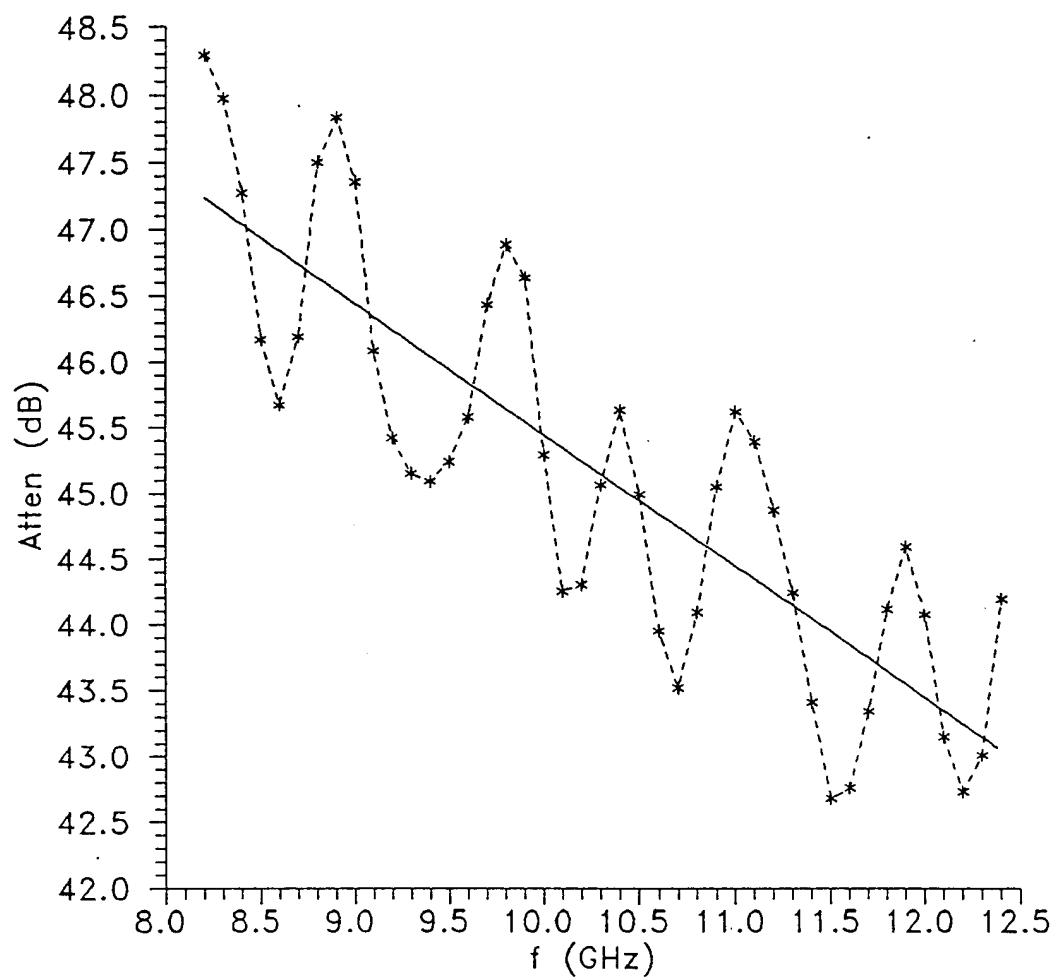


Fig. 3. Flush-mounted Sinus-6 D-dot probe attenuation factor for TM_{01} waves. Solid line is linear least-squares fit to data.

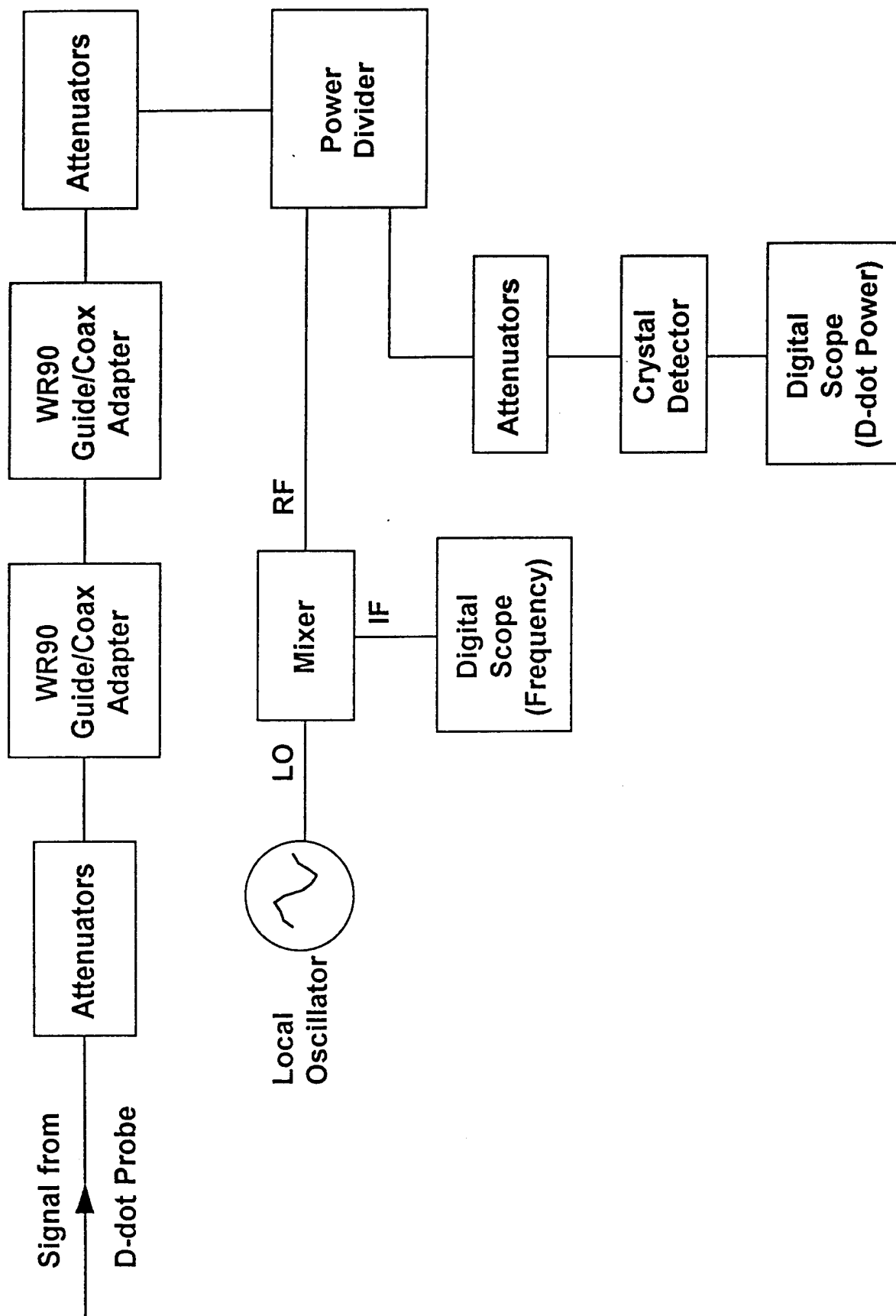


Fig. 4. Screen room setup for D-dot probe measurements.

The University of New Mexico

EECE Department
Room 110, EECE Building
Albuquerque, NM 87131

Memorandum

To: UNM HPM Group
From: Mike Haworth *MA*
Date: 8/1/94
Subject: Cold measurements on BWO slow-wave structures. Part I.: TM_{01} dispersion relation results.

This note discusses the results of cold measurements made on two BWO slow-wave structures: an 8-period uniform structure using type-D rings and an 11-period nonuniform structure using the A-A-B-B-B-C-C-C-D-D-C ring configuration. In both cases resonant frequency measurements and SUPERFISH runs were made to yield dispersion relations for the structures.

I. Introduction

A common method of measuring the propagation characteristics of a slow-wave structure is to place shorting planes at axial points of mirror translational symmetry [1]. This forms a resonant cavity consisting of N periods of the slow-wave circuit. The cavity is weakly excited at one end, and the resonances are measured either with a pick-up antenna at the other end (transmission method) or from the dips in the reflection coefficient measured from the launching antenna circuit (reflection method).

The cavity resonates at integral numbers of half-wavelengths, so for a slow-wave structure of period L and total length NL , the resonance condition is [1]

$$NL = \frac{n\lambda_g}{2}, \quad n = 0, 1, \dots, N \quad (1)$$

where λ_g is the guide wavelength. Rewriting Eq. (1) in terms of the cavity wave number (or wave propagation constant) $\beta = 2\pi/\lambda_g$, then

$$\beta L = \frac{n}{N} \pi, \quad n = 0, 1, \dots, N. \quad (2)$$

Eq. (2) shows that there are $N+1$ phase shifts per period from 0 to π for each passband (the TM_{01} passband, for example). A plot of ω_n vs. $(\beta L)_n$ at the $N+1$ resonant frequencies yields the desired dispersion relation (also called a Brillouin or ω - β diagram). This

technique applies for experimental measurements as well as for a numerical solution of the dispersion relation via the resonant cavity code SUPERFISH [2,3].

II. SUPERFISH Results

The 8-period, type-D ring, uniform slow-wave structure was approximated as having an ideal sinusoidal outer wall and with both ends shorted as discussed above. The cylindrical symmetry of the problem means that only the upper half of the structure is solved (see Fig. 1). SUPERFISH was then run until the desired TM_{01} -mode resonance was found. This was repeated until all 9 resonances from the 0-mode to the π -mode were found for the TM_{01} passband.

SUPERFISH E-field plots for this structure are shown in Fig. 2 for all 9 resonances in the range $0 \leq \beta L \leq \pi$. The resulting dispersion relation for the TM_{01} passband is shown as the solid line in Fig. 3. (Note that this line was obtained by cubic spline fitting the 9 discrete $(\beta L, \omega)$ data points from the SUPERFISH results in Fig. 2.)

III. Experimental Results

The experimental values for the slow-wave structure resonances were found using the reflection method discussed above, with the experimental setup shown in Fig. 4. Eight type-D rings were inserted into the Sinus-6 BWO tube and both ends were shorted using solid stainless steel rings. A piece of 0.141 semi-rigid cable penetrated the upstream shorting ring on axis, and RF from the sweeper was fed into it to launch a particular mode.

Two different launching antennas were tried: a simple on-axis monopole antenna using the center conductor of the 0.141 cable and a rod-wheel-type antenna [3] developed at the University of Maryland. The latter antenna, which worked slightly better, is shown in Fig. 5 and was approximately 0.5-in. in O.D., consisted of 6 spokes each intercepting 20° , and was fabricated using single-sided printed circuit board. The rod wheel was soldered onto the center conductor of the 0.141 cable and was inserted around 0.5 cm into the cavity.

Typical reflection data for the 8-period, type-D ring, uniform slow-wave structure is shown in Fig. 6. A comparison between the experimental and SUPERFISH results are shown in Fig. 3. A similar procedure was carried out for the long, nonuniform A-A-B-B-B-C-C-C-D-D-C structure and the dispersion results are shown in Figs. 7 to 9. Notice that the SUPERFISH results for both the 0- and π -modes appear to be in error since they indicate a non-zero group velocity for these modes. The E-field structure for these two modes shown in the first and last plots in Fig. 7 indicates trouble, but the reason for this error is not known.

Looking at the data in Fig. 6, it's very clear how you obtain the resonant frequency data, but how do you determine the values for βL ? The answer is that Eq. (2) tells you that there should be 9 resonances in this case, and you simply assume that the first resonance is the 0-mode and the last one is the π -mode. This is obviously not a very satisfying procedure and can lead to incorrect results since spurious resonances are often present. This is particularly apparent in Fig. 9, where the mode assignments for the experimental data were basically guided by the SUPERFISH results.

Fortunately, there is a measurement technique commonly used in the RF accelerator community that allows you to unambiguously identify the correct βL -value corresponding to a resonant frequency. It is called the beadpull technique [4,5] and is based on the Slater cavity perturbation formula [1,4]. The operating principle is that a small perturbation (i.e., a spherical bead) is introduced into the cavity, which produces a slight shift in the resonant frequency. The frequency difference with and without the bead is proportional to the square of the E-field (and/or the H-field).

Thus, by measuring the change in the cavity resonant frequency as the bead travels axially down the slow-wave structure, it is possible to map out the E_z -field of the mode. As Fig. 10 illustrates for three modes in the TM_{01} passband for the 8-period, type-D ring, uniform slow-wave structure, the number of phase shifts per period [i.e., the value of n in Eq. (2)] is determined by simply counting the number of zero crossings in the E_z -field pattern.

A beautiful example of the beadpull technique applied to slow-wave structure measurements is presented in Ref. 5. An added bonus of the beadpull technique is that if its results taken at the beam radius are combined with the dispersion relation results, then the interaction impedance can be calculated [1].

References

- [1] C. C. Johnson, Field and Wave Electrodynamics (McGraw-Hill, New York, 1965), Chaps. 6 and 7.
- [2] K. Halbach and R. F. Holsinger, "SUPERFISH - A computer program for evaluation of RF cavities with cylindrical symmetry," Part. Accel. 7, 213 (1976).
- [3] H. Guo *et al.*, "A novel highly accurate synthetic technique for determination of the dispersive characteristics in periodic slow wave circuits," IEEE Trans. Microwave Theory Tech. 40, 2086 (1992).
- [4] L. C. Maier and J. C. Slater, "Field strength measurements in resonant cavities," J. Appl. Phys. 23, 68 (1952).
- [5] Bill Main (private communication). W. Main *et al.*, "Electromagnetic properties of open and closed overmoded slow-wave resonators for interaction with relativistic electron beams," (to be published).

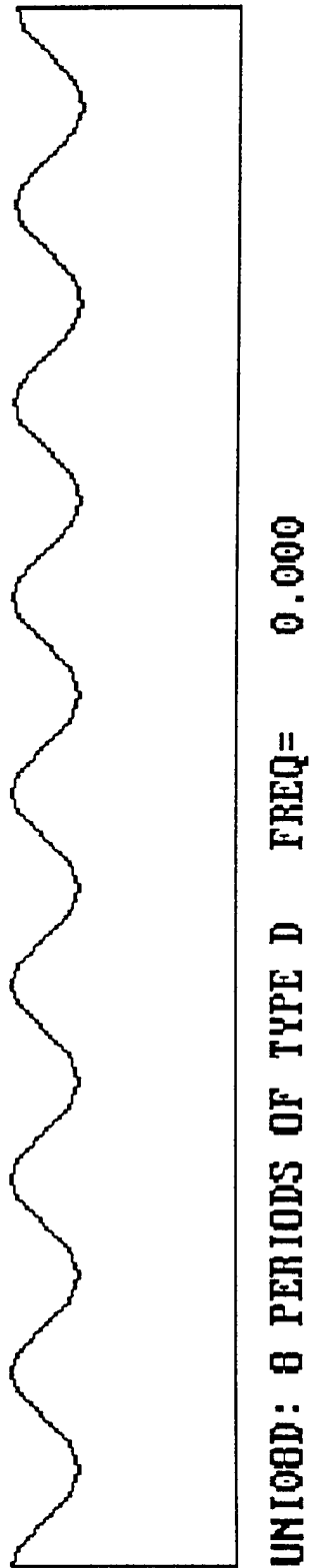


Fig. 1. SUPERFISH problem geometry for the 8-period, type-D ring, uniform BWO slow-wave structure.



UN108D: 8 PERIODS OF TYPE D FREQ= 8114.217

(a) 0-mode



UN108D: 8 PERIODS OF TYPE D FREQ= 8189.574

(b) $\pi/8$ -mode



UN108D: 8 PERIODS OF TYPE D FREQ= 8409.400

(c) $2\pi/8 = \pi/4$ -mode



UN108D: 8 PERIODS OF TYPE D FREQ= 8755.956

(d) $3\pi/8$ -mode



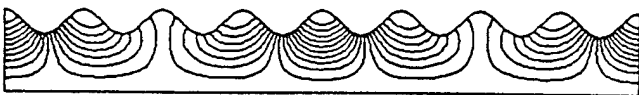
UN108D: 8 PERIODS OF TYPE D FREQ= 9201.210

(e) $4\pi/8 = \pi/2$ -mode



UN108D: 8 PERIODS OF TYPE D FREQ= 9705.774

(f) $5\pi/8$ -mode



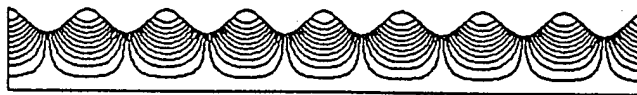
UN108D: 8 PERIODS OF TYPE D FREQ=10210.065

(g) $6\pi/8 = 3\pi/4$ -mode



UN108D: 8 PERIODS OF TYPE D FREQ=10618.663

(h) $7\pi/8$ -mode



UN108D: 8 PERIODS OF TYPE D FREQ=10784.045

(i) $8\pi/8 = \pi$ -mode

Fig. 2. SUPERFISH results for the 0- to π -modes in the TM_{01} passband of the 8-period, type-D ring, uniform BWO slow-wave structure.

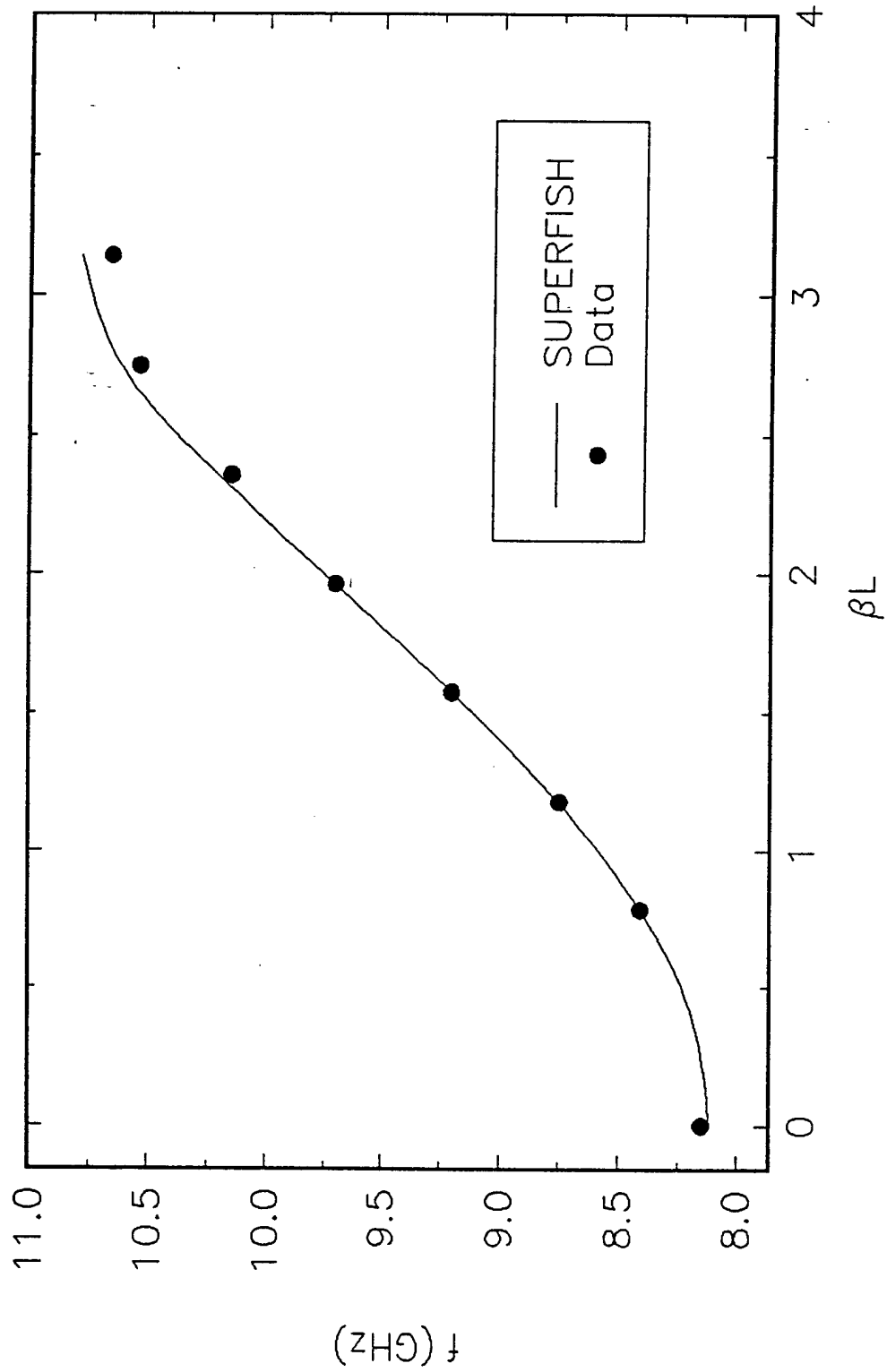


Fig. 3. Dispersion relation for the TM_{01} passband of the 8-period, type-D ring, uniform BWO slow-wave structure. Circles are the experimental data from cold testing, while the solid line is a cubic spline fit of the SUPERFISH results from Fig. 2.

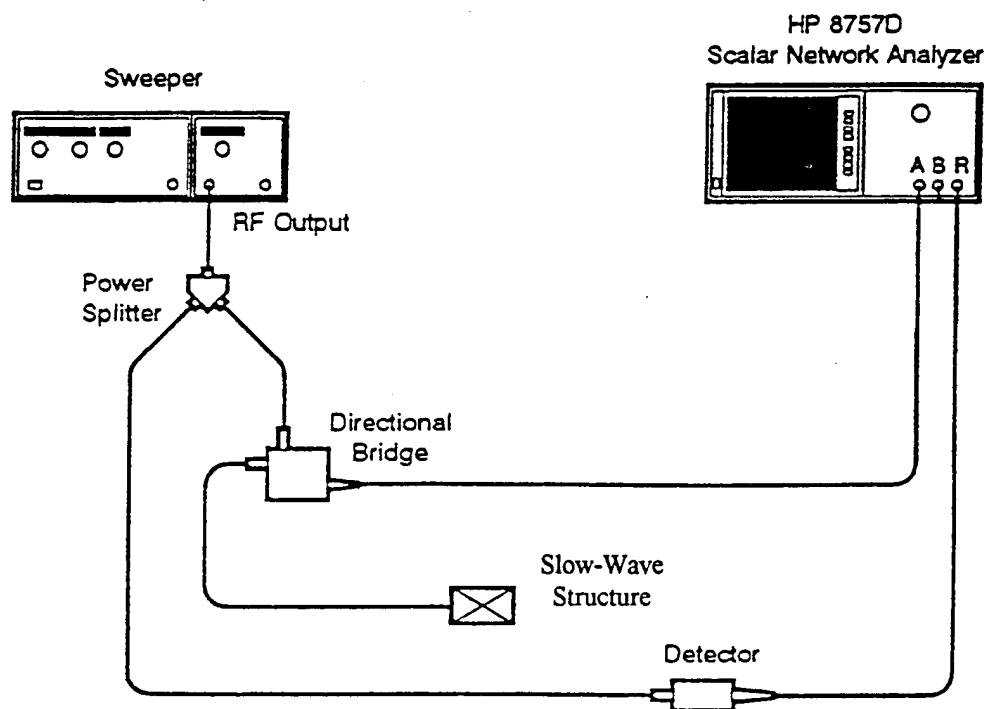


Fig. 4. Experimental setup for the cold tests.

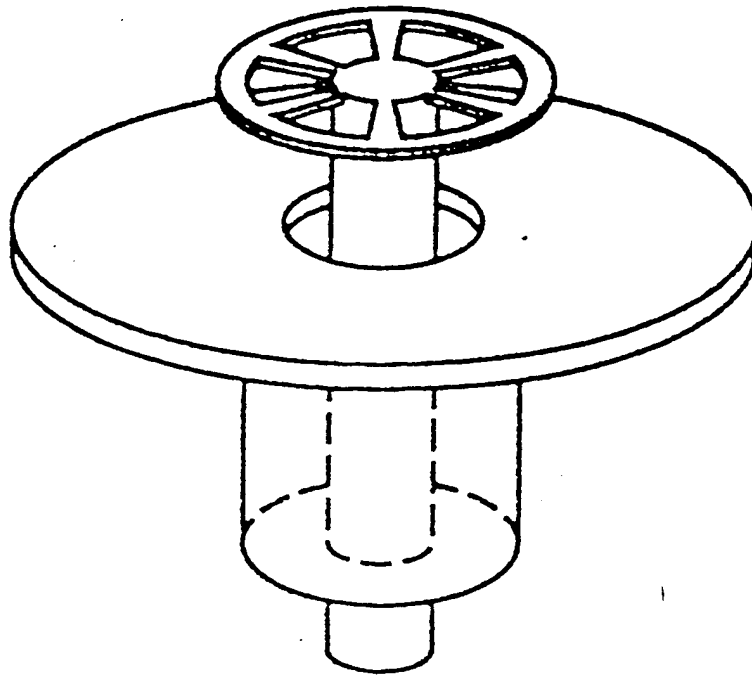


Fig. 5. Sketch of the rod wheel radiator used to launch the modes in the TM_{01} passband.
(This figure was taken from Ref. 3.)

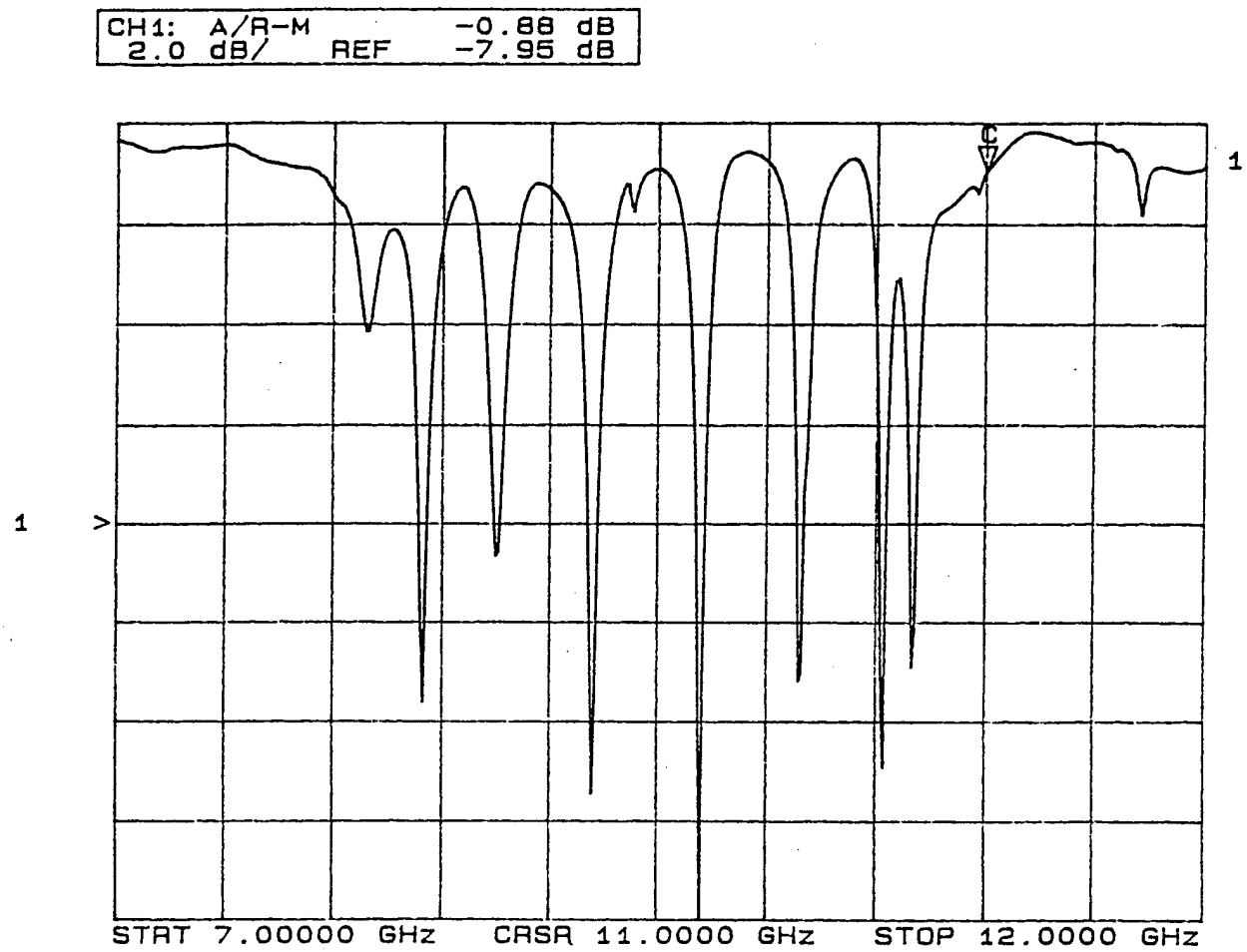


Fig. 6. Reflected power from the feed to the rod wheel antenna for the 8-period, type-D ring, uniform BWO slow-wave structure shorted at both ends.



(a) 0-mode



(b) $\pi/11$ -mode



(c) $2\pi/11$ -mode



(d) $3\pi/11$ -mode



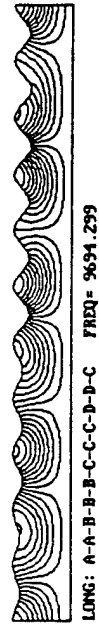
(e) $4\pi/11$ -mode



(f) $5\pi/11$ -mode



(g) $6\pi/11$ -mode



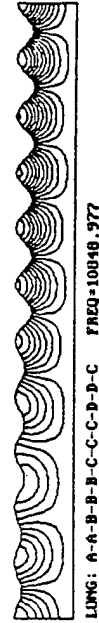
(h) $7\pi/11$ -mode



(i) $8\pi/11$ -mode



(j) $9\pi/11$ -mode



(k) $10\pi/11$ -mode



(l) $11\pi/11 = \pi$ -mode

Fig. 7. SUPERFISH results for the 0- to π -modes in the TM_{01} passband of the 11-period, nonuniform BWO slow-wave structure (A-A-B-B-B-C-C-D-D-C ring configuration).

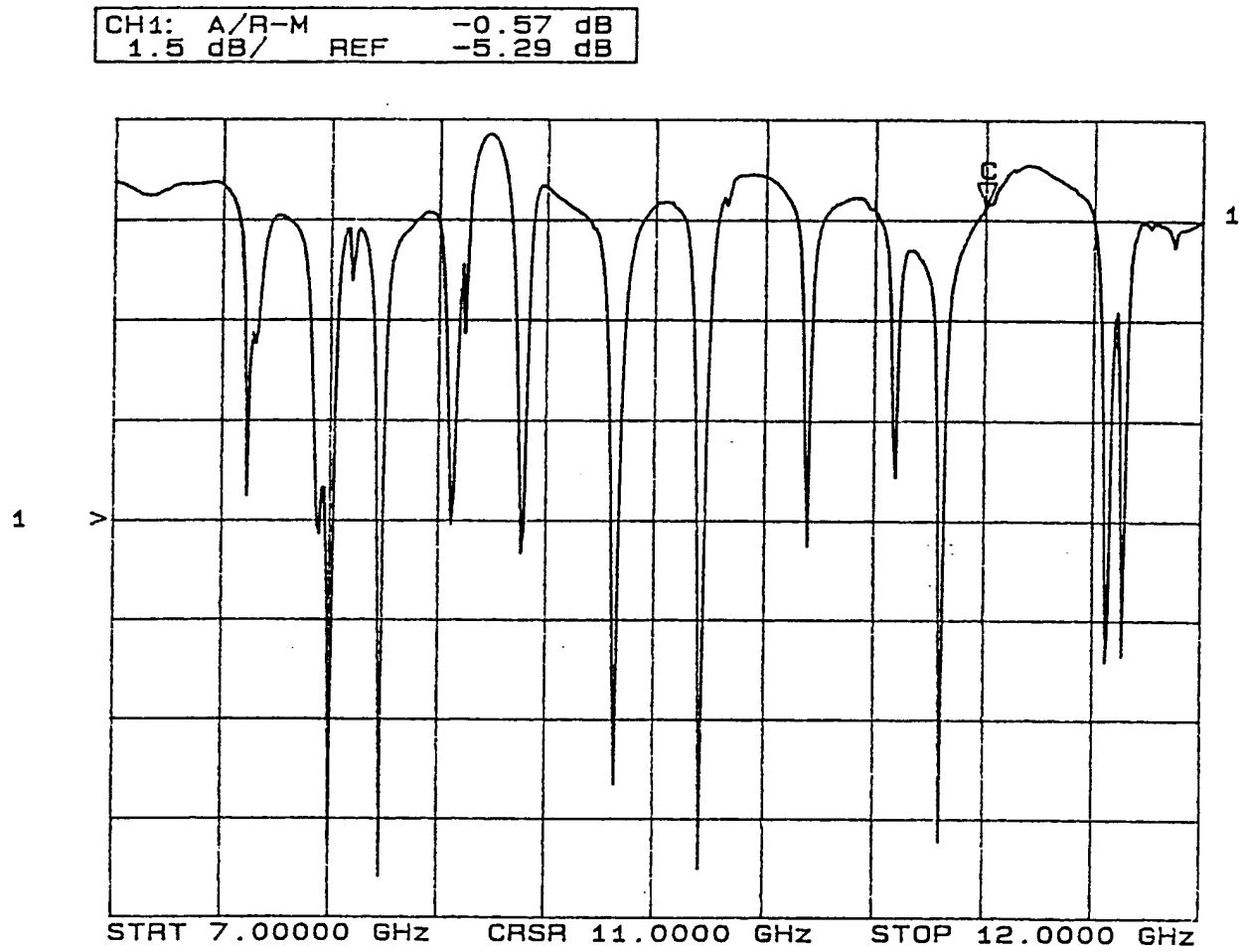


Fig. 8. Reflected power from the feed to the rod wheel antenna for the 11-period, nonuniform BWO slow-wave structure (A-A-B-B-B-C-C-C-D-D-C ring configuration) shorted at both ends.

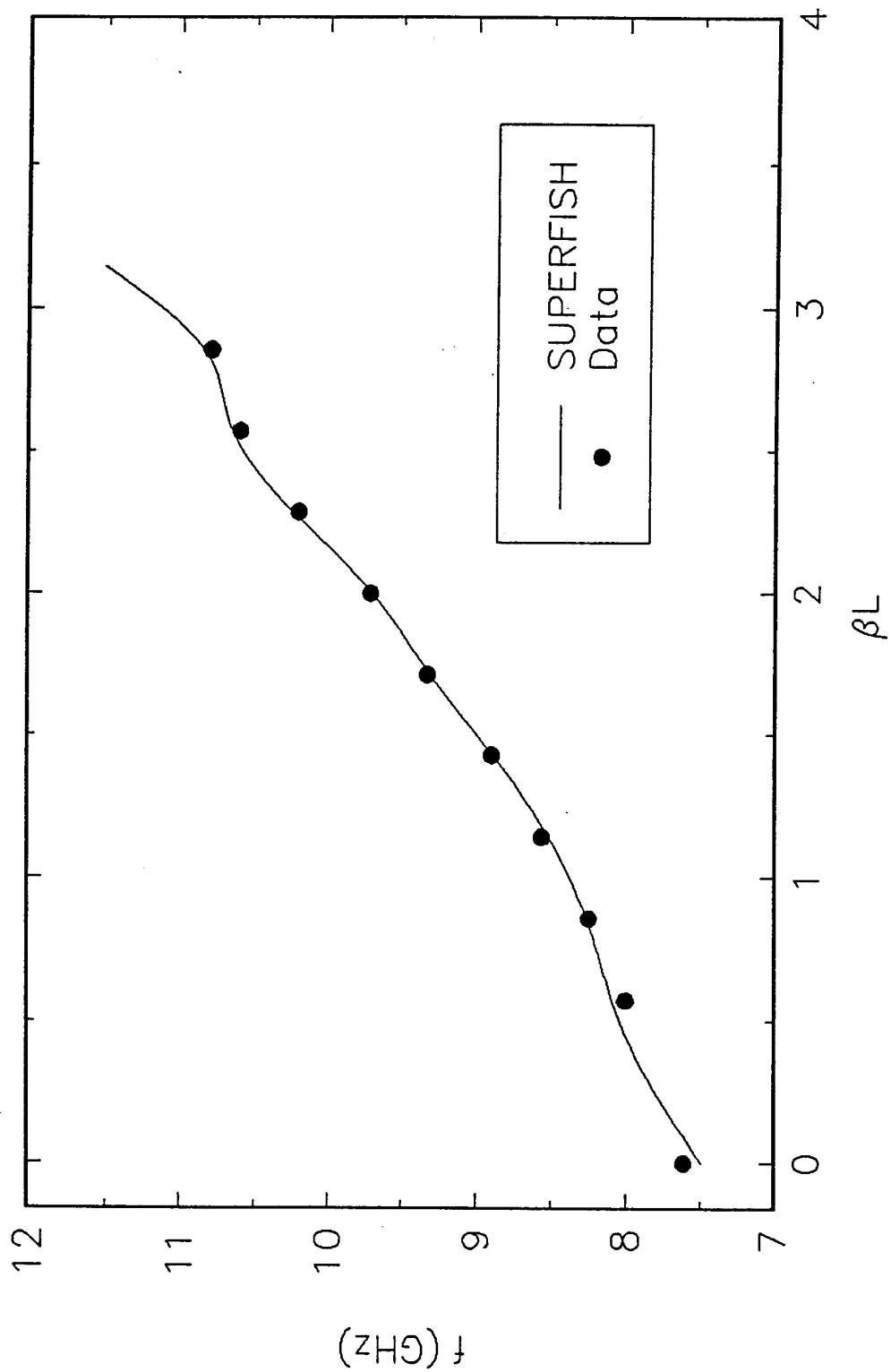


Fig. 9. Dispersion relation for the TM_{01} passband of the 11-period, nonuniform BWO slow-wave structure (A-A-B-B-C-C-D-D-C ring configuration). Circles are the experimental data from cold testing, while the solid line is a cubic spline fit of the SUPERFISH results from Fig. 7.

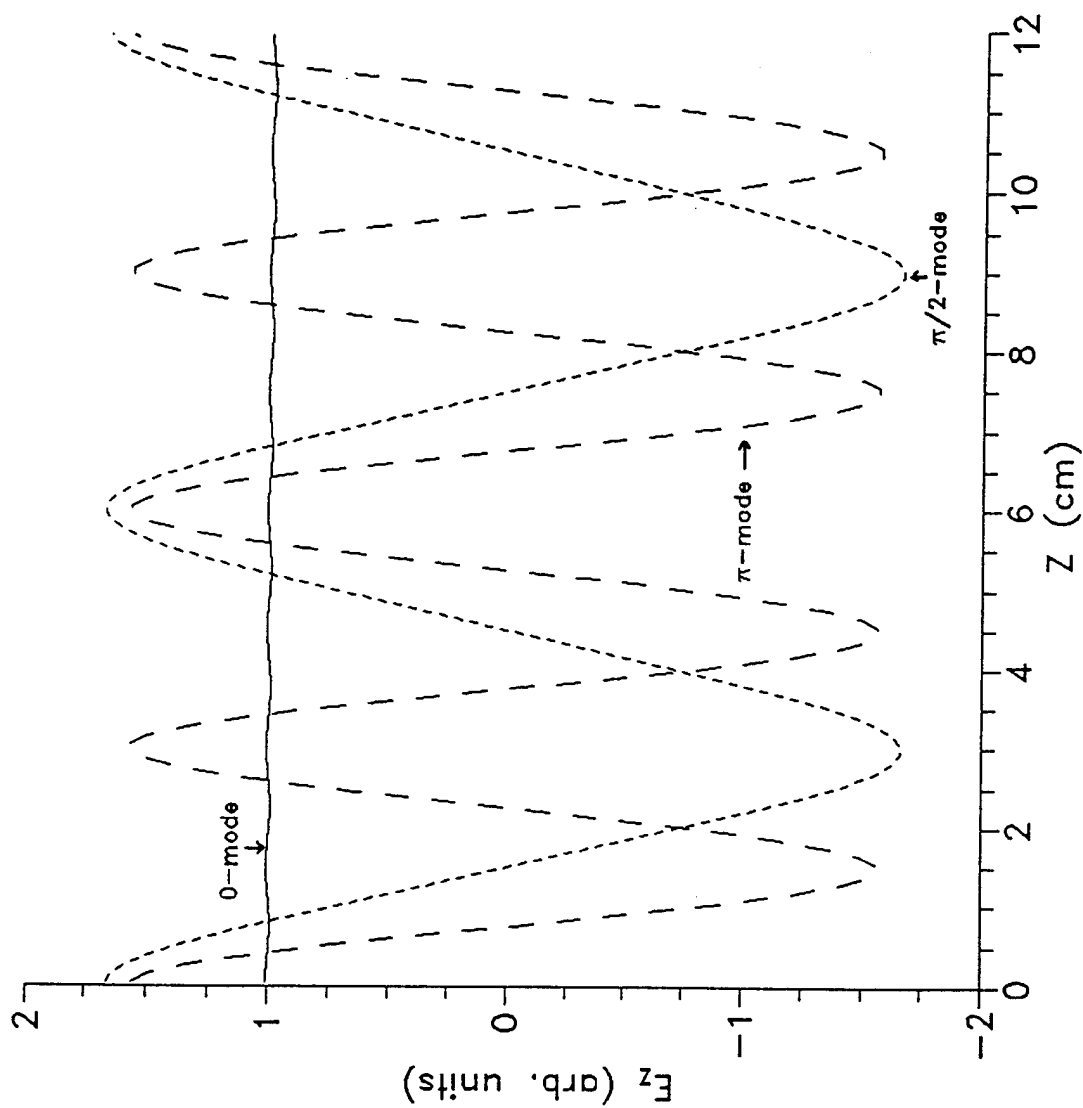


Fig. 10. SUPERFISH results for on-axis E_z -field profiles for the 0-, $\pi/2$ -, and π -modes of the TM_{01} passband of the 8-period, type-D ring, uniform BWO slow-wave structure.

VI. Bibliography of Presentations and Papers

Journal Articles

1. L. D. Moreland, E. Schamiloglu, R. W. Lemke, S. D. Korovin, V. V. Rostov, A. M. Roitman, K. J. Hendricks, and T. A. Spencer, *IEEE Trans. Plasma Sci.* **22**, 554 (1994).
2. C. S. Mayberry, B. Wroblewski, E. Schamiloglu, and C. B. Fleddermann, *J. Appl. Phys.* **76**, 4448 (1994).
3. T. C. Cavazos, W. L. Wilbanks, C. B. Fleddermann, and D. A. Shiffler, *Appl. Phys. Lett.* **65**, 2612 (1994).

Conference Papers

1. E. Schamiloglu, J. Gahl, C. Fleddermann, D. Shiffler, L. Moreland, C. Grabowski, T. Cavazos, B. Wroblewski, and W. Wilbanks, to appear in *Proceedings NATO AGARD Electromagnetic Wave Propagation Panel Symposium on High Power Microwaves*.
2. L. D. Moreland, E. Schamiloglu, R. Lemke, J. Gahl, and D. Shiffler, "Effects of Using a Nonuniform-Amplitude Slow Wave Structure in a Repetitively-Pulsed, High Power Relativistic Backward Wave Oscillator," *Proc. of the 9th IEEE International Pulsed Power Conf.* (1994), p. 396.
3. C. Grabowski, J. Gahl, E. Schamiloglu, and D. Shiffler, "Long-Pulse High Power Microwave Experiments," *Proc. of the 9th IEEE International Pulsed Power Conf.* (1994), p. 600.
4. T. Cavazos, D. Shiffler, B. Wroblewski, C. Fleddermann, J. Gahl, and E. Schamiloglu, "Initial Studies of Ferroelectric Cathodes," *Proc. of the 9th IEEE International Pulsed Power Conf.* (1994), p. 950.
5. E. Schamiloglu, L. D. Moreland, R. W. Lemke, J. M. Gahl, and C. Grabowski, "Efficiency Enhancement of High Power Vacuum Backward-Wave Oscillators Driven by Short Pulse and Long Pulse Electron Beams," *Proceedings of the EUROEM 94 International Symposium* (EUROEM, 46500 Gramat, France).
6. T. Cavazos, W. Wilbanks, C. Fleddermann, and D. Shiffler, "Investigation of

Electron Emission from Bulk (Pb,La)(Zr,Ti)O₃ Ferroelectric Ceramics," to appear in *Proceedings 1994 IEEE Electron Devices Conference*.

Conference Presentations

1. C. Grabowski, J. Gahl, E. Schamiloglu, and D. Shiffler, "Progress in the Long-Pulse BWO Experiment at the University of New Mexico," IEEE International Conference on Plasma Science (Santa Fe, NM, 1994).
2. L. D. Moreland, A. M. Roitman, E. Schamiloglu, R. W. Lemke, and I. V. Pegel, "Power and Frequency Measurements from a Uniform Backward Wave Oscillator as a Function of Length," IEEE International Conference on Plasma Science (Santa Fe, NM, 1994).
3. A. M. Roitman, L. D. Moreland, E. Schamiloglu, R. W. Lemke, and I. V. Pegel, "A High Efficiency Relativistic Uniform Backward Wave Oscillator," IEEE International Conference on Plasma Science (Santa Fe, NM, 1994).
4. R. W. Lemke, L. D. Moreland, E. Schamiloglu, S. D. Korovin, I. V. Pegel, and A. M. Roitman, IEEE International Conference on Plasma Science (Santa Fe, NM, 1994).
5. I. V. Pegel, L. D. Moreland, E. Schamiloglu, A. M. Roitman, V. P. Gubanov, A. V. Gunin, S. D. Korovin, V. V. Rostov, and V. P. Tarakanov, "Numerical Simulation and Experimental Measurement of Pulse Generation in Coaxial Forming Lines," IEEE International Conference on Plasma Science (Santa Fe, NM, 1994).
6. T. Cavazos, W. Wilbanks, C. Fleddermann, and D. Shiffler, "Investigation of Electron Emission from Thin Film and Bulk PLZT Ferroelectric Ceramics," IEEE International Conference on Plasma Science (Santa Fe, NM, 1994).
7. C. Fleddermann, T. Cavazos, W. Wilbanks, and D. Shiffler, "Ferroelectric Cathodes for Pulsed Gas Discharge Triggering," 47th Annual Gaseous Electronics Conference (Gaithersburg, MD, 1994).

Patents

1. Patent application filed "DC Reset for Ferroelectric Cathodes" (Ref. UNM-382).

VII. References

1. L. D. Moreland, *Effects of Varying Coupling Impedance, Finite Length, and Asynchronous Harmonics on High Power BWO Performance*, Ph.D. dissertation, University of New Mexico (1995). This is available on the WWW. Access URL <http://www.eece.unm.edu> and click on the faculty under Prof. Schamiloglu.
2. L. D. Moreland, E. Schamiloglu, R. W. Lemke, S. D. Korovin, V. V. Rostov, A. M. Roitman, K. J. Hendricks, and T. A. Spencer, *IEEE Trans. Plasma Sci.* **22**, 554 (1994).

Appendix A: Status of Personnel

- Professors Schamiloglu and Gahl were promoted to Associate Professors of Electrical & Computer Engineering with tenure.
- Professor Shiffler resigned from his tenure-track Assistant Professor position. He is now a Research Assistant Professor assigned to the Air Force Phillips Laboratory. He is no longer associated with this project.
- Dr. Mike Haworth, a Research Associate Professor, has been assigned to the Air Force Phillips Laboratory.
- Larald Moreland has completed his Ph.D. dissertation and is presently a postdoc at the University of New Mexico.
- Chris Grabowski is making progress towards completion of his Ph.D.
- Tommy Cavazos is now being supervised and is making progress towards completion of his Ph.D.
- W. L. Wilbanks has left the M.S. program for permanent employment.

Appendix B: Overview Paper Presented at AGARD Panel

High Efficiency Backward-Wave Oscillators for High Power Microwave Generation: Present Status and Future Trends

E. Schamiloglu, J. Gahl, C. Fleddermann, D. Shiffler, L. Moreland,
C. Grabowski, T. Cavazos, B. Wroblewski, and W. Wilbanks

Department of Electrical and Computer Engineering
University of New Mexico
Albuquerque, NM, 87131, USA

Summary

The efficiency of high peak power microwave generation in vacuum X-band backward-wave oscillators is described. Nonuniform slow wave structures are driven by the Sinus-6, a short pulse, repetitive relativistic electron beam accelerator. Peak microwave power exceeding 500 MW at 9.45 GHz has been measured in an 8 ns pulse. The corresponding beam-to-microwave power conversion efficiency was 17%, although efficiencies approaching 25% have been achieved at lower power levels. The ability to acquire a large amount of data using the Sinus-6 accelerator facilitates comparisons with electromagnetic particle-in-cell simulations and analytical theories. In a companion set of experiments, a modified PI-110A single shot electron beam accelerator is used to study backward-wave oscillators with parameters comparable to the Sinus-6 experiments, except at pulse durations approaching 0.5 μ s. The goal of these studies is to extend the duration of microwave generation in high power backward-wave oscillators to several hundreds of nanoseconds. Technological innovations, such as ferroelectric cathodes and thin film metallic coatings, are expected to yield significant advances in long pulse operation.

1. Introduction

High power backward-wave oscillators (BWOs) have been studied experimentally and theoretically for about 25 years (Ref 1). The resurgence in interest in these classical microwave tubes coincided with the development of pulsed high current relativistic electron beam accelerators. Researchers in the United States primarily use single shot electron beam accelerators whose energy store is a Marx bank (Ref 1). The electron beams propagate through slow wave structures with uniform ripple amplitudes and periods, transported by a strong axial magnetic field. Researchers in the Former Soviet Union, on the other hand, developed several generations of repetitively-pulsed electron beam accelerators based on Tesla transformer technology with very high coupling efficiencies (Ref 1). In addition, they developed complicated slow wave structures which were motivated by theoretical analyses showing that nonuniform BWOs can be designed to yield higher beam-to-microwave power conversion efficiencies than uniform BWOs (see Refs 2 and 3, and references therein). In a nonuniform BWO, variations in the coupling impedance or

phase velocity affect the interaction between the electron beam and electromagnetic modes along the length of the tube. The coupling impedance between the slow space charge wave on the electron beam and the surface harmonic of the backward TM_{01} mode can be modified by varying the ripple amplitude, or by varying the magnetic field distribution within the tube. The phase velocity of this harmonic can be varied along the length of the tube by gradually changing the period of the ripples. The efficiencies for converting input beam power into RF radiation using uniform BWOs have been reported to be as large as 15% (Ref 2). Work in the former Soviet Union on nonuniform BWOs has shown experimental measurements of RF efficiencies exceeding 40%, and theoretical predictions indicate efficiencies may reach 75% in the absence of space charge effects (Refs 2 and 3).

The high power BWO program at the University of New Mexico seeks to define the physics of efficient microwave generation in uniform and nonuniform BWOs in both the short pulse and long pulse regimes. Basic understanding is gained from experiments using the Sinus-6, a repetitively-pulsed relativistic electron beam accelerator developed jointly by the High Current Electronics Institute (Tomsk, Russia) and the Institute of Electrophysics (Ekaterinburg, Russia). This basic understanding is then transferred to the PI-110A long pulse experiments. It is expected that technological innovation will lead to advances in long pulse BWO operation beyond the 100 ns barrier that researchers have typically faced (Ref 1).

2. Sinus 6 Experiments

The experiments using the Sinus-6 described below seek to quantify the use of a shallow ripple-amplitude initial section of a nonuniform BWO as a prebuncher to increase the microwave generation efficiency.

Figure 1 is a cut-away diagram of the Sinus-6. The Tesla transformer (1) steps up the voltage from 300 V to 700 kV. An open ferromagnetic core is used in the Tesla transformer, which provides a high coupling coefficient between the transformer windings. The pulse forming line is contained within the Tesla transformer, permitting both increased efficiency and an overall compact system. The high voltage switch (2) is a nitrogen-filled spark gap, which is pressurized to 16 atmospheres. By adjusting the pressure the spark gap voltage can be varied from 350 to 700 kV. The oil-filled

2
adiabatic transmission line (3) matches the 22 Ω impedance of the pulse forming line to the $\approx 100\Omega$ impedance of the vacuum diode. The magnetically insulated coaxial diode uses an explosive-emission graphite cathode (2 cm diameter with a 1 mm annular wall thickness). A uniform magnetic field up to 3.0 T in magnitude, used to confine the electron beam, is generated by a pulsed solenoid system (4). The pulsed system provides a magnetic field pulse duration of 3 ms and requires 10 s to recharge. The Sinus-6 can generate electron beams at a pulse repetition rate of 200 Hz, but is presently operating at 0.1 Hz due to constraints imposed by the magnetic field system.

The Anode-Cathode ($A - K$) gap spacing and applied magnetic field were held constant and the resultant diode impedance was about 125 Ω , depending on the cathode potential. The electron beam pulse has a full width, half maximum (FWHM) temporal duration of about 12 ns. Cathode voltages are measured using a capacitive divider, and beam currents are measured using a Rogowski coil. By adjusting the pressure in the spark gap, cathode voltages from 400 to 650 kV are generated with corresponding beam currents ranging from 3 to 5 kA.

Total peak radiated power measurements were made using both a semiconductor microwave detector and a crystal diode detector (set-up shown schematically in Fig 2). Power density measurements were made 1.6 m downstream from a conical horn antenna which has a maximum diameter of 15 cm. The total power was calculated by numerically integrating the radiation pattern that was experimentally mapped. The radiated frequency was measured by heterodyning the RF signal against a known oscillator frequency.

The basic tube studied in this work is a nonuniform amplitude configuration referred to as the "Long Tube". This tube is a two stage slow wave structure constructed from individual rings for each ripple period, and was designed based on the work of Kovalev and colleagues (Ref 2). Each ring is a trapezoidally shaped annulus with a width of 1.5 cm (corresponding to a ripple period of 1.5 cm) and a maximum radius of 1.65 cm. Four different rings were used, and their parameters are listed in Table 1.

In addition to this basic tube, variations referred to as Short Tubes #1-#3 were also studied to elucidate the role of the initial stage of the Long Tube. As is evident from Table 2, the short tubes are variations of the second stage of the Long Tube. These short tubes have a start current in the range of the start current for the Long Tube.

A typical mode pattern radiated by the Long Tube and measured 1.6 m from the output antenna is shown in Fig 3. The beam parameters

used were 500 kV and 4 kA, and each data point was the average of 3 to 5 shots. The calculated TM_{01} radiation pattern (Ref 4) for a total peak power of 500 MW is indicated by the solid line in Fig 3. For comparison, the data points were integrated numerically to yield a total power of 450 MW, in good agreement with the calculated mode pattern. Since the radiation pattern was found to be insensitive to slight changes in frequency, it was sufficient to measure the power density at the maximum electric field in order to ascertain the total radiated power.

Figure 4 shows the dependence of peak radiated power using the Long Tube on electron beam current. Each data point represents the average of 5 shots and the error bar represents the typical scatter in the data. The beam current was changed by varying the pressure in the spark gap switch and the applied voltage to the cathode. The $A - K$ gap and applied magnetic field were held constant for all shots. The results from Long Tube over a range of parameters are summarized in Table 3. In this parameter scan the measured frequency remained constant at 9.45 ± 0.05 GHz.

At beam currents above 4 kA air breakdown near the output window was observed. Time-integrated photographs showed a bright annular ring of plasma consistent with a TM_{01} radiation mode pattern. In order to suppress the air breakdown, a gas bag filled with SF_6 was placed in front of the horn antenna. The amplitude and pulse duration from the crystal diode detector were observed to increase when the gas bag was used. Figure 4 shows the effect of using a gas bag on the microwave power measurements.

To elucidate the role of the prebuncher on the efficiency of the Long Tube, experiments were performed with various short tubes (parameters summarized in Tables 1 and 2). Sections of cutoff pipe were added to the modified tubes to ensure that the $A - K$ gap and the tapered magnetic field at the end of the tube remained constant. The beam parameters were approximately 4 kA and 500 kV, which were chosen to avoid air breakdown associated with the Long Tube. Data showing the peak output microwave power generated by the Long Tube and the three short tubes are given in Table 2. It is clear that none of the short tubes are as efficient as the Long Tube, and Short Tube #2 is the most efficient, with an efficiency of about 15%. Consistent with the lower relative powers indicated, air breakdown was never observed with the short tubes, even when they were driven at the highest input beam powers. Because the growth rate of the RF fields must decrease with the difference between the beam current and the start current, it can be inferred from the RF pulse widths in Table 2, that the start currents for the Long Tube is between the start currents for Short Tubes #2

and #3. Therefore, the increased efficiency of the Long Tube is a result of the prebuncher and cannot be attributed to the ratio of beam current to start current.

TWOQUICK (Ref 5) particle-in-cell (PIC) simulations provided a comprehensive picture of the prebunching of the electron beam in the initial section of the nonuniform amplitude slow wave structure. The results from the PIC simulations indicate that, in addition to the surface harmonic of the backward wave, the forward traveling volume harmonics may play an important role in the energy exchange process in the BWO. Based on these results it may be possible to design an uniform BWO where the forward traveling volume harmonics can serve the role of a prebuncher (Ref 6).

3. PI-110A Experiments

The accelerator used in the UNM Long Pulse BWO Experiment is a modified Physics International Pulserad 110A. An 11-stage Marx bank with an energy storage capacity of 2.75 kJ is used as the main energy store and initial pulse forming device in the accelerator. The Blumlein which previously followed the Marx bank has been replaced with an LC filter network. When erected, the Marx bank and the LC network together form a 2-stage pulse forming network (PFN). An equivalent circuit for this is shown in Fig 5. The pulse duration and impedance of the accelerator in this configuration are approximately 500 ns and 40 Ω , respectively. A balanced resistive voltage divider (not shown in the figure) has been placed between the Marx bank and the LC network to monitor the Marx voltage. The electron gun immediately follows the LC filter network, and its configuration is nearly identical to the one on the Sinus-6. The cathode holder is stainless steel and is curved to follow the magnetic field lines. At the end of the holder is a 2 cm-diameter carbon knife-edge tip from which an annular electron beam is emitted. Either 6 or 7 field coils can be placed around the slow wave structure to produce a guiding field for the electron beam. The field strength on axis is typically 3.0 T. After traveling through the slow wave structure, the electron beam follows the magnetic field lines to the beam dump, which consists of a section of stainless steel screen surrounded by a larger, concentric section of copper pipe that is lined with carbon on its inner surface. The microwaves that are produced in the slow wave structure travel past the screen into another section of circular waveguide, and then to a conical horn where they are radiated into an *anechoic* measurement area.

Two Rogowski coils are used to monitor the beam current, one around the cathode holder and the other to be located just upstream of the beam dump. In addition, a capacitive voltage divider has recently been installed just behind the first Rogowski coil to enable

measurement of the cathode voltage during experiments. To measure the microwave radiation, two different kinds of detectors have been used. One is a simple \dot{B} probe which directly measures the magnetic field intensity of the microwave radiation. The other detector is similar to the one presently being used on the Sinus-6 experiments. It consists of a small piece of a semiconductor material placed inside a short section of waveguide. Before the accelerator is fired, a negative voltage pulse having an amplitude of approximately 50 V and a duration of 100-120 μ s is sent to the detector. When microwaves enter the waveguide and impinge upon the semiconductor, the impedance of the semiconductor changes, causing a ripple in the amplitude of the reflected voltage pulse. From the amplitude of the ripple the power density of the incident microwave radiation can be determined.

Long pulse vacuum BWO experiments have begun using uniform slow wave structures. Initial results from these experiments yielded microwave pulses with FWHM durations exceeding 100 ns. Typical signals from the first Rogowski coil and the microwave detector (\dot{B} probe) are shown in Fig 6. The radiated power was estimated to be about 10 MW. By positioning the \dot{B} probe at various angles with respect to the center axis of the horn, a crude map of the radiation was obtained and indicated that the radiation is emitted in the TM_{01} mode. Frequency measurements have not been performed at this time. However, several PIC code simulations of the slow wave structure were performed and the results indicated a frequency of approximately 10 GHz. It should be noted that there was evidence of breakdown inside the slow wave structures on these shots.

4. Technological Innovations

The extension of microwave radiation in long pulse, high power BWOs beyond the typical 100 ns timescale is dependent on technological innovations. Two innovations that are being studied as part of the program at the University of New Mexico are ferroelectric cathodes and thin film metallic and ceramic coatings. Ferroelectric cathodes are potentially a new source of electrons for high power, electron beam-driven microwave devices. These cathodes have the potential to extend the pulse duration of high power BWOs beyond the 100 ns regime. Typically high power BWO experiments utilize explosive emission cathodes. These cathodes form plasmas which can expand into the anode-cathode gap and hence cause a change in the diode impedance. Furthermore, plasmas and neutrals inherent to the explosive emission process can adversely affect the BWO interaction over time scales longer than 10's of nanoseconds. Ferroelectric ceramics have the potential for providing sufficient

current to operate a BWO without the above problems (Ref 7).

Ferroelectrics are materials possessing a spontaneous electric dipole moment when the temperature is below the Curie temperature and above the Curie-Weiss temperature. Since these materials have a spontaneous dipole moment, ferroelectrics may be characterized by a bulk surface charge density which depends upon the magnitude and direction of the polarization of the sample. These materials are promising as advanced cathode materials because it is possible to liberate electron charge from the sample. The emission mechanism consists of the following sequence of events. The material is placed in a state very close to a phase transition. A large electric field is then applied across the cathode. If the electric field is of the proper polarity, a phase transition occurs, causing the cathode to become paraelectric and forcing the spontaneous electric dipole moment to zero. When the phase transition occurs, a large amount of surface charge remains momentarily unscreened on the surface of the cathode. This charge may be liberated as electrons. For example, the ferroelectric lead lanthanum zirconate titanate (PLZT) has a surface charge of 55 mC/cm^2 , corresponding to about 10^{14} electrons/ cm^2 . Furthermore, since the amount of unscreened charge is initially quite large, the emission energy of electrons from the surface can lie in the kilovolt range.

The ferroelectric experiment at the University of New Mexico consists of a ferroelectric sample placed in the triode configuration shown in Fig 7. A circular grid 0.27 cm in diameter with 20% transmission forms the emitting surface on the top of the PLZT wafer. The thickness of the wafer is 0.33 mm and the grid and plate are separated by 2.7 cm. The cathode contact on the back of the wafer is grounded. The drive circuitry is also shown in Fig 7. A bias voltage, used to produce a preset dipole moment in the sample, is applied to the grid, and the pulsed coercive field is applied through a coupling capacitor. A DC voltage of up to 20 kV is applied between the plate and the cathode contact. Current viewing resistors (CVRs) provide measurements of the grid current and plate current, while a current toroid and Rogowski coil have been used to measure current in the grid-cathode gap. Voltage measurements are obtained using resistive dividers.

Preliminary results from these experiments indicate that the initial state of the ferroelectric clearly affects the electron emission process. Emission occurs only when the ferroelectric becomes saturated. Electron charge on the order of 10's of milliCoulombs have been measured at electric fields on the order of 10 kV/cm. Ferroelectric cathodes compatible with high current accelerators are expected to be developed during the course of this investigation.

Finally, in an attempt to increase the threshold electric field for vacuum breakdown in slow wave structures, a quasi-DC experiment was performed to study the effectiveness of ion sputter-deposited thin film metallic and ceramic coatings on planar electrodes. Electric fields as high as 60 kV/mm were sustained across a 1 mm gap for pulse durations approaching 10 μs . It is believed that electron emission was suppressed by the 500 nm thick coatings because whiskers were covered and localized field enhancements were minimized (Ref 8).

Future trends in efficient high power microwave generation using vacuum BWOs will incorporate new physics, such as carefully taking advantage of the backward and forward propagating volume harmonics of the TM_{01} mode, as well as technological innovation in the form of ferroelectric cathodes and novel thin film coatings.

5. References

1. Benford, J. and Swegle, J., "High-Power Microwaves", Boston, MA, Artech House, 1992, Chap 6, and references therein.
2. Kovalev, N.F. and Petrukhina, V.I., "Ultra-relativistic Carcinotron with a Jump in Beam-rf Coupling", *Electr. Techn. SVCH*, vol. 7, 1977, pp 101-105, (in Russian), and references therein.
3. Korovin, S.D., Polevin, S.D., Roitman, A.M., and Rostov, V.V. "Relativistic backward wave tube with variable phase velocity", *Sov. Tech. Phys. Lett.*, vol. 18, 1992, pp 265-266.
4. Koslover, R.A., Computer code "TM0n", SEAC, Albuquerque NM, 1988.
5. Seidel, D.B. and Pointon, T.D., Sandia National Laboratories, private communication.
6. Moreland, L.D., Schamiloglu, E., Lemke, R.W., Korovin, S.D., Rostov, V.V., Roitman, A.M., Hendricks, K.J., and Spencer, T.A., "Efficiency of High Power Vacuum BWOs using Nonuniform Slow Wave Structures", to appear in *IEEE Trans. Plasma Sci.*, Special Issue on High Power Microwaves, 1994.
7. Riege, H., "Electron Emission from Ferroelectrics—A Review", *Nucl. Instrum. Methods*, vol. A340, 1994, pp 80-89.
8. Mayberry, C.S., Wroblewski, B., Schamiloglu, E., and Fleddermann, C.B., "Suppression of Vacuum Breakdown using Thin Film Coatings", to appear in *J. Appl. Phys.*, 1994.

Illustrations

Table 1. Parameters of slow wave structure rings.

Ring Type	Maximum Radius [cm]	Minimum Radius [cm]	Average Radius [cm]	Ripple Amplitude [cm]	Ripple Period [cm]
A	1.65	1.45	1.550	0.100	1.50
B	1.65	1.38	1.515	0.135	1.50
C	1.65	1.20	1.425	0.225	1.50
D	1.65	1.15	1.400	0.250	1.50

Table 2. Summary of tube configurations.

	Tube Configuration	Relative Power	Crystal Diode Detector Pulse Width [ns]	Frequency ± 0.05 [GHz]
Long Tube	A-A-B-B-B-C-C-C-D-D-C	1.0	8.7	9.45
Short Tube #1	C-C-C-D-D-C	0.2	7.2	9.60
Short Tube #2	C-C-C-C-D-D-C	0.7	7.7	9.50
Short Tube #3	C-C-C-C-C-D-D-C	0.5	10.0	9.60

Table 3. Summary of Long Tube results.

Cathode Voltage [kV]	Beam Current [kA]	Input Power [GW]	Total Peak Power [MW]	RF Conversion Efficiency	Diode Impedance [ohms]
475	3.49	1.66	371	0.22	136
508	3.83	1.95	420	0.22	133
533	4.06	2.16	453	0.21	131
566	4.39	2.48	487	0.20	129
576	4.52	2.60	494	0.19	128
601	4.86	2.92	519	0.18	124
627	5.19	3.26	545	0.17	121

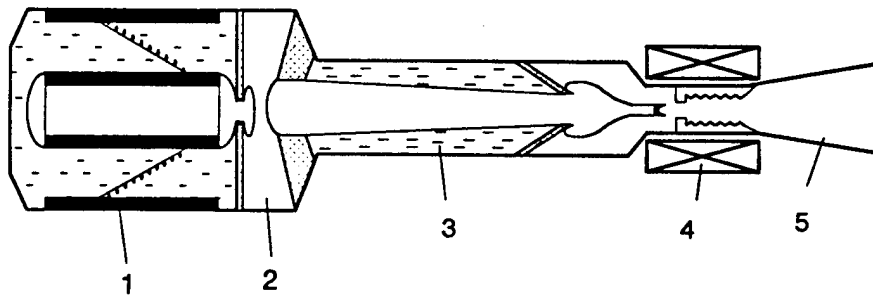


Fig 1. Cut-away diagram of Sinus-6. (The various components are described in the text.)

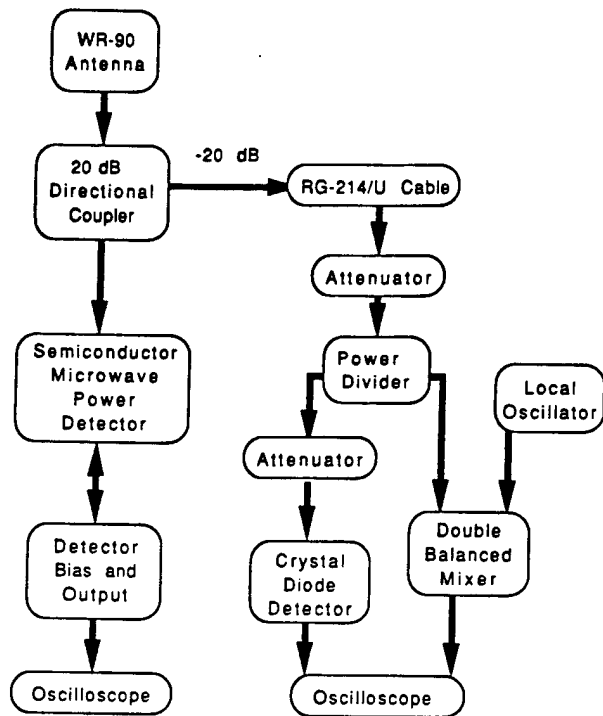


Fig 2. Block diagram of power measurement scheme.

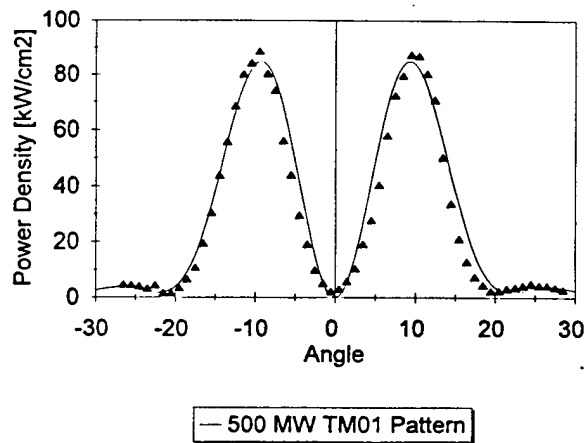


Fig 3. Radiation pattern from Long Tube.

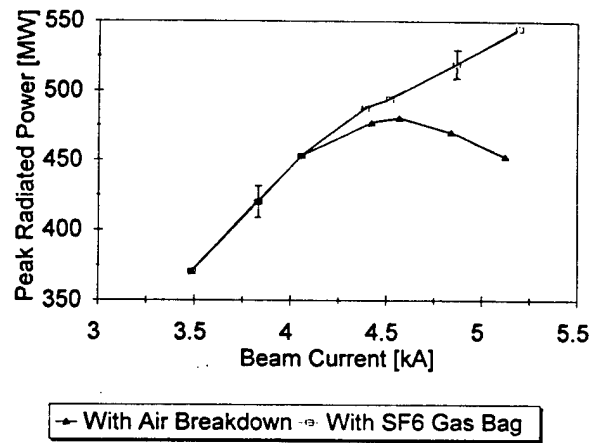


Fig 4. Dependence of power radiated from Long Tube on beam current.

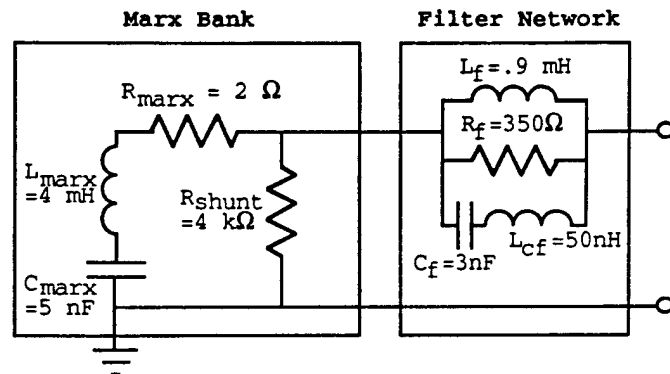


Fig 5. Equivalent circuit of modified PI-110A.

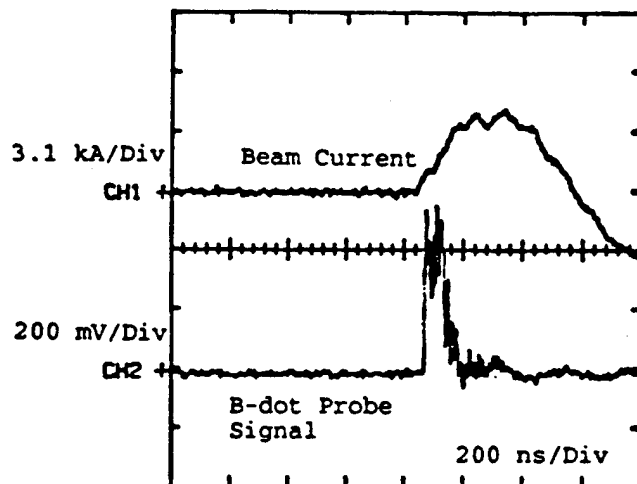


Fig 6. Typical output radiation from long pulse experiment measured using \dot{B} probe.

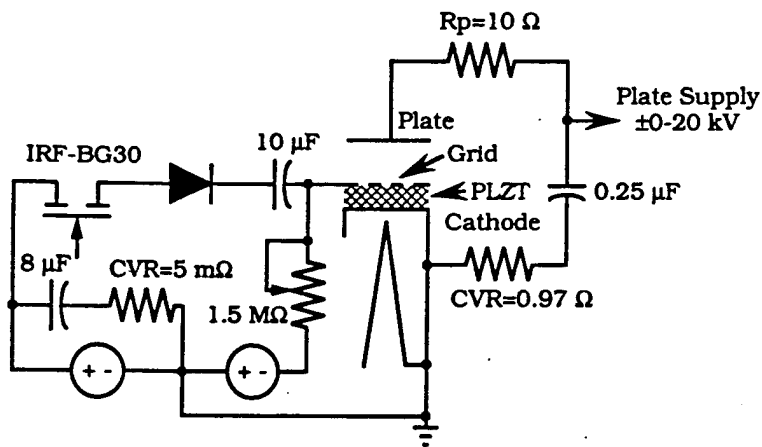


Fig 7. Configuration for ferroelectric cathode experiment.

Acknowledgements

This work is supported by U.S. Air Force Office of Scientific Research Grant F49620-94-1-0087DEF and Air Force Office of Scientific Research Instrumentation Grant F49620-93-1-0585. Acquisition of the Sinus-6 was funded by the Air Force Phillips Laboratory, Advanced Weapons and Survivability Directorate, Air Force Materiel Command, Kirtland AFB, New Mexico. Particle-in-cell simulation support was provided by Dr. R. W. Lemke (Sandia National Laboratories, Albuquerque, New Mexico).

Appendix C: Papers in Print Pertaining to Sinus-6 BWO

Efficiency Enhancement of High Power Vacuum BWO's Using Nonuniform Slow Wave Structures

Larald D. Moreland, Edl Schamiloglu, *Member, IEEE*, Raymond W. Lemke, S. D. Korovin, V. V. Rostov, A. M. Roitman, Kyle J. Hendricks, and T. A. Spencer

Abstract—The Sinus-6, a high-power relativistic repetitively-pulsed electron beam accelerator, is used to drive various slow wave structures in a BWO configuration in vacuum. Peak output power of about 550 MW at 9.45 GHz was radiated in an 8-ns pulse. We describe experiments which study the relative efficiencies of microwave generation from a two-stage nonuniform amplitude slow wave structure and its variations without an initial stage. Experimental results are compared with 2.5 D particle-in-cell computer simulations. Our results suggest that prebunching the electron beam in the initial section of the nonuniform BWO results in increased microwave generation efficiency. Furthermore, simulations reveal that, in addition to the backward propagating surface harmonic of the TM_{01} mode, backward and forward propagating volume harmonics with phase velocity twice that of the surface harmonic play an important role in high-power microwave generation and radiation.

I. INTRODUCTION

THERE have been many experimental and theoretical studies of high-power backward wave oscillators (BWO's) [1]. The majority of the work within the United States involved slow wave structures with uniform ripple amplitudes and periods. Analyses have shown that nonuniform BWO's can be designed to yield higher beam-to-microwave power conversion efficiency than uniform BWO's [2], [3]. In a nonuniform BWO, variations in the coupling impedance or phase velocity affect the interaction between the electron beam and electromagnetic modes along the length of the tube. The coupling impedance between the slow space charge wave on the electron beam and the surface harmonic of the backward TM_{01} mode can be modified by varying the ripple amplitude, or by varying the magnetic field distribution within the tube.

Manuscript received October 4, 1993; revised May 22, 1994. The work at the University of New Mexico was supported by the Air Force Office of Scientific Research under Grant F429620-92-J-0157DEF. The work at Sandia National Laboratories was supported in part by Air Force Phillips Laboratory and the Department of Energy.

L. Moreland and E. Schamiloglu are with the Pulsed Power and Plasma Science Laboratory, Department of Electrical and Computer Engineering, University of New Mexico, Albuquerque, NM 87131 USA.

R. W. Lemke is with Department 1241, Sandia National Laboratories, Albuquerque, NM 87185 USA.

S. D. Korovin, V. V. Rostov, and A. M. Roitman are with the Institute of High Current Electronics, Siberian Branch, Russian Academy of Sciences, Tomsk, Russia.

K. J. Hendricks and T. A. Spencer are with Phillips Laboratory, Advanced Weapons and Survivability Directorate, Air Force Materiel Command, Kirtland Air Force Base, NM 87117 USA.

IEEE Log Number 9404586.

The phase velocity of this harmonic can be varied along the length of the tube by gradually changing the period of the ripples. The efficiencies for converting input beam power into RF radiation using uniform BWO's have been reported to be as large as 15% [2]. Work in the former Soviet Union on nonuniform BWO's has shown experimental measurements of RF efficiencies exceeding 40%, and theoretical predictions indicate efficiencies may reach 75% in the absence of space charge effects [2], [3].

The goal of this study is to define the physics of the nonuniform BWO, which may reveal methods of further improving the efficiency of microwave generation using the Sinus-6 accelerator. In particular, we seek to quantify the use of a shallow ripple-amplitude initial section as a prebuncher to yield high efficiency operation. Experimental results are presented which contrast the operation of a nonuniform BWO both with and without such a prebuncher. A simple model analyzing the changes in electron energies and their relative phases along the length of a nonuniform amplitude BWO provided insight into the mechanism for improved efficiency using a prebuncher [2], [3].

The complexity of the nonuniform BWO experiment precludes an exact theoretical analysis using analytical methods. Therefore, particle-in-cell (PIC) simulation is the most feasible approach to investigating the physics of the nonuniform BWO. To this end, we have performed simulation studies of the experimental configurations using the 2.5 D, relativistic, fully electromagnetic PIC code TWOQUICK [4]. This code is a derivative of MAGIC [5].

This paper describes results to-date from a systematic program to investigate RF efficiencies of uniform and nonuniform BWO's using the Sinus-6 repetitively-pulsed electron beam accelerator. The Sinus-6 was designed and constructed jointly by the Institute of High Current Electronics and the Institute of Electrophysics, and was installed at the University of New Mexico in June 1992. The advantage of this accelerator is that it easily yields hundreds of BWO test shots in a single day, which makes it feasible to compare experimental results with theoretical calculations and particle simulations. The remainder of this paper is organized as follows. Section II describes the experimental setup and is followed in Section III by a discussion of the experimental measurements. A discussion of the PIC code simulation results is covered in Section IV, in addition to comparisons with experimental results. Finally, conclusions from this study and plans for future work are

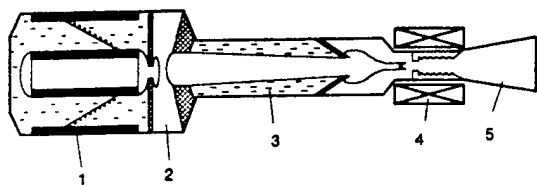


Fig. 1. Cut-away diagram of the Sinus-6 accelerator. The Tesla transformer (1) steps up the voltage from 300 V to 700 kV. The high voltage switch (2) is a nitrogen-filled spark gap, which is pressurized to 16 atm. The oil-filled adiabatic transmission line (3) matches the $22\ \Omega$ impedance of the pulse forming line to the $\sim 100\ \Omega$ impedance of the vacuum diode. The magnetic field coils (4) enclose the magnetically insulated coaxial vacuum diode which uses an explosive-emission graphite cathode. A conical horn antenna (5) is used for extracting microwave radiation.

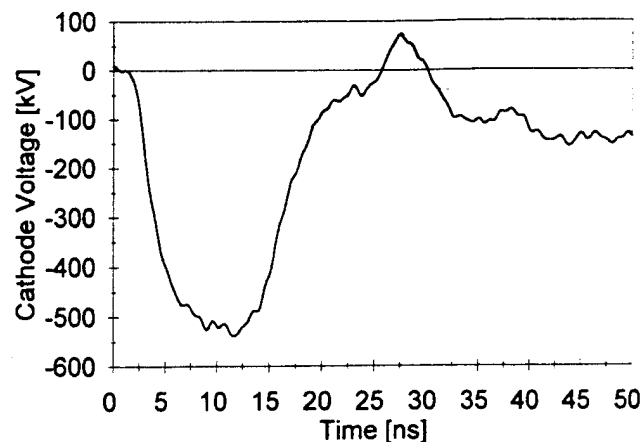
outlined in Section V. The Appendix provides additional detail on the calibration of the microwave measurements.

II. EXPERIMENTAL SETUP

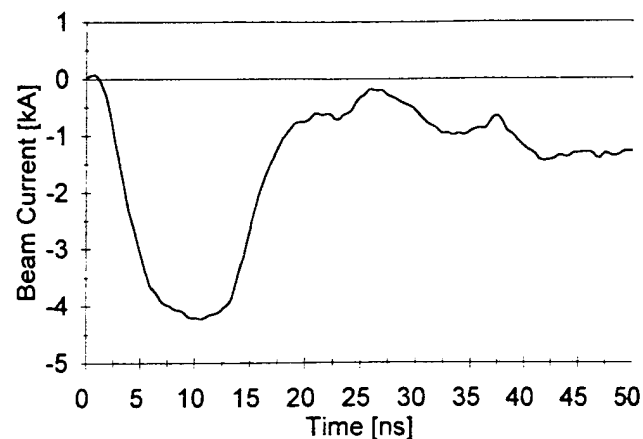
Fig. 1 is a cut-away diagram of the Sinus-6. The Tesla transformer (1) steps up the voltage from 300 V to 700 kV. An open ferromagnetic core is used in the Tesla transformer, which provides a high coupling coefficient between the transformer windings. The pulse forming line is contained within the Tesla transformer, permitting both increased efficiency and an overall compact system. The high voltage switch (2) is a nitrogen-filled spark gap, which is pressurized to 16 atm. By adjusting the pressure the spark gap voltage can be varied from 350 to 700 kV. The oil-filled adiabatic transmission line (3) matches the $22\ \Omega$ impedance of the pulse forming line to the $\sim 100\ \Omega$ impedance of the vacuum diode. The magnetically insulated coaxial vacuum diode uses an explosive-emission graphite cathode. The diameter of the annular electron beam is 2 cm with a beam thickness of 1 mm, confirmed using a witness plate damage diagnostic. A magnetic field with magnitude up to 3.0 T, used to confine the electron beam, is generated by a pulsed solenoid system (4). The pulsed system provides a magnetic pulse duration of 3 ms and requires 10 s to recharge. The Sinus-6 can generate electron beams at a pulse repetition rate of 200 Hz, but is presently operating at 0.1 Hz due to constraints imposed by the magnetic field system.

The Anode-Cathode (A-K) gap spacing and applied magnetic field were held constant and the resultant diode impedance was about $125\ \Omega$, depending on the cathode potential. The electron beam pulse has a full width, half maximum (FWHM) temporal duration of about 12 ns. Fig. 2 shows typical voltage and current waveforms. The voltage was measured using a capacitive divider, and the current was measured using a Rogowski coil. By adjusting the pressure in the spark gap, cathode voltages from 400 to 650 kV were tested with corresponding beam currents ranging from 3 to 5 kA.

Total peak radiated power measurements were made using both a semiconductor microwave detector and a crystal diode detector, indicated schematically in Fig. 3. Power density measurements were made 1.6 m downstream from a conical horn antenna which has a maximum diameter of 15 cm. The total power was calculated by numerically integrating the



(a)



(b)

Fig. 2. Typical voltage and current waveforms from the Sinus-6 accelerator. (a) The cathode voltage. (b) The corresponding beam current.

radiation pattern that was experimentally mapped. The radiated frequency was measured by heterodyning the RF signal against a known oscillator frequency.

The basic tube studied in this work is a nonuniform amplitude configuration we simply call "Long Tube." This tube is a two stage slow wave structure constructed from individual rings for each ripple period. Each ring is a trapezoidally shaped annulus with a width of 1.5 cm (corresponding to a ripple period of 1.5 cm) and a maximum radius of 1.65 cm. Four different rings were used, and their parameters are listed in Table I. In addition to this basic tube, variations we call Short Tubes #1-#3 were also studied to elucidate the role of the initial stage of the Long Tube. As is evident from Table II, the short tubes are variations of the second stage of the Long Tube.

During its first year of operation at the University of New Mexico, the Sinus-6 has accumulated over 10 000 single shots.

III. EXPERIMENTAL RESULTS

In this section we present experimental data describing the performance of the Long Tube and its shorter variations. Kovalev and colleagues [2] proposed that BWO efficiency can be improved by bunching the electrons in a weak electric

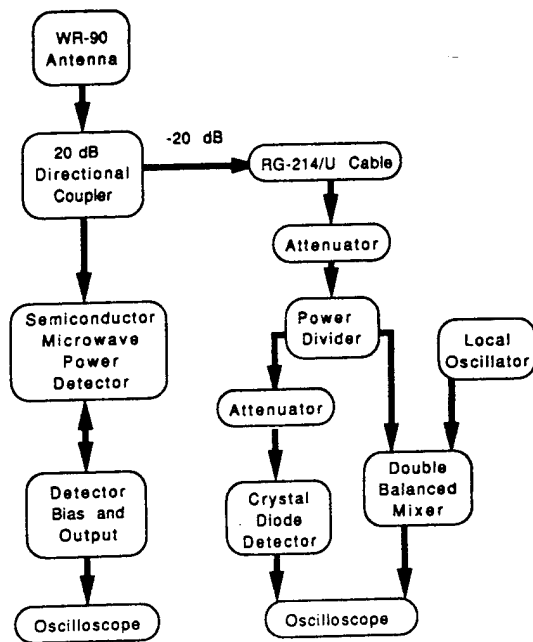


Fig. 3. Diagram of the experimental setup used to measure microwave power and frequency. A semiconductor microwave power detector is used to measure radiated power density (left), and a crystal diode and a balanced mixer are used to measure microwave power density and frequency, respectively (right).

TABLE I
DIMENSIONS OF SLOW WAVE STRUCTURE RINGS

Ring Type	Maximum Radius [cm]	Minimum Radius [cm]	Average Radius [cm]	Ripple Amplitude [cm]	Ripple Period [cm]
A	1.65	1.45	1.550	0.100	1.50
B	1.65	1.38	1.515	0.135	1.50
C	1.65	1.20	1.425	0.225	1.50
D	1.65	1.15	1.400	0.250	1.50

TABLE II
SUMMARY OF EXPERIMENTAL TUBE CONFIGURATIONS AND COMPARISONS

	Tube Configuration	Relative Power	Crystal Diode Detector Pulse Width [ns]	Frequency ± 0.05 [GHz]
Long Tube	A-A-B-B-B-C-C-C-D-D-C	1.0	8.7	9.45
Short Tube #1	C-C-C-D-D-C	0.2	7.2	9.60
Short Tube #2	C-C-C-C-D-D-C	0.7	7.7	9.50
Short Tube #3	C-C-C-C-C-D-D-C	0.5	10.0	9.60

field region at the beginning of the tube, and extracting the kinetic energy from the electrons in a strong electric field at the end of the tube. This electric field configuration can be achieved by constructing the initial section using shallow ripple-amplitude waveguide (weak coupling impedance) and the output section using deeper ripple-amplitude waveguide (stronger coupling impedance). The Long Tube was designed based on this principle, and we refer to the initial section as a "prebuncher."

The tests with the short tubes were performed to understand the role of the initial section of the two stage BWO. To ensure that efficiency enhancement observed using the Long Tube is due to the initial prebunching section, experiments were performed using short tubes of various lengths. Short Tube #1

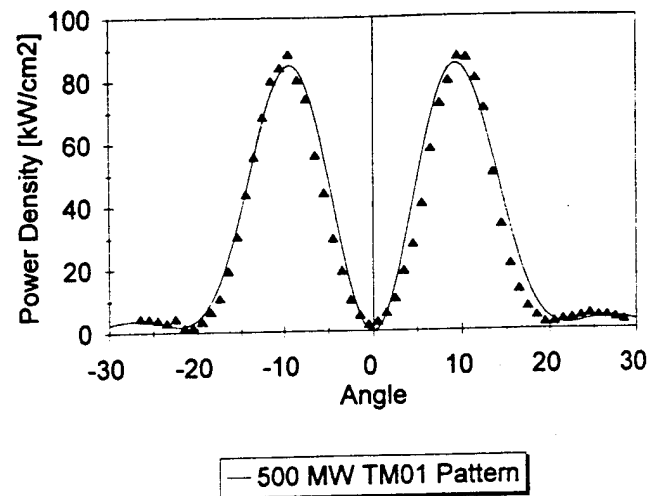


Fig. 4. Measured and calculated radiation pattern for a TM_{01} mode. The plotted curve is the calculated radiation pattern from [6] for a 500 MW TM_{01} mode. Numerical integration of the data points yields a total peak power of 450 MW.

is the output section of the Long Tube. Short Tubes #2 and #3 are longer to achieve a start current range corresponding to the Long Tube, but without an initial prebunching section. The parameters of the tubes are summarized in Table II.

Power density measurements were made using the setup described above in Fig. 3. A typical mode pattern radiated by the Long Tube and measured 1.6 m from the output antenna is shown in Fig. 4. The beam parameters used were 500 kV and 4 kA, and each data point was the average of 3 to 5 shots. The calculated TM_{01} radiation pattern [6] for a total peak power of 500 MW is indicated by the solid line in Fig. 4. For comparison, the data points were integrated numerically to yield a total power of 450 MW, in good agreement with the calculated mode pattern. Since the radiation pattern was found to be insensitive to slight changes in frequency, it was sufficient to measure the power density at the maximum electric field in order to ascertain the total radiated power. Fig. 5 and 6 present simultaneous power density measurements of the output of the Long Tube obtained using the semiconductor microwave power and crystal diode detector, respectively. Note that the crystal diode detector has a considerably faster response than the semiconductor microwave power detector. (See the Appendix for additional details on the power measurements.)

We now present results from our investigation of the efficiency of microwave generation using the Long Tube. Fig. 7 shows the dependence of peak radiated power on electron beam current. Each data point in the figure represents the average of 5 shots and the error bar represents the typical scatter in the data. The beam current was changed by varying the pressure in the spark gap switch and the applied voltage to the cathode. The A-K gap and applied magnetic field were held constant for all shots. (The cathode voltage and other parameters used to generate Fig. 7 and 9 are summarized in Table III.) In this parameter scan the measured frequency remained constant at 9.45 ± 0.05 GHz.

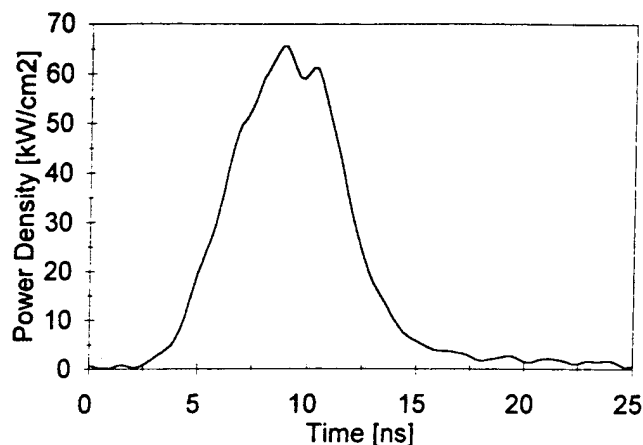


Fig. 5. Profile of RF pulse using semiconductor microwave power detector.

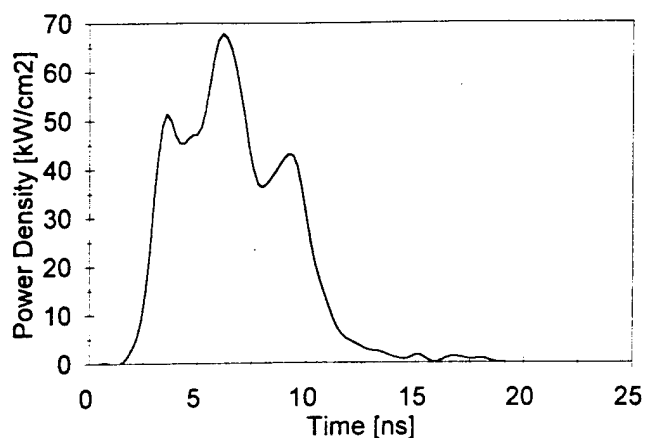


Fig. 6. Profile of RF pulse using crystal diode detector (for the same RF pulse as Fig. 5).

TABLE III
SUMMARY OF RESULTS FROM LONG TUBE. TOTAL PEAK
MICROWAVE POWER MEASUREMENTS MADE USING SF₆ GAS BAG

Cathode Voltage [kV]	Beam Current [kA]	Input Power [GW]	Total Peak Power [MW]	RF Conversion Efficiency	Diode Impedance [ohms]
475	3.49	1.66	371	0.22	136
508	3.83	1.95	420	0.22	133
533	4.06	2.16	453	0.21	131
566	4.39	2.48	487	0.20	129
576	4.52	2.60	494	0.19	128
601	4.86	2.92	519	0.18	124
627	5.19	3.26	545	0.17	121

At beam currents above 4 kA air breakdown near the output window was observed. Time-integrated photographs showed a bright annular ring of plasma consistent with a TM₀₁ mode pattern. In order to suppress the air breakdown, a gas bag filled with SF₆ was placed in front of the horn antenna. The amplitude and pulse duration from the crystal diode detector were observed to increase when the gas bag was used. Fig. 7 shows the effect of using a gas bag on the microwave power measurements. Fig. 8 shows the response of the crystal diode both with and without the SF₆ gas bag.

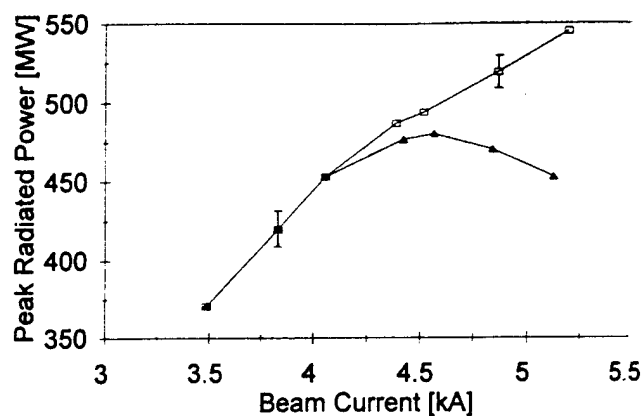


Fig. 7. Peak radiated power from the Long Tube as a function of beam current. The A-K gap and magnetic field were held constant. The cathode voltage can be found in Table II for each data point. A gas bag of SF₆ was placed over the output antenna to prevent air breakdown at the higher beam currents.

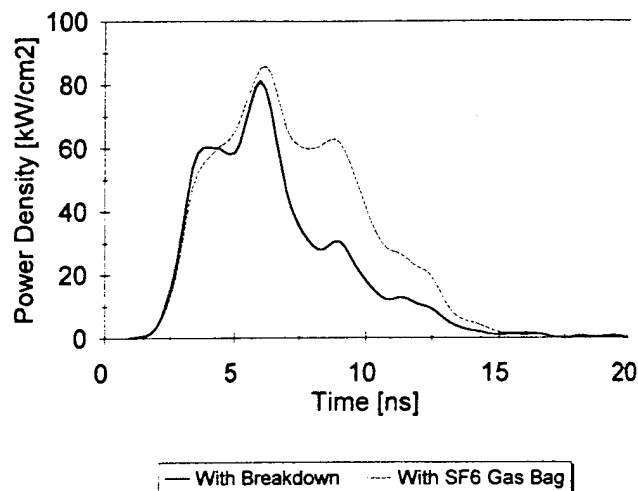


Fig. 8. Comparison of RF pulse profile with air breakdown and with a SF₆-filled gas bag. The dashed line is the RF profile from the crystal diode detector with SF₆ gas bag. The solid line shows the RF profile when air breakdown occurs in front of the output antenna.

The RF conversion efficiency was calculated by comparing the measured peak radiated microwave power to the peak input beam power. (Input beam power was obtained by multiplying the cathode voltage by the beam current.) The dependence of this efficiency on electron beam current is shown in Fig. 9. The maximum RF conversion efficiency was 22% and occurred at the lower beam currents. (Note that the efficiency decreases for increasing beam current. This will be discussed later in Section IV.) The maximum radiated microwave power was about 550 MW, which corresponds to an efficiency of 17%.

As was discussed earlier, to elucidate the role of the pre-buncher on the efficiency of the Long Tube, experiments were performed with various short tubes (parameters summarized in Tables I and II). Sections of cutoff pipe were added to the

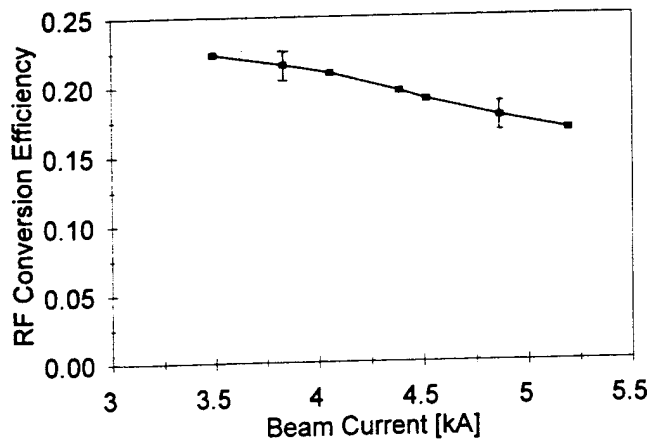


Fig. 9. The RF conversion efficiency for the Long Tube as a function of beam current. The A-K gap and magnetic field were held constant. The cathode voltage can be found in Table III for each data point. A gas bag filled with SF_6 was placed over the output antenna to prevent air breakdown at the higher beam currents.

modified tubes to ensure that the A-K gap and the tapered magnetic field at the end of the tube remained constant. The beam parameters were approximately 4 kA and 500 kV, which were chosen to avoid air breakdown associated with the Long Tube. Data showing the peak output microwave power generated by the Long Tube and the three short tubes are given in Table II. It is clear that none of the short tubes are as efficient as the Long Tube, and among the short tubes, Short Tube #2 is the most efficient, with an efficiency of about 15%. Consistent with the lower relative powers indicated, air breakdown was never observed with the short tubes, even when they were driven at the highest input beam powers. Because the growth rate of the RF fields must decrease with the difference between the beam current and the start current, we infer from the RF pulse widths in Table II, that the start current for the Long Tube is between the start currents for Short Tubes #2 and #3. Therefore, we conclude that the increased efficiency of the Long Tube is a result of the prebuncher and cannot be attributed to the ratio of beam current to start current.

IV. NUMERICAL SIMULATION OF THE NONUNIFORM BWO

The complexity of the nonuniform BWO geometry precludes an exact theoretical analysis using analytical methods. In this case, particle-in-cell (PIC) simulation is the most feasible approach to investigating the physics of this tube. We present results from a simulation study performed using the 2.5 D, relativistic, fully electromagnetic, PIC code TWOQUICK [4]. The latter is a derivative of MAGIC [5].

The goal of this study is to define the physics of the nonuniform BWO, which may reveal methods of improving the efficiency of the Sinus-6 tube and BWO's in general. In particular, it is of interest to quantify the use of nonuniform amplitude ripples versus uniform ripples to achieve high efficiency.

Although we have attempted to model the Sinus-6 experimental configuration as closely as possible, it must be

remembered that, with all its sophistication, the PIC simulation is still an approximation to reality, and therefore it is possible for model dependent phenomena to arise that influence the results. These phenomena are either physical or numerical. It is worthwhile giving an example of each kind, both of which can significantly affect the results of microwave tube simulations, and which had to be dealt with in our investigation of the nonuniform BWO.

In the numerical model the tube is constructed of a single piece of perfectly conducting material. This implies an infinite Q (quality factor) for a cavity, or a Q which is dependent only on the bulk geometry in the case of an aperture for power extraction, as in the BWO. This is not the case in reality. The nonuniform BWO, for example, is constructed by stacking rings made of lossy conducting material. Thus, RF power can be lost in the material and through the ring interfaces, in addition to the radiation aperture. Therefore the Q of the experimental apparatus is lower than in the numerical simulation. The difference is exacerbated if a lossy plasma is unintentionally created in the experiment (by an electron beam impinging on a conductor, for example). This difference in Q is particularly important for microwave tube simulations because the higher intrinsic Q can affect both the temporal behavior and absolute value of the RF output power (compared to the experiment), in addition to giving rise to sharp resonances, which may be significantly broadened in the lower Q experimental configuration, and therefore are of no consequence.

High frequency numerical noise is inherent in PIC simulations and is due to the discretization of the physical problem. Usually the frequency of numerical noise is much higher than the RF frequency of interest, and the associated amplitude is negligible compared to that of the phenomenon under investigation. However, for certain numerical configurations the noise becomes unstable at some high frequency (e.g., 50 GHz), and saturates at an amplitude that ruins the fidelity of the simulation. In TWOQUICK (and MAGIC) a time biased field solver [7] provides intrinsic damping to eliminate high frequency noise. Damping occurs at all frequencies, although to a much lesser extent at the lower frequencies usually of interest. Nevertheless, numerical damping can significantly reduce the output power radiated in a microwave tube simulation, an effect that becomes more pronounced as the frequency of interest increases. Fortunately, numerical damping can be controlled.

It was necessary to use the time biased field solver to eliminate large amplitude noise in our simulations of the nonuniform BWO. Measurements of output power from a benchmark experiment using a uniform BWO consisting of eight periods of type C sections were used to adjust the time biased coefficients [7] until the noise was eliminated and the simulated value of power agreed with the measured value. A uniform tube was chosen for the benchmark comparison because its behavior is relatively well understood compared to the nonuniform BWO. The amount of numerical damping (other than zero damping) did not change the simulated qualitative behavior of this tube; that is, the physics does not depend on the degree of damping.

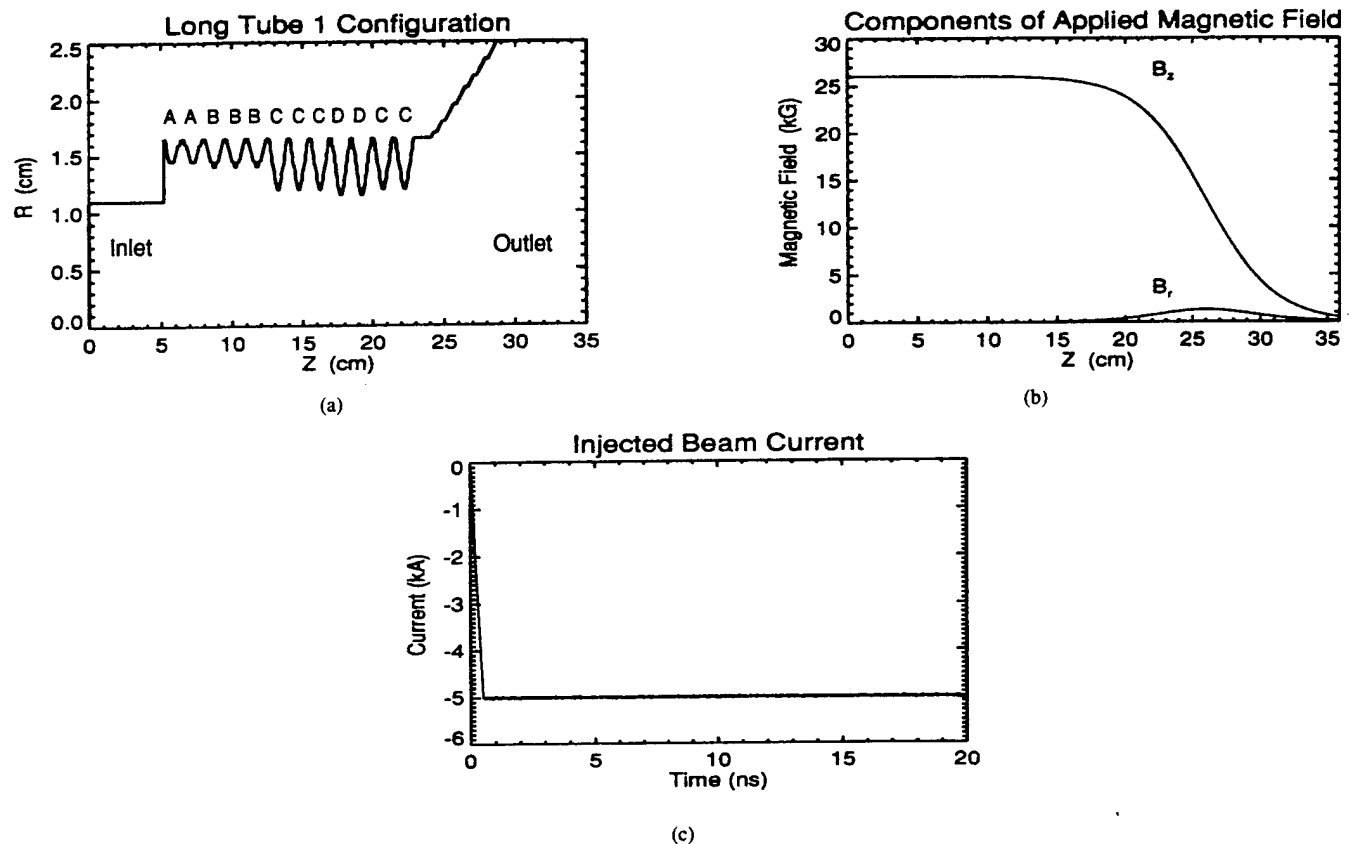


Fig. 10. (a) Simulation configuration for the Long Tube. The geometry is cylindrical, with the z -axis corresponding to the axis of symmetry. The various rings comprising the slow wave structure are labeled with corresponding upper case letters. The electron beam is injected at the inlet. Microwaves are radiated at the outlet. (b) Axial dependence of the applied magnetic guide field at the radial location $r = 1.0$ cm, which corresponds to the outer edge of the beam. (c) Time history of the injected beam current.

Initially the exact beam temporal pulse was used in the simulations. It was discovered that the RF power saturated several nanoseconds later than in the experiment, a consequence of the intrinsically high quality factor discussed above. In the interest of reducing the simulation time, and since we were only interested in the saturated state, which depends on the beam equilibrium and geometry, the current rise time was shortened to one nanosecond. This change did not affect the saturated state.

Diligent comparison of numerical results with experimental measurements gives us confidence that our PIC simulations reveal the internal dynamics of the nonuniform BWO. In addition to the average radiated power, experimental data that can be compared directly with simulation results consists of tube efficiency, oscillation frequency, and the geometrical pattern of the radiated mode. Variations in the values of these quantities with changes in the geometrical configuration or beam parameters, in addition to other information provided by the simulation, can be used to deduce changes in the internal dynamics of the experiment. We present results that pertain to the Long Tube discussed above.

The simulation configuration for the Long Tube is shown in Fig. 10(a). The tube has cylindrical symmetry with the r -axis vertical and the z -axis horizontal. The latter corresponds to the axis of symmetry. Rotating the figure 360° about the axis of symmetry (perpendicular to the page) produces the complete geometry.

In Fig. 10(a) the inlet corresponds to the end of the diode A-K gap, and is the plane at which the electron beam is injected into the problem. Similar to the experiment, the inlet is at the beginning of a section of waveguide that cuts off radiation having the expected oscillation frequency (9.5 GHz). Thus little or no radiation will reach the injection plane. Therefore the latter is chosen to be a perfect conductor in the simulation.

The outlet represents the waveguide which, in the experiment, leads to the antenna. Reflections at the outlet could possibly have a significant impact on the dynamics of a simulation [8]. We consider only cases for which the outlet is perfectly transmitting to waves of the expected frequency. The transmission coefficient at this boundary is insensitive to small changes ($< 10\%$) in wave oscillation frequency.

The applied external magnetic field used to guide the electron beam is patterned after the actual magnetic field used in experiments. Shown in Fig. 10(b) are the axial dependencies of B_z and B_r , which were calculated using the expressions

$$B_z(r, z) = \frac{B_0}{[1 + e^{(z-z')/\alpha}]} \quad (1)$$

and

$$B_r(r, z) = \frac{B_0}{2\alpha} r \frac{e^{(z-z')/\alpha}}{[1 + e^{(z-z')/\alpha}]^2} \quad (2)$$

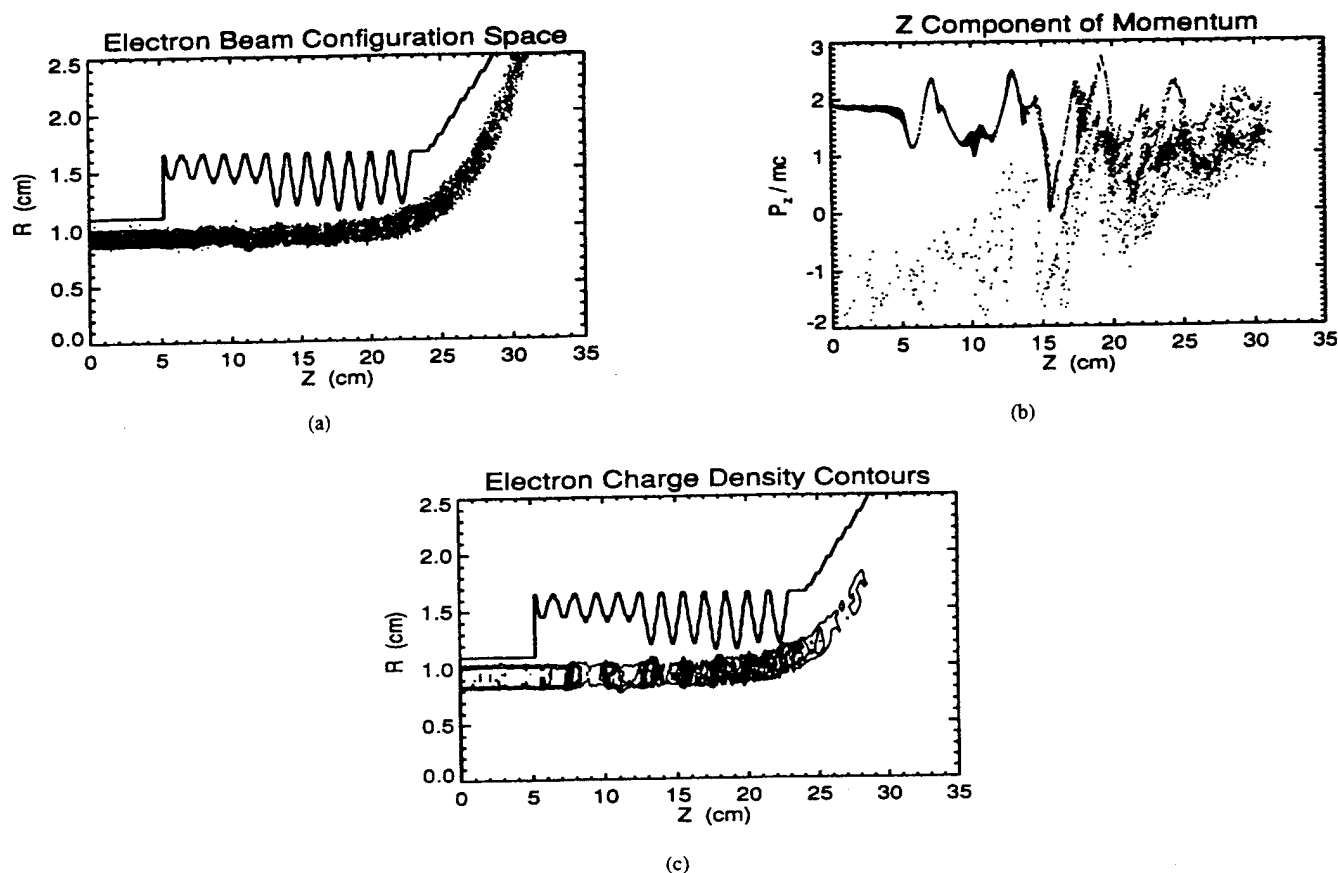


Fig. 11. (a) Configuration space of the electron beam. (b) Particle plot of the z component of axial momentum, which is normalized to the electron mass (m) times the speed of light (c). (c) Contour plot of electron charge density, which shows that the electron beam is modulated with a spatial wavelength of 1.5 times the ripple period. This corresponds to the wavelength of the slow space charge wave.

where $B_0 = 2.6$ T is the magnitude of the magnetic field in the region where it is uniform. The free parameters α and z' are set to ensure that the electron beam is dumped beyond the interaction region, but before the outlet. The magnetic field described by (1) and (2) satisfies the divergence equation.

Beam equilibrium parameters are based on experimentally measured values. The simulated current pulse is shown in Fig. 10(c) for a 5 kA electron beam. For reasons explained above an artificially short rise time of 1 ns is used. The corresponding voltage is 600 kV, and is constant throughout the current pulse. Simulations show that the saturated steady state is not affected by the initial transient state of the electron beam.

The electron beam cross section is annular. The associated current density is uniform in the annulus, which is defined by $0.85 \leq r \leq 1.00$ cm.

It is expected that the dynamics of the nonuniform BWO will be fundamentally similar to a conventional uniform BWO, in which a slow space-charge wave of the beam interacts with the surface harmonic of the backward traveling transverse magnetic (TM) wave [9]. Simulations confirm this hypothesis, but reveal some differences that may result in higher efficiencies for tubes with nonuniform slow wave structures.

Fig. 11–15 contain results from a simulation of the Long Tube. Fig. 11 shows several different representations of the beam at a time when the RF fields in the nonuniform BWO have saturated, about 14.9 ns into the simulation.

Fig. 11(a) shows the position of the beam relative to the geometry, and the location of the beam dump. The beam, which is injected at the left-hand boundary (inlet) and travels from left to right, has clearly become modulated (bunched).

Fig. 11(b) is a plot of the (relativistic) electron axial momentum versus z (z component of phase space), which shows that velocity modulation first occurs in the section comprised of relatively shallow rings (AABBB) where the coupling of the beam to the surface wave of the slow wave structure is weak. In addition, the spatial variation of the momentum in this section is longer (about twice as long) than downstream, which suggests the presence of multiple space harmonics of the axial electric field (E_z).

A plot of electron charge density contours, shown in Fig. 11(c), confirms that significant density modulation has occurred, which is indicative of a strong interaction between the slow space charge wave on the beam with the slow TM surface harmonic associated with the slow wave structure. The period of the density bunches is the wavelength of the slow space charge wave, which is about 1.5 times the structure period in this case. Comparison of Fig. 11(c) with Fig. 11(a) and 11(b) shows that density bunches coincide with a local minimum in the axial momentum, which implies that electrons in a bunch always experience a decelerating electric field, a minimum requirement for efficient operation.

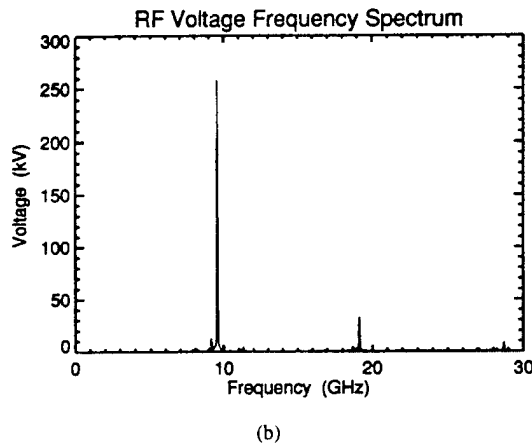
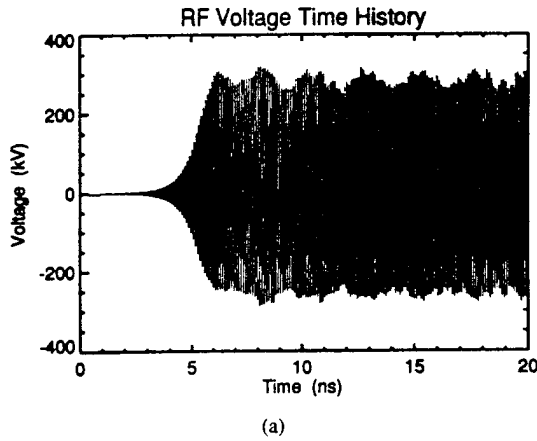


Fig. 12. (a) Time history of the voltage across the gap between the second and third B sections in the Long Tube, and (b) the corresponding frequency spectrum.

The oscillation frequency of the nonuniform BWO is obtained from the Fourier transform (FT) of the time history of the RF voltage across the gap formed by the second and third B sections (see Fig. 10(a)). The RF voltage time history is shown in Fig. 12(a), and the corresponding frequency spectrum in Fig. 12(b). The FT is taken for times after the voltage has reached a steady state, which in this case corresponds to $6 \leq t \leq 20$ ns. This temporal window sets the frequency resolution to $\Delta f = 35$ MHz. The oscillation frequency of the dominant TM mode is $9.57 \text{ GHz} \pm \Delta f$, which is in good agreement with the measured value of 9.45 GHz.

The temporal modulation of the RF voltage evident in Fig. 12(a) is due to a small amplitude (10 kV) oscillation with a frequency of 9.14 GHz, which is possibly due to reflections at the downstream end of the tube. This oscillation is not present in simulations in which the last C section is replaced with an A section, which provides a less abrupt transition to the outlet waveguide, and does not affect the average value of the RF output power.

The component of RF voltage at 19.14 GHz (twice the dominant frequency) is due to radiation generated by the corresponding harmonic of the modulated beam current. The amplitudes of these higher harmonics increase downstream as the beam current becomes more modulated due to its interaction inside the slow wave structure.

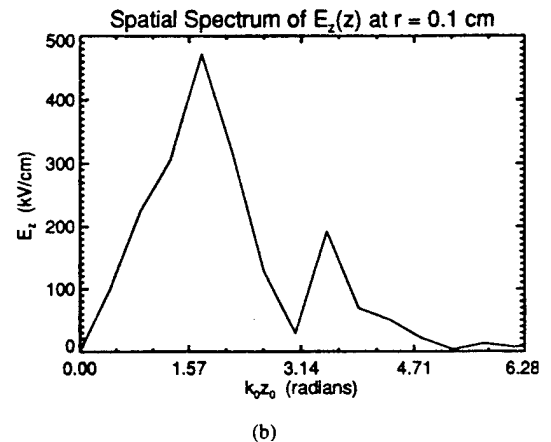
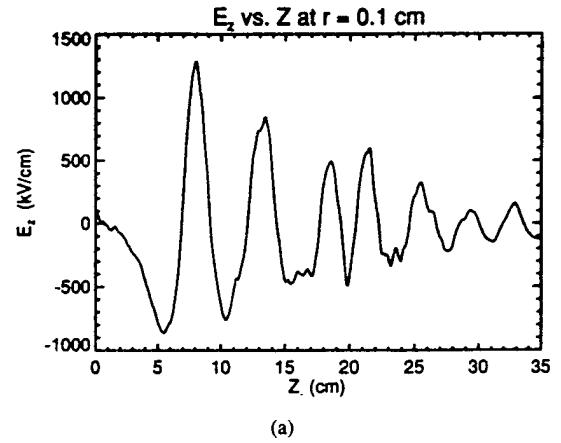


Fig. 13. (a) Plot of E_z versus z at $r = 0.1$ cm. (b) The corresponding Fourier spectrum showing the dominant space harmonics.

To understand the interaction of the beam with the electric fields in the nonuniform BWO it is necessary to isolate the dominant space harmonics of E_z . Plots of the total E_z versus r (from simulations) only reveal that E_z has a maximum on axis. In conjunction with the known oscillation frequency this indicates the presence of a fast TM_{01} space harmonic (phase velocity greater than the speed of light c), the frequency of which is set by the radius of the waveguide wall. For this reason we refer to this harmonic as a volume harmonic, to distinguish it from the surface harmonic that is due to the slow wave structure.

The dominant space harmonics are isolated by Fourier transforming a plot of E_z versus z for a particular radial location (axial slice plot). Fig. 13(a) is such a plot for $r = 0.1$ cm, near the axis. Fig. 13(b) is the spatial spectrum of E_z , which shows two dominant space harmonics having normalized wave numbers of $(k_{n=0})z_0 = 1.75$ and $(k_{n=-1})z_0 = 3.50$, corresponding to wavelengths of $\lambda_0 = 5.4$ cm and $\lambda_{-1} = 2.7$ cm, respectively. Knowing the oscillation frequency, basic considerations indicate that the long wavelength component must be the TM_{01} volume harmonic. The shorter wavelength is similar to the spatial separation of the density bunches observed in Fig. 11, and must be associated with the TM_{01} surface harmonic, the phase velocity of which is less than c .

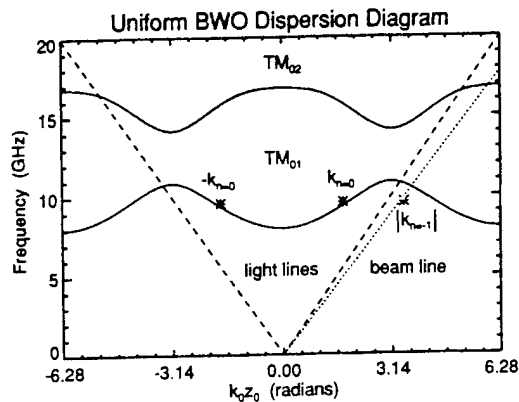


Fig. 14. Approximate dispersion diagram for Long Tube showing the first two passbands, which are labeled TM_{01} and TM_{02} . The wavenumbers obtained from the simulation are designated by an asterisk and are labeled $-k_{n=0}$, $k_{n=0}$, and $k_{n=-1}$, which correspond to backward and forward traveling fast waves (volume harmonics), and the backward traveling slow wave (surface harmonic), respectively.

The previous notation used for the wave numbers of the dominant space harmonics comes from the Floquet series for the total E_z component, which is given by

$$E_z(r, z, t) = \sum_{n=-\infty}^{\infty} \tilde{E}_{zn}(r) e^{i(\omega t - k_n z)} \quad (3)$$

where $k_n = k_0 + (2\pi n)/z_0$, z_0 is the ripple period, and ω is the angular frequency of oscillation.

The eigenfunction $\tilde{E}_{zn}(r)$ satisfies Bessel's equation of order zero, which has the solution

$$\tilde{E}_{zn}(r) = A_n J_0(\Gamma_n r) \quad (4)$$

where $\Gamma_n = \sqrt{(\omega/c)^2 - k_n^2}$, and J_0 is the Bessel function of the first kind of order 0.

For fast waves Γ_n is real, so E_z has a maximum on the axis (where J_0 is largest). For slow waves Γ_n is imaginary. In this case the radial dependence of $\tilde{E}_{zn}(r)$ is given by the modified Bessel function of the 1st kind $I_0(-i\Gamma_n r)$, which implies that the maximum of the eigenfunction occurs away from the axis. A more rigorous analysis shows that the maximum occurs near the surface of the slow wave structure.

The nature of the dominant space harmonics is further clarified by superimposing the wave numbers obtained from the simulation (all having an oscillation frequency of 9.57 GHz) on a dispersion diagram for the nonuniform BWO. The latter is approximated by the dispersion diagram for an infinitely long uniform BWO consisting of C type sections and no electron beam, which is shown in Fig. 14. The beam line corresponding to a voltage of 600 kV is superimposed on the diagram. The wave numbers obtained from the simulation are indicated by asterisks and are labeled with the notation used above to indicate volume and surface harmonics.

It is clear from Fig. 14 that the surface harmonic ($k_{n=-1}$) is indeed the slow TM_{01} backward traveling wave that couples to the space charge wave on the electron beam. A self consistent analysis shows that the beam space charge wave distorts the TM_{01} mode where they intersect [9], which explains why the frequency of the surface harmonic does not coincide with a point on the curve in Fig. 14.

Also indicated in Fig. 14 are forward and backward traveling volume harmonics, both of which are part of the TM_{01} mode. The backward traveling component arises from the interaction of the beam with the electromagnetic fields inside the slow wave structure. It coexists with the surface harmonic, and is necessary to satisfy boundary conditions at the cutoff waveguide. The amplitude of the backward traveling volume harmonic relative to that of the surface harmonic depends in part on the ripple depth and the waveguide radius [10]. For a given waveguide radius increasing the ripple depth increases the amplitude of the surface harmonic relative to that of the backward traveling volume harmonic. While both are reflected at the cutoff waveguide, it is the forward traveling component which escapes the BWO and comprises the radiated power.

The instantaneous output power is obtained by calculating the integral of the Poynting flux over the cross section of the outlet. Fig. 15(a) compares the input beam power with the RF output power, the average of which is 453 MW. The corresponding tube efficiency is 15.3%, which is lower than the 18% measured in the experiments for the same beam parameters.

The Fourier spectrum of the power, Fig. 15(b), is computed after subtracting off the average value. The power associated with an oscillation frequency f occurs at a frequency $2f$. The frequency spectrum shows that most of the power is radiated in the TM_{01} mode ($2f = 19.14$ GHz), which agrees with the experiment. The output power is modulated due to the 9.14 GHz oscillation observed in the RF voltage (Fig. 12), which is attributed to finite length effects.

Changing the beam parameters to current = 3.5 kA and voltage = 500 kV reduces the output RF power to 329 MW, but increased the tube efficiency to 18.8%, in qualitative agreement with the experiment. This behavior may be an indication that the larger current is too high relative to the start current (I_{st}) for efficient operation [8], [11].

A nonlinear theory [8] of the uniform BWO indicates that tube efficiency begins to decrease for beam currents greater than about $2.5I_{st}$ due to overbunching of the beam produced by the large amplitude RF electric field. The start current for the Long Tube was calculated by performing a series of simulations in which the current is reduced until no growth occurs during a 20 ns interval; that is, until the linear growth rate is effectively zero. In this manner we deduced a start current of $I_{st} = 0.9$ kA for the Long Tube, which includes end reflections. Thus, both beam currents used in simulations are larger than the start current. In qualitative agreement with theory, the larger of the two currents results in lower tube efficiency.

The picture of nonuniform BWO operation derived from simulations is that the beam interaction with the slow wave structure produces a TM_{01} mode that consists of backward traveling surface and volume harmonics, which correspond to slow and fast waves, respectively. The fast wave is reflected at the cutoff waveguide producing a forward traveling volume harmonic, which is radiated from the downstream end of the BWO (where it may also be partially reflected). Similar behavior is observed in simulations of BWO's with uniform amplitude ripples.

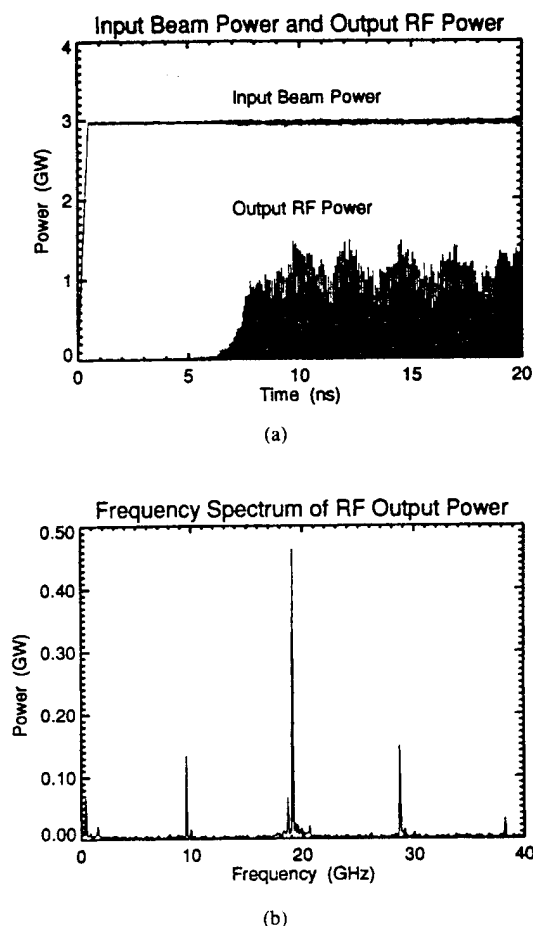


Fig. 15. (a) Input beam power and output RF power versus time for the Long Tube, and (b) the corresponding Fourier spectrum. The average output RF power is 453 MW, which is calculated in the region where the power has saturated ($t > 10$ ns). The frequency spectrum indicates that most of the radiated power is in the TM_{01} mode.

Reflections of the various wave harmonics at the discontinuities in the nonuniform BWO produce standing waves. Thus, the energy conversion process will in general depend on both the slow and fast waves [10]. An appropriate choice of the slow wave structure length would allow the beam to give up energy directly to the fast wave through transit time effects. In addition, the standing wave electric field causes the beam to become bunched prior to entering the region of strong coupling, as shown in Fig. 11. This prebunching would enhance the interaction of the beam with the surface wave, thereby increasing the tube efficiency.

The possibility of increasing power conversion efficiency through prebunching and enhanced transit time effects represents an advantage of using a nonuniform amplitude slow wave structure over an uniform structure in a BWO. Ongoing work suggests that prebunching the beam increases the efficiency of a BWO in general [12], [13], independent of structure type.

V. CONCLUSION

The purpose of this study was to elucidate the role of the initial section of the two stage BWO. The nonuniform amplitude BWO (the Long Tube) had peak RF efficiencies ranging

from 17 to 22%, depending on the input beam parameters. The highest peak power generated was about 550 MW at a cathode voltage of 620 kV and beam current of 5.2 kA. The microwave pulse duration was typically 8 ns at an RF frequency of 9.45 GHz. A gas bag filled with SF_6 placed around the horn antenna was necessary to suppress air breakdown at these power levels. Experiments showed that the RF efficiency of the Long Tube was considerably greater than the RF efficiency of comparable tubes without the prebunching section.

TWOQUICK simulations provided a comprehensive picture of the prebunching of the electron beam in the initial section of the nonuniform amplitude slow wave structure. There was good agreement between the experiment and simulation results.

The results from the PIC simulations indicate that, in addition to the surface harmonic of the backward wave, the forward traveling volume harmonics may play an important role in the energy exchange process in the BWO. We therefore propose that it may be possible to design an uniform BWO where the forward traveling volume harmonics can serve the role of a prebuncher. This is presently an area of investigation in our laboratory.

APPENDIX

A. Calibration of Semiconductor Microwave Power Detector

The operation of the semiconductor microwave power detector is based on the response of the fast electrons in the semiconductor to an applied RF electric field. The fast electrons cause the bulk resistance of the semiconductor to change. The semiconductor is located inside a WR-90 waveguide. The detector is biased by a 100- μ s, 50 V pulse and its transient voltage response, which is proportional to the RF pulse's power, is recorded by an oscilloscope. In our experiments, the semiconductor microwave power detector output was compared with a crystal diode detector, and independently calibrated using a magnetron. An advantage of the semiconductor microwave power detector is that it yields a video voltage pulse at the high-power levels being measured. The crystal detector, on the other hand, requires an attenuation of the RF pulse by over 70 dB in order to avoid damaging the crystal. Periodic calibration of the attenuation using a scalar network analyzer is required. These two detectors provide independent checks on the power measurements.

B. Comparison of Detector Responses

It is clear from Fig. 6, shown earlier, that the response time of the crystal detector is less than one nanosecond. Fig. 5, on the other hand, shows that the response of the semiconductor microwave power detector is several nanoseconds. In fact, the curves in Fig. 5 and 6 were found to match if the data from the crystal detector was averaged over two nanoseconds.

C. Effective Area of WR-90 Waveguide Antenna

We used an open-ended section of WR-90 waveguide as the receiving antenna for our microwave detectors. This waveguide has a geometric cross sectional area of 2.32 cm². Tests

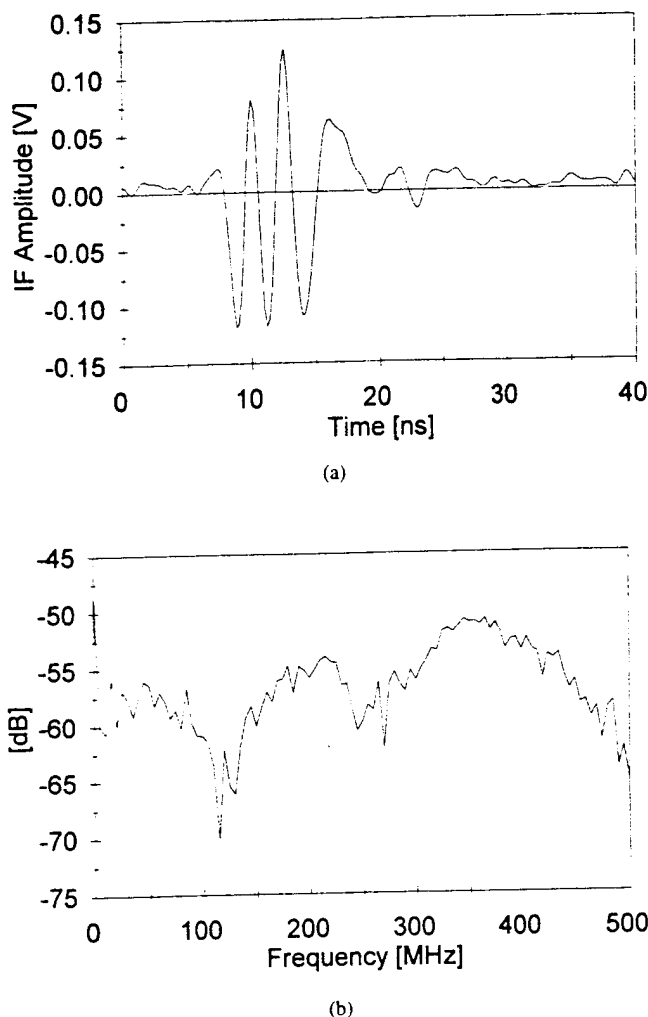


Fig. 16. (a) The intermediate frequency (IF) obtained by the mixing of the RF pulse with the local oscillator frequency. (b) The Fourier transform of the IF. The local oscillator frequency was 9.10 GHz. The Fourier transform shows that the main frequency component of this RF pulse is 9.45 GHz. Numerous shots were made at different local oscillator frequencies to confirm the RF frequency.

performed found that the effective area for open-ended WR-90 waveguide varied from 2.5 to 3.7 cm² for frequencies between 9 to 10 GHz. To calculate total radiated microwave power, we used the conservative value of 3.7 cm² for the effective area.

D. Frequency Measurements

To measure the radiated microwave frequency, the RF pulse is mixed with a local oscillator (LO) signal, as shown earlier in Fig. 3. The resultant intermediate frequency (IF) signal is displayed on an oscilloscope (Tektronix TDS 644A digitizing oscilloscope with a 2 gigasample per second sampling rate and a 500 MHz bandwidth). Fig. 16(a) shows the IF signal generated by mixing a 9.10 GHz LO signal with the radiated output from the Long Tube. Fig. 16(b) is the Fourier transform of this IF signal. From this figure, the dominant IF frequency is found to be 350 MHz which, when added to the LO frequency of 9.10 GHz, yields a primary RF frequency of 9.45 GHz. The IF measurements were made with the LO frequency both below and above the RF frequency to resolve

any ambiguities in the difference measurements. For a variety of LO frequencies, the main frequency component generated by the long tube was consistently measured to be 9.45 GHz.

REFERENCES

- [1] J. Benford and J. Swegle, *High-Power Microwaves*. Boston: Artech House, 1992, ch. 6.
- [2] N. F. Kovalev and V. I. Petrukina, "Ultra-relativistic carcinotron with a jump in beam-rf coupling," *Electr. Techn. SVCH*, vol. 7, pp. 101-105, 1977 (in Russian).
- [3] S. D. Korovin, S. D. Polevin, A. M. Roitman, and V. V. Rostov, "Relativistic backward wave tube with variable phase velocity," *Sov. Tech. Phys. Lett.*, vol. 18, pp. 265-266, 1992.
- [4] D. B. Seidel and T. D. Pointon, Sandia National Laboratories, private communication.
- [5] B. Goplen, R. E. Clark, J. McDonald, and W. M. Bollen, *Users Manual for MAGIC*, Rep. MRC/WDC-R-068, Mission Res. Corp., Alexandria, VA, 1983.
- [6] R. A. Koslover, Computer code "TM0n," SEAC, Albuquerque NM, 1988.
- [7] B. B. Godfrey, "Time-biased field solver for electromagnetic PIC codes," presented at Ninth Conf. Numerical Simulation of Plasmas, Northwestern University, Evanston, IL, June 30-July 2, 1980.
- [8] B. Levush, T. M. Antonsen, Jr., A. Bromborsky, W. Lou, and Y. Carmel, "Theory of relativistic backward-wave oscillators with end reflections," *IEEE Trans. Plasma Sci.*, vol. 20, pp. 263-280, 1992.
- [9] J. A. Swegle, J. W. Poukey, and G. T. Leifeste, "Backward wave oscillators with rippled wall resonators: analytic theory and numerical simulation," *Phys. Fluids*, vol. 28, pp. 2882-2894, 1985.
- [10] S. D. Korovin, S. D. Polevin, A. M. Roitman, and V. V. Rostov, "Influence of the traveling wave on efficiency of the relativistic BWO," *Sov. Tech. Phys. Lett.*, vol. 20, pp. 12-16, 1994.
- [11] J. A. Swegle, "Starting conditions for relativistic backward wave oscillators at low currents," *Phys. Fluids*, vol. 30, pp. 1201-1211, 1987.
- [12] R. W. Lemke, L. D. Moreland, E. Schamiloglu, S. D. Korovin, I. V. Pegel, and A. M. Roitman, "Numerical simulation of backward wave oscillators having nonuniform amplitude slow wave structures," presented at 21st IEEE Int. Conf. Plasma Sci., Santa Fe, NM, June 6-8, 1994.
- [13] D. Shiffler, University of New Mexico, private communication.



Larald D. Moreland received the B.S. and M.A. degrees in physics from California State University, Long Beach, in 1969 and 1972, respectively. He is currently a Ph.D. candidate in the Department of Electrical and Computer Engineering at the University of New Mexico, Albuquerque.

He joined the US Air Force in 1972 and became a C-5 navigator, with additional assignments at Space Division, Los Angeles AFS, working with the NAVSTAR Global Positioning System Joint Program Office and the Air Force Philips Laboratory, Kirtland AFB with the High Power Microwave Program. His research activities have included propagation of high-power microwaves, electron accelerators, and generation of microwaves from backward wave oscillators.



Edl Schamiloglu (M'90) received the B.S. degree in applied physics and nuclear engineering and the M.S. degree in plasma physics from Columbia University in 1979 and 1981, respectively. He received the Ph.D. degree from the Laboratory of Plasma Studies, Cornell University in 1988.

He joined the Department of Electrical and Computer Engineering at the University of New Mexico, Albuquerque in 1988, and is presently an Associate Professor. His research interests include charged-particle beam generation and propagation, ion sources, millimeter and infrared radiation sources, ion beam and plasma processing of materials, and plasma diagnostics.

Dr. Schamiloglu is a member of the American Physical Society.



Raymond W. Lemke received the B.S. degree in astrophysics and mathematics in 1976 and the Ph.D. degree in physics in 1988, both from the University of New Mexico, Albuquerque.

From 1978 through 1989, he was employed at the Air Force Phillips Laboratory (formerly Weapons Laboratory), Albuquerque, where he performed theoretical research in the areas of charged-particle beam propagation and high-power microwave generation. Since 1989 he has been at the Sandia National Laboratories, Albuquerque, where he currently works in the areas of high-power microwaves and inertial confinement fusion.



A. M. Roltman graduated from the Tomsk State University, Department of Physics in 1987.

He then joined the High Current Electronics Institute of the Russian Academy of Sciences. His research interests are in microwave electronics—in particular, the experimental and theoretical study of backward wave oscillators.



S. D. Korovin graduated from the Novosibirsk State University, Department of Physics in 1975. He received the Kandidat degree in 1981 and the Doctor of Sciences degree in 1991. Since 1975, he has been with the High Current Electronics Institute of the Russian Academy of Sciences, and is currently Head of the Physical Electronics laboratory. His research interests include electrodynamics of ultra-high frequencies, relativistic high-current electronics, and physics of high-current electron accelerators. He is the author of more than 60 scientific papers.



Kyle J. Hendricks received the B.S. and M.S. degrees from the University of Iowa in 1980 and 1982, respectively. He received the Ph.D. degree from the University of New Mexico in 1989.

Since 1983, his research interests have included narrow band high-power microwave (HPM) sources, electron beam diodes and propagation, pulse power systems, laboratory plasma systems, and diagnostic techniques for laboratory plasmas and HPM systems. He is presently leader for the Phillips Lab's narrow band HPM source group.

Dr. Hendricks received the 1988 USAF Research and Development Award for work on phase locking of Virtual Cathode Oscillators.



V. V. Rostov graduated from the Novosibirsk State University, Department of Physics in 1978. He received the Kandidat degree in 1985.

He joined the High Current Electronics Institute of the Russian Academy of Sciences in 1978. He is now leader of a research group dealing with theoretical investigations in microwave electronics.

Thomas A. Spencer was born in 1964 in Arlington, VA. He received the B.S. degree in nuclear science from Virginia Polytechnic Institute and State University in 1986, and the M.S.E. and Ph.D. degree in nuclear engineering from the University of Michigan, Ann Arbor, MI, in 1991 for work on high power microwave generation using a microsecond electron beam accelerator.

He was a Research Fellow at the University of Michigan in 1991 and detailed to the Phillips Laboratory as an IPA for continued research on high power microwave generation. He has been a high power microwave source engineer for the Phillips Laboratory at Kirtland AFB, NM, since 1992, where his present research activities include work on gyrotron backward wave oscillators, conventional backward wave oscillators, relativistic klystron amplifiers, magnetically insulated line oscillators, diode physics, novel cathodes, and RF atmospheric breakdown.

EFFECTS OF USING A NONUNIFORM-AMPLITUDE SLOW WAVE STRUCTURE IN A REPETITIVELY-PULSED, HIGH POWER RELATIVISTIC BACKWARD WAVE OSCILLATOR. + *

L. D. Moreland, E. Schamiloglu, R. Lemke,[§] J. Gahl, D. Shiffler
University of New Mexico
Department of Electrical and Computer Engineering
Albuquerque, New Mexico 87131

Abstract

The University of New Mexico Pulsed Power and Plasma Science Laboratory is conducting a systematic investigation of nonuniform-amplitude backward wave oscillators (BWOs) using the SINUS-6, a high power relativistic repetitively-pulsed electron beam accelerator. The Sinus-6 produces a 12 ns microwave pulse with a peak power of 600 MW at 9.6 GHz. Efficiencies of microwave generation using both uniform and nonuniform-amplitude BWOs are measured and compared with TWOQUICK (MAGIC) computer simulations. Each BWO structure is tested hundreds of times over a wide range of input parameters. The plentiful data allow for careful comparisons with theoretical models. Initial results confirm that prebunching the electron beam in a nonoscillating shallow ripple section results in increased microwave generation efficiency. Finally, experimental results from a high power serpentine mode converter based on a design of the Institute of Applied Physics, Nizhny Novgorod, Russia are also presented. The converter changes the dominant TM_{01} mode output of the BWO to a TE_{11} mode with very high conversion efficiency.

Introduction

There have been many experimental and theoretical studies of high power backward wave oscillators (BWOs) [1]. The majority of the work within the United States has used uniform amplitude and period slow wave structures. The efficiencies for converting input beam power into RF radiation using these devices have been reported to be as large as 15%. Work from the former Soviet Union on nonuniform BWOs has shown experimental measurements of RF efficiencies exceeding 40% and theoretical predictions indicate efficiencies may reach 75% [2,3].

This paper describes a systematic program at the University of New Mexico to investigate RF efficiencies of uniform and nonuniform BWOs using the Sinus-6 repetitively-pulsed electron beam accelerator. The advantage of this accelerator is that it easily yields hundreds of BWO test shots in a single day, which allows for careful comparison of experimental results with theoretical calculations.

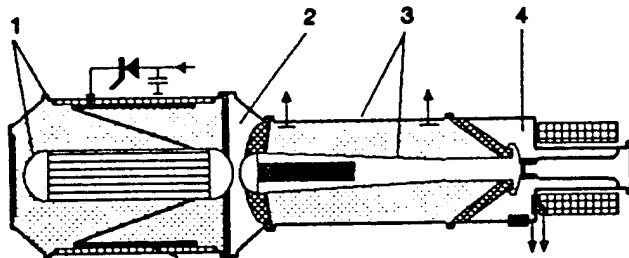


Fig. 1 Cut-away view of Sinus-6.

Sinus-6

The Sinus-6 (pronounced CEE-NUSS) is a high current, repetitively pulsed electron beam accelerator. Figure 1 is a cut-away diagram of the Sinus-6 with the following components: 1) Tesla transformer and pulse forming line which steps up the voltage from 300 V to 700 kV; 2) nitrogen-filled spark gap switch which is pressurized up to 18 atmospheres; by adjusting the nitrogen pressure, the spark gap voltage can be varied from 400 kV to 700 kV; 3) oil-filled adiabatic line which matches the 22 Ω input to a 100 Ω output; and 4) magnetically insulated coaxial vacuum diode with a cold explosive-emission graphite cathode. A magnetic field of 2.6 Tesla used to confine the electron beam is generated by a pulsed solenoid system. The pulsed system provides a magnetic pulse duration of 3 ms and requires 8 s to recharge. The Sinus-6 can rep rate its electron beam at 200 Hz but is currently operating at a single shot every 10 seconds, limited by the magnetic field system.

The electron beam pulse has a full width, half maximum (FWHM) temporal duration of 12 ns. Figure 2 shows voltage and current traces. By adjusting the pressure in the spark gap, cathode voltages from 400 to 650 kV were tested along with beam currents ranging from 3 to 5 kA.

For each different BWO structure, hundreds of test shots were made over the range of input parameters given above. The Sinus-6 provides a "work horse" to test many BWO structures over a wide range of input parameters. Within its first year of operation at the University of New Mexico, the Sinus-6 has accumulated over 10,000 single shots.

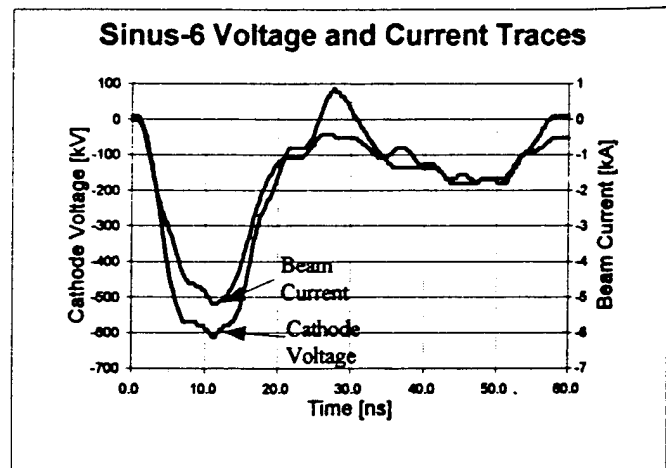


Fig. 2 Sinus-6 Voltage and Current Traces.

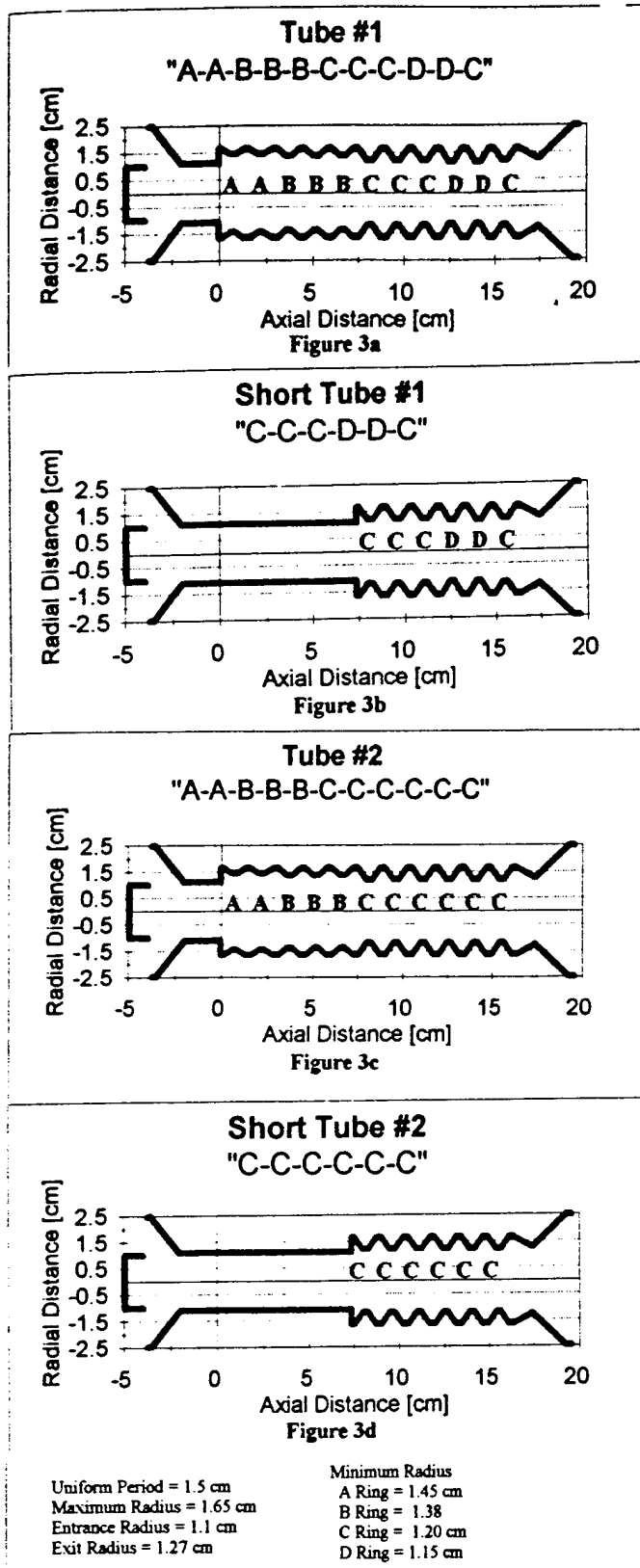


Fig. 3 Nonuniform-amplitude slow wave structures.

Analysis has shown that nonuniform BWOs can be designed to operate more efficiently than uniform BWOs [2,3]. A nonuniform BWO can be constructed by varying the amplitude of the ripple in the slow wave structure, or by varying the period of the ripple. Varying the amplitude of the ripple changes the coupling resistance between the slow surface and the TM_{01} modes. Varying the period of the ripples changes the phase velocity of the slow surface wave. Our initial studies used a nonuniform-amplitude BWO structure provided by the High Current Electronics Institute, Tomsk, Russia. Figure 3a shows this structure. Variations of this structure were tested. The BWO structure is constructed from individual rings for each ripple period. In this manner, the structure can be quickly changed to any combination of ripple amplitudes. Each ring has a width of 1.5 cm (corresponding to a ripple period of 1.5 cm) and a maximum radius of 1.65 cm. Four different types of rings were used with ripple amplitudes of 1.0 mm, 1.35 mm, 2.25 mm and 2.5 mm. The original structure studied (referred to as Tube #1 and shown in Fig. 3a) has two sections, a first section with shallow ripples followed by a second section with deeper ripples. A variation of this tube is Short Tube #1 where the shallow first section is eliminated, as shown in Fig. 3b. A second variation of our original tube is shown in Figs. 3c and 3d where the amplitude of the six ripple periods of the second section are the same. These tubes are referred to as Tube #2 and Short Tube #2.

Experimental Results

Variations in Slow Wave Structure Amplitude

We now present experimental data in which the BWO sections were tested separately. The RF efficiency was obtained by dividing the maximum total RF power divided by the total peak input beam power (cathode voltage multiplied by beam current). When the shallow section was tested alone, no RF radiation was detected with beam currents up to 4.5 kA. When the second stage of deeper ripples was tested alone (Short Tube #1), the RF efficiency was plotted as a function of input beam power in Fig. 4 and has a maximum RF efficiency of about 5%. The full BWO (Tube #1) results are plotted in Fig. 5 and indicate a maximum efficiency of 25 to 30%. The results for Tube #2 and Short Tube #2 are shown in Figs. 6 and 7. When the RF efficiencies for Tube #1 and Tube #2 are compared with beam current, as shown in Figs. 8 and 9, the maximum RF efficiency occurs at approximately twice the start current.

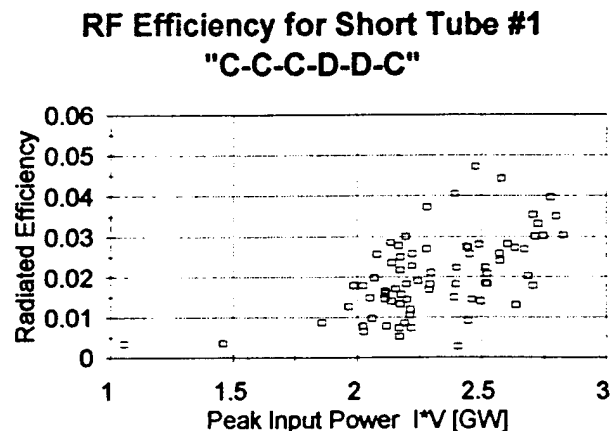


Fig. 4 RF efficiency for short tube #1.

RF Efficiencies for Tube #1
"A-A-B-B-B-C-C-C-D-D-C"

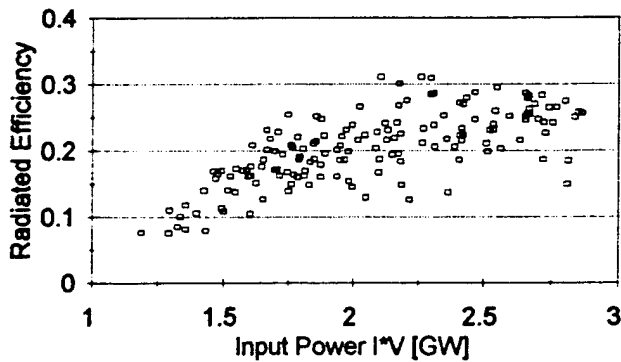


Fig. 5 RF efficiency for tube #1.

RF Efficiency for Tube #1
"A-B-B-B-C-C-C-D-D-C"

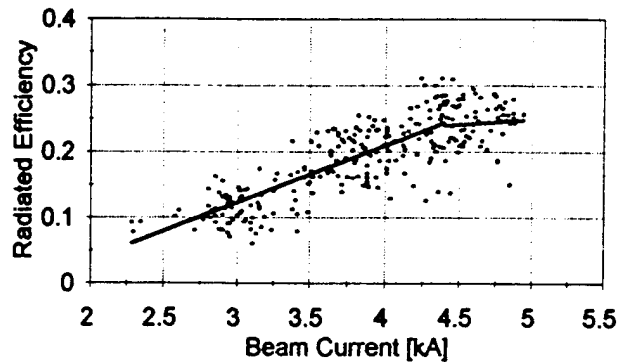


Fig. 8 RF efficiency for tube #1.

RF Efficiencies for Tube #2
"A-A-B-B-B-C-C-C-C-C"

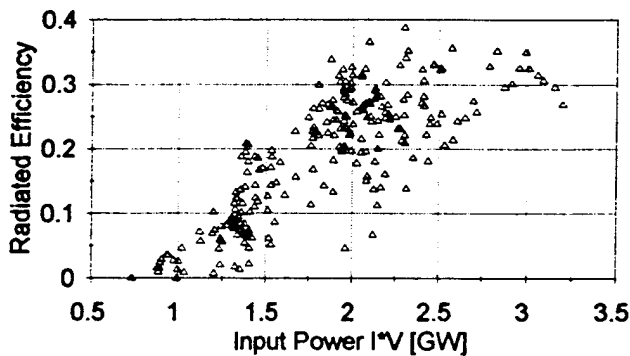


Fig. 6 RF efficiency for tube #2.

RF Efficiency for Tube #2
"A-A-B-B-B-C-C-C-C-C"

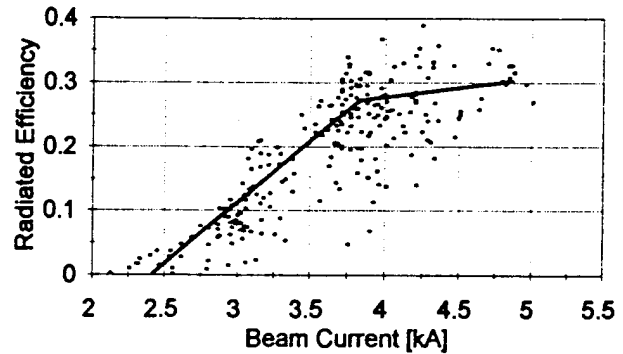


Fig. 9 RF efficiency for tube #2.

RF Efficiency for Short Tube #2
"C-C-C-C-C-C"

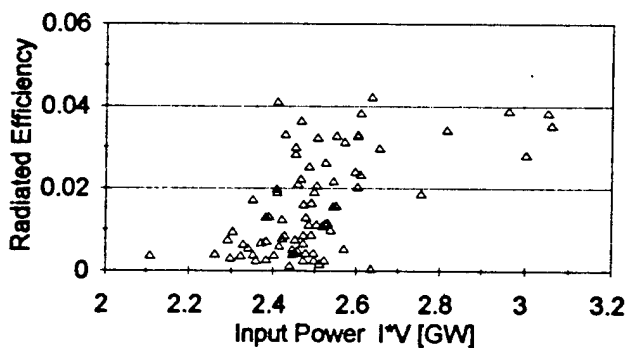


Fig. 7 RF efficiency for short tube #2.

Sinus-6 Peak Power Density
TM₀₁ Mode With Conical Horn Antenna

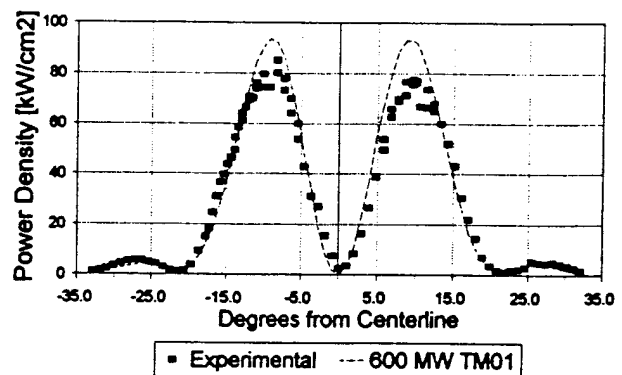


Fig. 10 TM₀₁ radiation pattern.

Mode Conversion

The TM₀₁ mode is the dominant mode in the slow wave structure. A conical horn antenna with a diameter of 15 cm was used to radiate the RF energy. Power density measurements were made in the horizontal plane at a distance of 1.7 m from the horn aperture. Using the nonuniform-amplitude BWO (Tube #1), the radiation pattern from the TM₀₁ mode is shown in Fig. 10. The measurements in Fig. 10 are compared with the calculated radiation pattern from a 600 MW TM₀₁ source [4]. Next a mode

converter based on a design of the Institute of Applied Physics, Nizhny Novgorod, Russia was used to convert the TM₀₁ mode to a TE₁₁ mode [5]. The measured radiation pattern using the mode converter is shown in Fig. 11 and compared with a Gaussian radiation pattern of 600 MW total power and a half power beam width of 12 degrees. The mode conversion efficiency was nearly 100% within the limits of experimental error. The Gaussian-like radiation pattern is useful for applications, such as high power radars [6].

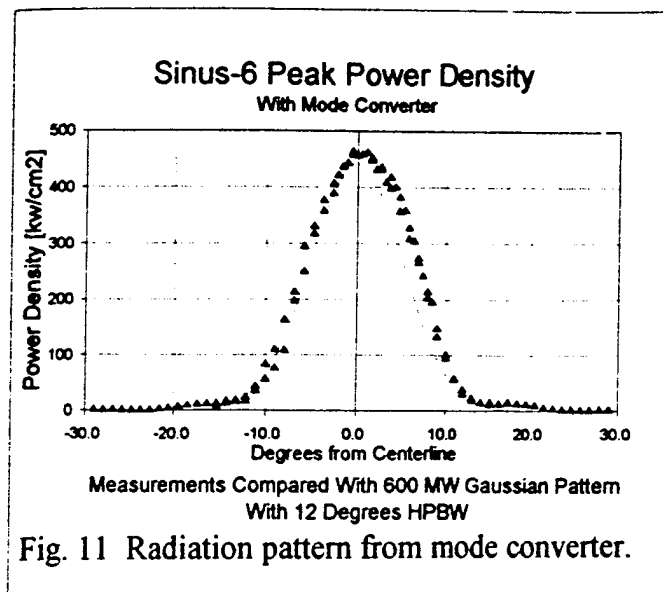


Fig. 11 Radiation pattern from mode converter.

MAGIC Comparisons

Sandia National Laboratories' version of MAGIC, TWOQUICK, was used to perform computer simulations to compare with experimental results. The computer simulations allow "snapshots" to be taken of the BWO operation. By calculating and plotting the charge density of the electron beam throughout the tube, the slow surface wave on the beam can be observed, as shown in Fig. 12. These results indicated that the surface wave has a wavelength equal to approximately 1.5 ripple periods. By plotting the intensity of the longitudinal electric field within the tube, the volume mode of the tube can be observed. The wavelength of the volume mode is approximately equal to 3 ripple periods. The tube is overmoded and the extraction of power through the volume mode minimizes microwave breakdown problems.

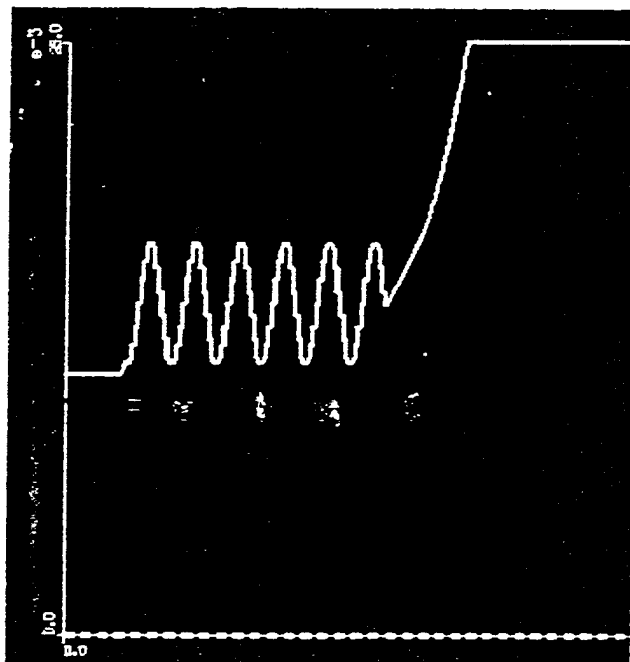


Fig. 12 Electron beam density from TWOQUICK (MAGIC) simulation.

Simulations provided good agreement with experimental measurements of the operating frequency of the BWOs. Simulations confirm that the first stage of shallow ripples in the original two-section structure does not oscillate. Simulations also indicate that efficient BWO operation occurs when the beam current is approximately twice the starting current for the oscillating section, consistent with experimental measurements. Simulations could not predict actual operating efficiencies in all cases due to resonance effects associated with artificially low power losses in the ideal model. However, the scaling appears to be in agreement provided that the tubes are not oscillating in the vicinity of a cavity resonance in the simulations.

Conclusions

The nonuniform-amplitude BWOs tested resulted in peak RF efficiencies of 25 to 35%. The maximum values for RF efficiencies occurred at approximately twice the start current, consistent with computer simulations. When the two sections were tested individually, the first shallow ripple section did not radiate measurable RF power and the second deeper ripple section showed RF efficiencies of less than 5%. The increased efficiency of the two section BWOs can be attributed to the prebunching of the electron beam by the nonoscillating first section.

TWOQUICK MAGIC simulations provided insight into the interaction of the surface mode and volume mode inside the slow wave structure. Simulation results were sensitive to the cavity Q's of the set-up. Agreement with experimental measurements were good when the simulations were not near resonance.

A high power serpentine mode converter resulted in power densities as large as 450 kW/cm² being measured 1.7 m from the radiating antenna. The TM₀₁ to TE₁₁ conversion efficiency was nearly 100%, consistent with theoretical predictions [5]

+ In collaboration with the High Current Electronics Institute, Tomsk, Russia.

* Research supported by AFOSR Grant # F49620-92-J-0157DEF
§ Sandia National Laboratories, Albuquerque, NM

References

- [1] See, for example, J. Benford and J. Swegle, High-Power Microwaves. Boston: Artech House, 1992 and references therein.
- [2] N. F. Kovalev, V. I. Petrukhina, and A. V. Smorgnoski, Radiotekh Elektron. 20, 1547 (1975).
- [3] S. D. Korovin, S. D. Polevin, A. M. Roitman, and V. V. Rostov, "Relativistic backward wave tube with variable phase velocity," Sov. Tech. Phys. Lett. 18(4) (1992).
- [4] R. A. Koslover, Computer code "TM0n" (SEAC, Albuquerque NW) (1988).
- [5] D. V. Vinogradov and G. G. Denisov, "The conversion of waves in a bent waveguide with a variable curvature," Radiofizika, 33, 726 (1990).
- [6] G. A. Mesyats, paper presented at the 1992 IEEE Microwave Theory and Techniques Society Symposium, Albuquerque, NM, June 2, 1992.

EFFICIENCY ENHANCEMENT OF HIGH POWER VACUUM BACKWARD-WAVE OSCILLATORS DRIVEN BY SHORT PULSE AND LONG PULSE ELECTRON BEAMS

EDL SCHAMIOGLU,* L. D. MORELAND,* R. W. LEMKE,** J. M. GAHL,* and
C. GRABOWSKI*

* University of New Mexico, Department of Electrical and Computer Engineering,
Albuquerque, NM 87131, USA

** Department 1241, Sandia National Laboratories, P.O. Box 5800, Albuquerque,
NM 87185, USA

ABSTRACT

The efficiency of high peak power microwave generation in X-band backward-wave oscillators is being studied. In the short pulse regime, nonuniform slow wave structures are driven by a Sinus-6 repetitively-pulsed, relativistic electron beam accelerator. Peak microwave power exceeding 550 MW at 9.45 GHz has been measured in an 8 ns pulse with corresponding beam-to-microwave conversion efficiency of 18%, although efficiencies approaching 25% were achieved at reduced input beam parameters. A high power serpentine mode convertor transforms the TM_{01} mode radiated by the BWO to a Gaussian-like TE_{11} mode, resulting in power densities as large as 450 kW/cm^2 being measured 1.6 m downstream from the conical horn antenna. Experimental results are compared with 2.5 D particle-in-cell simulations which reveal that, in addition to the backward propagating surface harmonic of the TM_{01} mode, backward and forward propagating volume harmonics with phase velocity twice that of the surface harmonic play an important role in efficient microwave generation. In a companion set of experiments, a modified PI-110A long pulse, single shot electron beam accelerator is used to drive slow wave structures originally developed for the short pulse experiments. Preliminary results indicate that microwave radiation terminates within the first 100 ns of the 450 ns electron beam pulse.

INTRODUCTION

High power vacuum backward-wave oscillators (BWOs) have been studied experimentally and theoretically for about 25 years.^{1,2} The resurgence in interest in these classical microwave tubes coincided with the development of pulsed high current relativistic electron beam accelerators. A BWO consists of an electron beam guided by a strong axial magnetic field propagating through a rippled-wall slow wave structure. Researchers in the Former Soviet Union developed several generations of repetitively-pulsed electron beam accelerators based on Tesla transformer technology with very high coupling efficiencies.² In addition, they developed "advanced" slow wave structures which were motivated by theoretical analyses showing that nonuniform BWOs can be designed to yield higher beam-to-microwave power conversion efficiencies than uniform BWOs (see Refs. 3,4 and references therein). In a nonuniform BWO, variations in the coupling impedance or phase velocity affect the interaction between the

electron beam and electromagnetic modes along the length of the tube. The coupling impedance between the slow space charge wave on the electron beam and the surface harmonic of the backward TM_{01} mode can be modified by varying the ripple amplitude, or by varying the magnetic field distribution within the tube. The phase velocity of this harmonic can be varied along the length of the tube by gradually changing the period of the ripples. The efficiencies for converting input beam power into RF radiation using uniform BWOs have been reported to be as large as 15%.³ Work in the former Soviet Union on nonuniform BWOs has shown experimental measurements of RF efficiencies exceeding 40%, and theoretical predictions indicate efficiencies may reach 75% in the absence of space charge.^{3,4}

This paper describes progress-to-date on a research program that seeks to define the physics of efficient microwave generation in uniform and nonuniform BWOs in both the short pulse and long pulse regimes in vacuum. Basic understanding is gained from experiments using the Sinus-6, a repetitively-pulsed relativistic electron beam accelerator developed jointly by the High Current Electronics Institute (Tomsk, Russia) and the Institute of Electrophysics (Ekaterinburg, Russia). This basic understanding is then transferred to the PI-110A long pulse experiments. It is expected that technological innovation¹ will lead to advances in long pulse BWO operation beyond the 100 ns barrier² that researchers have typically faced. One of the goals of this study is to increase microwave generation efficiency in vacuum without resorting to a plasma fill.⁵

SHORT PULSE EXPERIMENTS

Recent experiments using the Sinus-6 seek to quantify the use of a shallow ripple-amplitude initial section of a nonuniform amplitude BWO as a prebuncher to increase microwave generation efficiency. Figure 1 presents a diagram of the Sinus-6. The Tesla transformer (1) steps up the voltage from 300 V to 700 kV. An open ferromagnetic core is used in the Tesla transformer, which provides a high coupling coefficient between the transformer windings. The pulse forming line is contained within the Tesla transformer, permitting both increased efficiency and an overall compact system. The high voltage switch (2) is a nitrogen-filled spark gap, which is pressurized to 16 atmospheres. By adjusting the pressure the spark gap voltage can be varied from 350 to 700 kV. The oil-filled adiabatic transmission line (3) matches the 22 Ω impedance of the pulse forming line to the $\approx 100 \Omega$ impedance of the vacuum diode. The magnetically insulated coaxial diode uses an explosive-emission graphite cathode (2 cm diameter with a 1 mm annular wall thickness). A uniform magnetic field up to 3.0 T in magnitude, used to confine the electron beam, is generated by a pulsed solenoid system (4). The pulsed system provides a magnetic field pulse duration of 3 ms and requires 10 s to recharge. The Sinus-6 can generate electron beams at a pulse repetition rate of 200 Hz, but is presently operating at 0.1 Hz due to constraints imposed by the magnetic field system.

The Anode-Cathode (A - K) gap spacing and applied magnetic field were held constant and the resultant diode impedance was about 125 Ω , depending on the cathode potential. The electron beam pulse has a full width, half maximum (FWHM)

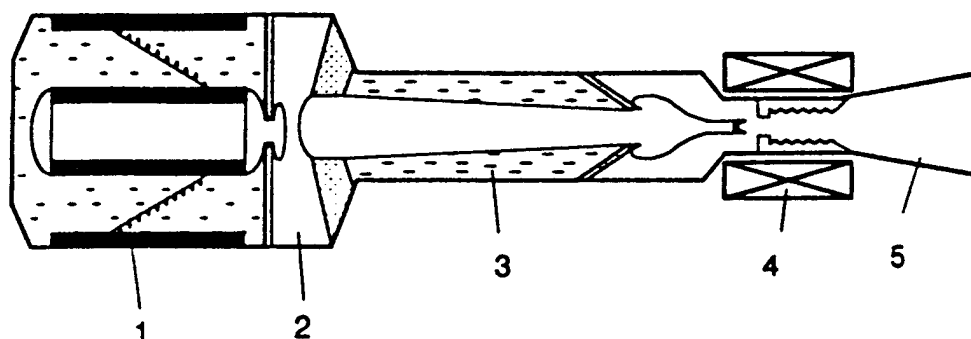


FIG. 1. Diagram of the Sinus-6 accelerator (the various components are described in the text).

temporal duration of about 12 ns. Cathode voltages are measured using a capacitive divider and beam currents are measured using a Rogowski coil. By adjusting the pressure in the spark gap, cathode voltages from 400 to 650 kV are generated with corresponding beam currents ranging from 3 to 5 kA.

Total peak radiated power measurements were made using both a semiconductor microwave detector and a crystal diode detector. (Additional information on the measurement techniques can be found in Ref. 6). Power density measurements were made 1.6 m downstream from a conical horn antenna which has a maximum diameter of 15 cm. The total power was calculated by numerically integrating the radiation pattern that was experimentally mapped. The radiated frequency was measured by heterodyning the RF signal against a known oscillator frequency.

The basic tube studied in this work is a nonuniform amplitude configuration referred to as the "Long Tube". This tube is a two stage slow wave structure constructed from individual rings for each ripple period, and was designed based on the work of Kovalev and colleagues.³ Each ring is a trapezoidally shaped annulus with a width (ripple period) of 1.5 cm and a maximum radius of 1.65 cm. Four different rings were used, and their parameters are listed in Table I(A).

In addition to this basic tube, variations referred to as Short Tubes #1-#3 were also studied to elucidate the role of the initial stage of the Long Tube. As is evident from Table I(B), the short tubes are variations of the second stage of the Long Tube. These short tubes have a start current in the range of the start current for the Long Tube.

A typical mode pattern radiated by the Long Tube and measured 1.6 m from the output antenna is shown in Fig. 2(a). The beam parameters used were 500 kV and 4 kA, and each data point was the average of 3 to 5 shots. The calculated TM_{01} radiation pattern for a total peak power of 500 MW is indicated by the solid line in Fig. 2(a). For comparison, the data points were integrated numerically to yield a total power of 450 MW, in good agreement with the calculated mode pattern. Since the radiation pattern was found to be insensitive to slight changes in frequency, it was sufficient to measure the power density at the maximum electric field in order to ascertain the total radiated power. Figure 2(b) presents a measured mode pattern

TABLE I(A). Parameters of slow wave structure rings; **(B).** summary of tube configurations; **(C).** summary of Long Tube results.

(A)

Ring Type	Maximum Radius [cm]	Minimum Radius [cm]	Average Radius [cm]	Ripple Amplitude [cm]	Ripple Period [cm]
A	1.65	1.45	1.550	0.100	1.50
B	1.65	1.38	1.515	0.135	1.50
C	1.65	1.20	1.425	0.225	1.50
D	1.65	1.15	1.400	0.250	1.50

(B)

	Tube Configuration	Relative Power	Crystal Diode Detector Pulse Width [ns]	Frequency ± 0.05 [GHz]
Long Tube	A-A-B-B-C-C-C-D-D-C	1.0	8.7	9.45
Short Tube #1	C-C-C-D-D-C	0.2	7.2	9.60
Short Tube #2	C-C-C-C-D-D-C	0.7	7.7	9.50
Short Tube #3	C-C-C-C-C-D-D-C	0.5	10.0	9.60

(C)

Cathode Voltage [kV]	Beam Current [kA]	Input Power [GW]	Total Peak Power [MW]	RF Conversion Efficiency	Diode Impedance [ohms]
475	3.49	1.66	371	0.22	136
508	3.83	1.95	420	0.22	133
533	4.06	2.16	453	0.21	131
566	4.39	2.48	487	0.20	129
576	4.52	2.60	494	0.19	128
601	4.86	2.92	519	0.18	124
627	5.19	3.26	545	0.17	121

when a mode convertor⁷ is placed between the slow wave structure and conical horn antenna. This mode convertor was constructed based on the design of Denisov and colleagues at the Institute of Applied Physics (Nizhny Novgorod, Russia).⁷

Figure 3 shows the dependence of peak radiated power using the Long Tube on electron beam current. Each data point represents the average of 5 shots and the error bar displays the typical scatter in the data. The beam current was changed by varying the pressure in the spark gap switch and the applied voltage to the cathode. The $A - K$ gap and applied magnetic field were held constant for all shots. The results from Long Tube over a range of parameters are summarized in Table I(C).

At beam currents above 4 kA air breakdown near the output window was observed. Time-integrated photographs showed a bright annular ring of plasma consistent with a TM_{01} radiation mode pattern. In order to suppress the air breakdown, a gas bag filled with SF_6 was placed in front of the horn antenna. The amplitude and pulse duration from the crystal diode detector were observed to increase when the gas bag was used. Figure 3 shows the effect of using a gas bag on the microwave power measurements.

To elucidate the role of the prebuncher on the efficiency of the Long Tube, experiments were performed with various short tubes (parameters summarized in Tables I(A) and (B)). Sections of cutoff pipe were added to the modified tubes to ensure that the $A - K$ gap and the tapered magnetic field at the end of the tube remained constant. The beam parameters were approximately 4 kA and 500 kV, which were chosen to avoid air breakdown associated with the Long Tube. Data showing the peak output microwave power generated by the Long Tube and the three short tubes are given in Table I(B). It is clear that none of the short tubes are as efficient as the Long Tube, and Short Tube #2 is the most efficient, with an efficiency of about 15%. Consistent with the lower relative powers indicated, air breakdown was never observed with the short tubes, even when they were driven at the highest input beam powers. Because the growth rate of the RF fields must decrease with the difference between the beam current and the start current, it can be inferred from the RF pulse widths in Table I(B) that the start current for the Long Tube is between the start currents for Short Tubes #2 and #3. Therefore, the increased efficiency of the Long Tube is a result of the prebuncher and cannot be attributed to the ratio of beam current to start current.

Particle-in-cell (PIC) simulations using TWOQUICK^{6,8} provided a comprehensive picture of the prebunching of the electron beam in the initial section of the nonuniform amplitude slow wave structure. The results from the PIC simulations indicate that, in addition to the surface harmonic of the backward wave, the forward traveling volume harmonics may play an important role in the energy exchange process in the BWO. Based on these results it may be possible to design an uniform BWO where the forward traveling volume harmonics can serve the role of a prebuncher.⁶

LONG PULSE EXPERIMENTS

The accelerator used in the long pulse BWO experiment is a modified Physics International Pulserad 110A. An 11-stage Marx bank with an energy storage capacity

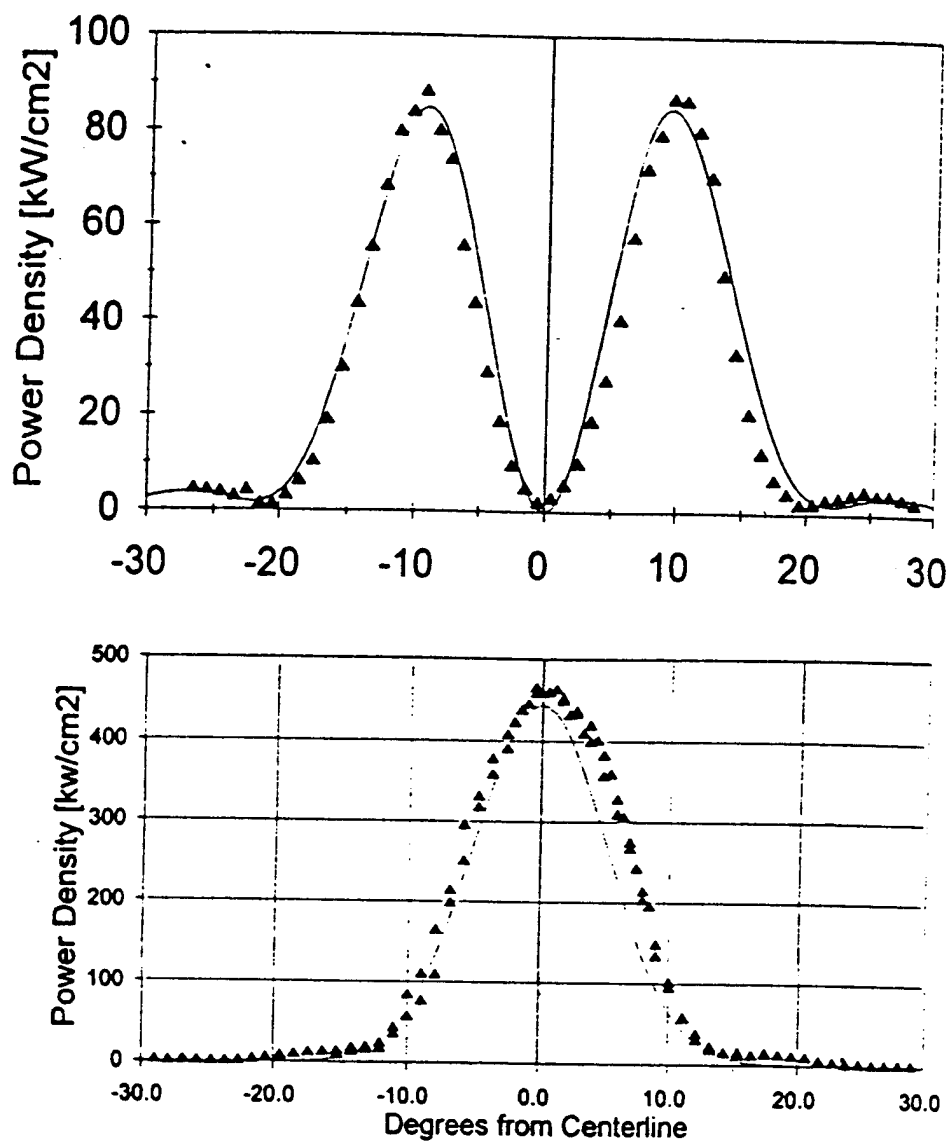


FIG. 2. (a) Measured and calculated TM_{01} mode pattern; (b) measured and calculated TE_{11} mode pattern.

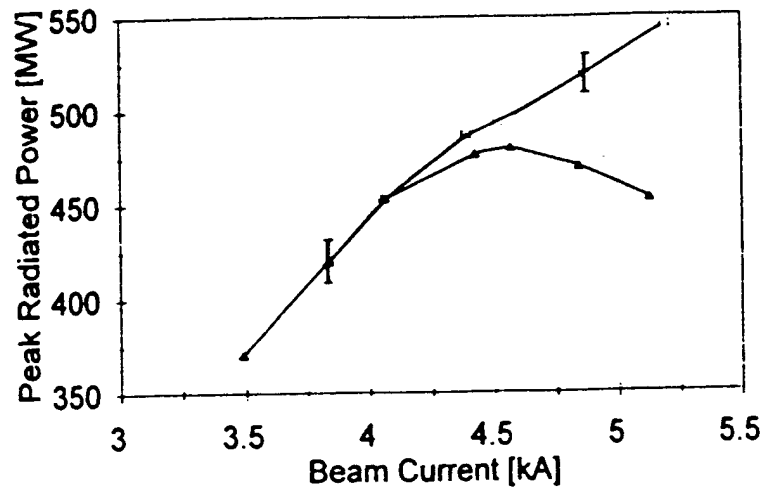


FIG. 3. Dependence of power radiated by Long Tube on electron beam current.

of 2.75 kJ is used as the main energy store and initial pulse forming device in the accelerator. The Blumlein which previously followed the Marx bank has been replaced with an LC filter network. When erected, the Marx bank and the LC network together form a 2-stage pulse forming network (PFN) (see Ref. 9 for additional information on this accelerator). The pulse duration and impedance of the accelerator in this configuration are approximately 450 ns and 40 Ω , respectively, although the diode load is presently being modified to increase the impedance. The electron gun immediately follows the LC filter network and its configuration is nearly identical to the one on the Sinus-6. The cathode holder is stainless steel and is curved to follow the magnetic field lines. At the end of the holder is a 2 cm-diameter carbon knife-edge tip from which an annular electron beam is emitted. Either 6 or 7 field coils can be placed around the slow wave structure to produce a guiding field for the electron beam. The magnetic field strength on axis is typically 3.0 T. After traveling through the slow wave structure, the electron beam follows the magnetic field lines to the beam dump, which consists of a section of stainless steel screen surrounded by a larger, concentric section of copper pipe that is lined with carbon on its inner surface. The microwaves that are produced in the slow wave structure travel past the screen into another section of circular waveguide, and then to a conical horn where they are radiated into an *anechoic* measurement area. Microwave radiation is measured using a simple \vec{B} probe which directly measures the wave magnetic field intensity.

Long pulse vacuum BWO experiments have begun using uniform slow wave structures. Initial results from these experiments yielded microwave pulses with FWHM durations on the order of 100 ns. Typical signals from a Rogowski coil measuring the beam current and the microwave detector (\vec{B} probe) can be found in Ref. 1. The radiated power is estimated to be only about 10 MW, although it should be noted that there was evidence of breakdown inside the slow wave structures on these shots. By positioning the \vec{B} probe at various angles with respect to the center axis of the horn, a crude map of the radiation was obtained and indicated that the

radiation is emitted in the TM_{01} mode. Frequency measurements have not been performed at this time. However, several PIC code simulations of the slow wave structure were performed and the results indicated a frequency of approximately 10 GHz. It is believed that improvement in the breakdown characteristics of the slow wave structures can yield improved long pulse performance.

ACKNOWLEDGMENTS

The work at the University of New Mexico is supported by U.S. Air Force Office of Scientific Research Grant F49620-94-1-0087DEF and Air Force Office of Scientific Research Instrumentation Grant F49620-93-1-0585. The work at Sandia National Laboratories is supported by DOE and the Air Force Phillips Laboratory. Much of this work has been in collaboration with our colleagues at the High Current Electronics Institute (Tomsk, Russia), notably Drs. Korovin, Rostov, Polevin, Roitman, and Pegel.

REFERENCES

1. Portions of this paper were presented earlier at the *AGARD-SPP/DRG Joint Symposium on High Power Microwaves (May 2-5, 1994, Ottawa, Canada)* (conference proceedings in press).
2. J. Benford and J. Swegle, *High-Power Microwaves* (Artech House, Boston, MA, 1992), Chap. 6 and references therein.
3. N.F. Kovalev and V.I. Petrukhina, "Ultra-relativistic Carcinotron with a Jump in Beam-rf Coupling," *Electr. Techn. SVCH* 7, 101 (1977) (in Russian), and references therein.
4. S.D. Korovin, S.D. Polevin, A.M. Roitman, and V.V. Rostov, "Relativistic Backward Wave Tube with Variable Phase Velocity," *Sov. Tech. Phys. Lett.* 18, 265 (1992).
5. For an overview of plasma-filled devices, see Y. Carmel, W.R. Lou, T.M. Antonsen, Jr., J. Rodgers, B. Levush, W.W. Destler, and V.L. Granatstein, "Relativistic Plasma Microwave Electronics: Studies of High-Power Plasma-Filled Backward-Wave Oscillators," *Phys. Fluids B* 4, 2286 (1992).
6. L.D. Moreland, E. Schamiloglu, R.W. Lemke, S.D. Korovin, V.V. Rostov, A.M. Roitman, K.J. Hendricks, and T.A. Spencer, "Efficiency Enhancement of High Power Vacuum BWOs using Nonuniform Slow Wave Structures," to appear in *IEEE Trans. Plasma Sci.* (Special Issue on High Power Microwaves, 1994).
7. D.V. Vinogradov and G.G. Denisov, *Radiofizika* 33, 726 (1990); G.G. Denisov (private communication, 1992).
8. D.B. Seidel and T.D. Pointon, (Sandia National Laboratories, private communication).
9. C. Grabowski, J. Gahl, E. Schamiloglu, and D. Shiffler, "Long-Pulse High Power Microwave Experiments," to appear in *Proc. of the 9th IEEE International Pulsed Power Conf.*

Appendix D: Paper in Print Pertaining to Long Pulse BWO

LONG-PULSE HIGH POWER MICROWAVE EXPERIMENTS

C. Grabowski, J. Gahl, E. Schamiloglu, and D. Shiffler
 Department of Electrical and Computer Engineering
 University of New Mexico
 Albuquerque, NM 87131

Abstract--Experiments to develop a long-pulse, high power microwave source are currently being conducted at the University of New Mexico (UNM). By removing the Blumlein in a PI Pulserad 110A and replacing it with a parallel L-C network, the Pulserad has been converted into a type A PFN.[1] The new pulse length, output voltage, and impedance of the device are approximately 450 ns, 500 kV, and 40 Ω , respectively. This modified Pulserad is used to drive an electron beam diode which is identical to the diode in the UNM SINUS-6 accelerator.[2] The relativistic electron beam produced by the diode is injected into a slow-wave structure to generate X-band microwaves at a frequency similar to that of the UNM SINUS-6. In addition, the output voltage and current are also similar for the two accelerators; however, the UNM SINUS-6 is a short-pulse, rep-rated accelerator while the UNM Pulserad is a long-pulse, single-shot machine. The primary objective of these experiments is to determine whether the backward wave oscillator (BWO) presently on the SINUS-6 machine can operate at long pulse durations. Initial experiments involve vacuum BWO operation, which will be followed by plasma-filled BWO operation. The system design will be presented along with electron beam diagnostic and microwave generation results.**

I. Introduction

In the past several years interest in high power microwaves has grown considerably. Devices have been developed which have peak powers on the order of terawatts. Increasing the average powers of these devices, though, has proved to be more difficult. In the case of long-pulse backward wave oscillators (BWO's) microwave generation simply ceases after a period of time even though the electron beam continues to travel through the slow wave structure.

At the University of New Mexico a long-pulse accelerator has been developed to drive a BWO for the purpose of investigating this phenomenon further. The electron gun of the BWO is nearly identical to that of the UNM SINUS-6, a short-pulse, rep-rated accelerator also at the university. Experiments are being conducted which involve both vacuum and plasma-filled BWO operation, and a portion of this study will be focused on understanding the behavior of the plasma and the interactions between the electron beam and the plasma in plasma-filled BWO operation.

This paper will discuss the work that has been completed thus far. In section II a description of the accelerator and the BWO will be presented, followed by a discussion of some of the preliminary results in section III.

**Research supported by AFOSR grant #F49620-92-J-0157DEF.

Section IV will present the conclusions drawn from this work and list the plans for future work. Acknowledgments are made in section V.

II. Experimental Design

The accelerator for the experiment has been constructed using a Physics International Pulserad 110A. Inside the Pulserad 110A is an 11-stage Marx bank, which has a capacitance of 0.05 μ F and a maximum charging voltage of 100 kV for each stage. This translates to a maximum energy storage capacity of 2.75 kJ. The blumlein following the Marx bank was removed and replaced with a parallel L-C network. Both the Marx bank (when erected) and the L-C network together form a type-A PFN which has a pulse width and impedance of approximately 450 ns and 40 Ω , respectively. An equivalent circuit is shown in Fig. 1. A balanced resistive voltage divider, which is not

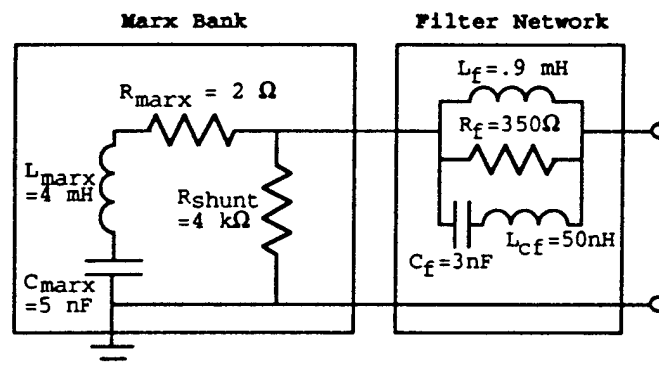


Fig. 1 Equivalent circuit of Pulserad 110A.

shown in Fig. 1, has been placed between the Marx bank and the filter network to monitor the Marx voltage. PSPICE calculations show that with a matched load a peak voltage of 775 kV can be obtained from the Marx bank after it has been erected, resulting in a cathode voltage and load current of 570 kV and 14.3 kA, respectively (Fig. 2).

As was mentioned previously, the electron gun used with the Pulserad 110A is nearly identical to that on the UNM SINUS-6. The major difference between the two is that the slow wave structure in the gun on the Pulserad 110A is slightly different. Figure 3 shows a diagram of the gun. The cathode is stainless steel and has a 1.95 cm diameter knife-edge tip to emit an annular beam into the slow wave structure. As can be seen from the drawing the cathode is inserted some distance into the magnetic field so that electrons are emitted on uniform field lines. The maximum field that can be produced on axis by the field coils is approximately 3 T. Two Rogowski coils are shown in the diagram which are used to measure the beam current, one around the

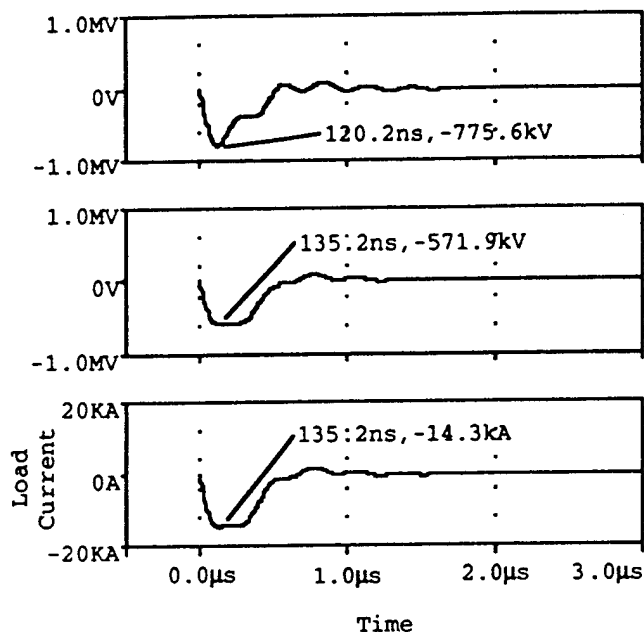


Fig. 2 Voltage and current waveforms calculated by PSPICE for the Pulserad 110A fully charged and terminated into a 40Ω load.

cathode, which is currently installed, and one at the end of the slow wave structure, which will be installed in the near future. The coil used is a standard non-integrating Rogowski coil, requiring an RC integrator at the input of the oscilloscope to process the signal. Finally, following the slow wave structure is a conical horn which radiates the microwave power.

III. Discussion of Preliminary Results

Cathode Voltage and Beam Current

During experiments in which the Marx bank was charged to full voltage the signal waveform from the voltage divider indicated a peak voltage from 520 to 620 kV, which is slightly less than the PSPICE prediction of 775 kV for the 40Ω load. Assuming that the ratio of the cathode voltage to the Marx voltage remained the same as that which PSPICE predicted, the cathode voltage was then in the range of 380 to 450 kV.

A beam current of 3.8 to 4.2 kA was consistently observed with the Rogowski coil. Pulse widths (measured at the base of the current pulse) varied from 530 to 560 ns. These values are in very good agreement with the pulse widths predicted by PSPICE in Fig. 2.

Mode Pattern

Two diagnostic methods were used to determine the mode pattern of the microwave radiation. The first and simplest method was to place a sheet of foam with a matrix of small neon bulbs embedded in it in the far-field region in front of the output horn. The room was darkened and an open-shutter camera was then used to take photographs of the light board as the Pulserad was fired. Figure 4 shows one of the photographs that were taken. In this particular case the Pulserad 110A was fired 7 times before closing the camera shutter. A small dark region can clearly be seen in the center of the light board surrounded by a rather broad lighted region which is in turn surrounded by another dark region. This pattern is characteristic of the TM_{01} radiation mode.

A second diagnostic used to evaluate the mode pattern was a B-dot probe. The probe was mounted on a wooden stand and positioned on

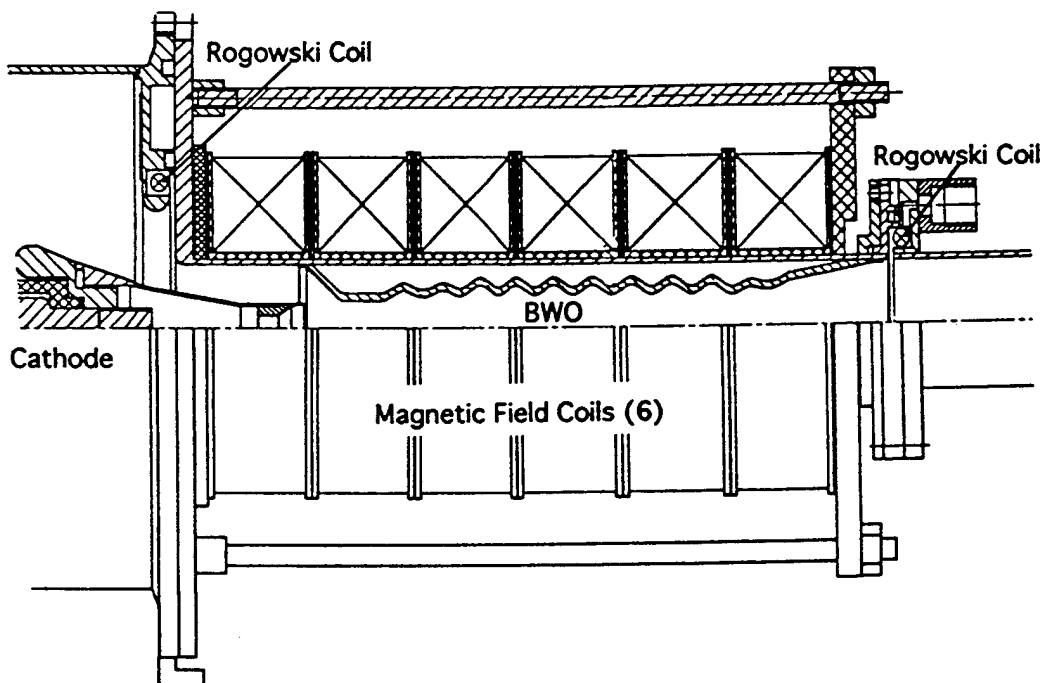


Fig. 3 Cross-sectional diagram of electron gun.

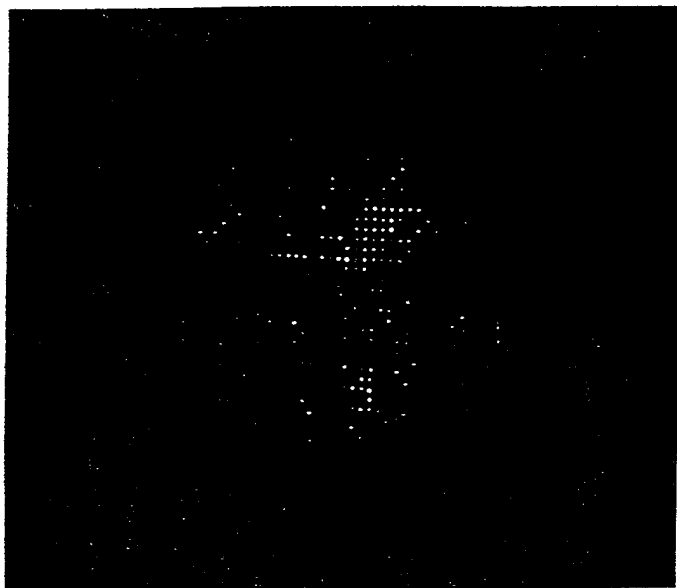


Fig. 4 Photograph of light board showing pattern for TM_{01} mode illuminated.

the axis of the microwave horn at the same distance at which the light board was set. Measurements were taken and then the probe was moved to the left or right in increments of 5 degrees away from the horn axis. One of the recorded signal waveforms from the B-dot probe is shown in Fig. 5 along with the current waveform for the same shot. The early cessation in the production of microwaves, which was mentioned earlier as a characteristic of BWO's, is clearly seen here; the current pulse has a duration of 540 ns, while the duration of the microwave pulse is only 130 ns, over 4 times shorter.

Because of the large amplitude of the microwave signal from this shot and other similar shots, several layers of attenuating material were placed in front of the output horn, since the crystal detector used with the probe behaves very non-linearly for large input signals. As shown in the plot of probe data in Fig. 6, the signals from the B-dot

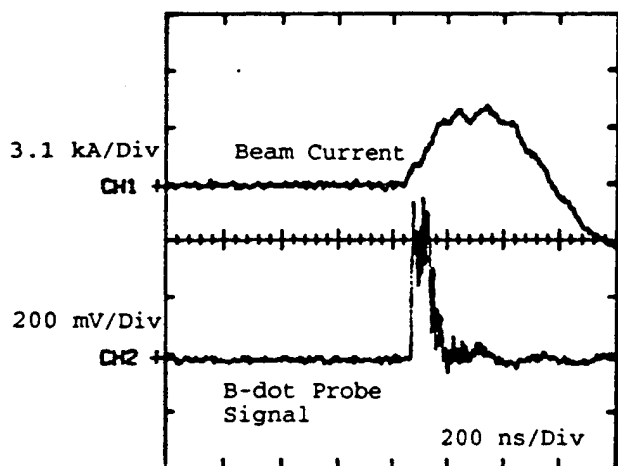


Fig. 5 Typical signal waveforms from the Rogowski coil and B-dot probe.

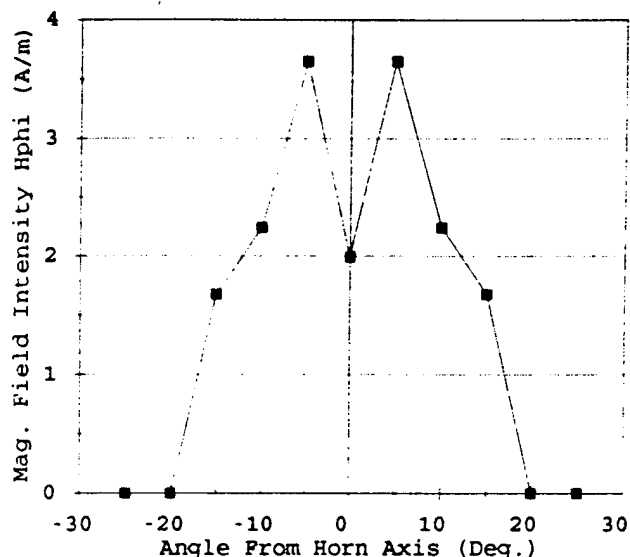


Fig. 6 Radiated magnetic fields measured by B-dot probe at 1.7 m from horn aperture. Data for positive angles was mirrored to negative angles to better illustrate radiation pattern.

probe were generally in agreement with the photograph in Fig. 4 and indicate the presence of the TM_{01} mode. The perturbation in the recorded data in comparison to the ideal TM_{01} pattern may have been caused by scattering of the microwaves as they passed through the attenuating material or the decreased radiation intensity bringing the probe signal closer to the noise floor.

Microwave Power and Frequency

Although the radiated power could not be calculated exactly from the experimental data, it was estimated to be less than 10 MW. Another estimate of the power was obtained using MAGIC, a 2 1/2 D particle-in-cell simulation code.[3] Figure 7 shows a plot from MAGIC of the power over a 10 ns time period calculated for the case with a cathode voltage of 350 kV and a beam current of 4 kA. The power rises to almost 80 MW after about 1.5 ns but then rapidly drops. Over a duration of 130 ns the average power would seem to be on the order of 10 MW, which agrees well with the estimate from the experimental data. By setting the oscilloscope on a faster time scale when recording the B-dot probe signals (say, 5 ns/div instead of the 200 ns/div used for most of the present measurements) the high initial powers could be confirmed.

For this cathode voltage and beam current MAGIC calculates a value of approximately 7 GHz for the dominant microwave component. However, other MAGIC runs for other cathode voltages and beam currents show the dominant frequency component to be 10 GHz. Using a Mathematica routine written by Tom Spencer at Phillips Lab for calculating the cold dispersion relation of a slow wave structure [4], a frequency of 10.8 GHz was predicted for the microwave radiation.

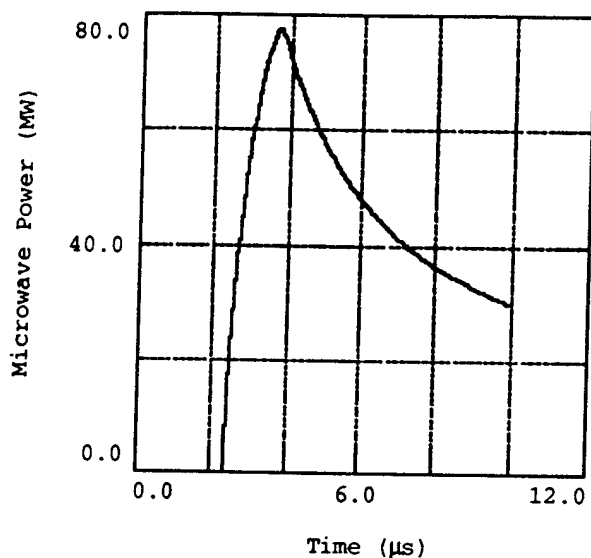


Fig. 7 Time history of radiated microwave power calculated by MAGIC for a beam current of 4 kA and a cathode voltage of 350 kV.

IV. Conclusions

Initial experiments show the radiated microwave power to be rather low; however, MAGIC predicts this low power level for the parameter space in which these experiments have been conducted. It should also be pointed out that the UNM SINUS-6 achieves considerably higher powers (~ 600 MW) [2] due to the fact that a more advanced slow wave structure has been installed in it. Once the theory behind the operation of this slow wave structure is better understood a structure of this design will then be placed on the Pulserad 110A. However, the immediate next steps in this investigation will involve varying the parameter space in MAGIC in order to determine a more favorable operating regime in which higher powers can be produced. Diagnostics will also be improved to better determine the radiated power and mode pattern. Work on plasma-filled BWO experiments will then begin, and the necessary diagnostics for these experiments will be developed and incorporated into the Pulserad 110A.

V. Acknowledgments

The authors wish to thank M. Anderson, J. Bradley, T. Cavasos, J. Crawford, L. Moreland, and R. Terry for their technical advice and assistance in assembling the experimental apparatus. The authors also wish to acknowledge the work of N. Keator with much of the early MAGIC simulations.

References

- [1] D. B. Cummings, "Conversion of a Marx Generator to a Type-A Pulse Forming Network," IEEE Conference Record of the Twelfth Modulator Symposium, IEEE Cat. No. 76CH1045-4ED, 1976, pp. 142-6.
- [2] L. Moreland, et al., this conference.
- [3] B. Goplen, R. E. Clark, J. McDonald, and W. M. Bollen, Users' Manual for MAGIC/Version-Oct. 1991, MRC/WDC-R-246, (Mission Research Corp., Washington, D.C., 1991).
- [4] T. Spencer (private communication, 1992).

Appendix E: Papers in Print Pertaining to Ferroelectric Cathodes

INITIAL STUDIES OF FERROELECTRIC CATHODES

T. Cavazos, D. Shiffler, B. Wroblewski, C. Fleddermann,
J. Gahl, and E. Schamiloglu
Electrical and Computer Engineering Department
University of New Mexico
Albuquerque, NM 87131

Abstract--A basic limitation of all electron beam driven radiation producing devices is the need for more input power. For high power microwave devices and free electron lasers, this requirement may be stated as the need for greater electron beam current with higher brightness beams. Our research investigates ferroelectrics as a source of electrons for high current cathodes. Ferroelectric cathodes operate by inducing a phase transition in a sample of ferroelectric material, leaving copious amounts of electron space charge on the surface which can be easily liberated.[1] We have built a prototype electron gun in a triode configuration. The gun is energized using a transmission line pulser. The grid of the triode induces the phase transition. A second voltage is applied across the anode-cathode gap to accelerate the electrons. In this paper, we present results of polarization measurements under AC signals, as well as results of operating the triode as an electron gun. Finally, a design is presented for a beam transport system using standard accelerator technology to determine the beam emittance and brightness. Since ferroelectric cathodes can in principle operate at relatively low temperatures, the limiting emittance set by the cathode temperature should be very low."

1-Introduction

Electron emission for vacuum electronics has been limited to thermionic sources (i.e. oxide coated or barium dispenser cathodes), explosive field emission cathodes (carbon felt materials) and exotic photocathodes. A novel cathode material has been introduced consisting of ferroelectric materials. By inducing a phase transition in a pre-poled ferroelectric, abundant electron emission can be observed. Emitted charge densities of up to $1 \mu\text{C}/\text{cm}^2$ [2] as well as current densities up to $70 \text{ A}/\text{cm}^2$ have been documented.[3] These results demonstrate diode currents exceeding the space charge limit for typical vacuum diodes.

A research program is in progress at the University of New Mexico (UNM) to investigate ferroelectric cathodes as a novel emitter for high power microwave (HPM) sources. Such sources require high brightness, low emittance electron beams. Ferroelectric cathodes offer two key advantages over state-of-the-art thermionic emitters: (1) higher current densities and (2) lower operating temperatures. Since the ferroelectric is not operated as an explosive emitter, it is not susceptible to gap closure due to plasma formation. The material has demonstrated repetitive operation and can be used in any environment (rough to hard vacuum, and plasma filled devices).[4]

*This research is funded by AFOSR Grant #F49620-92-0157DEF.

A key aspect of this research program is to investigate thin film ferroelectric cathodes. These films are fabricated in the UNM Center for High Technology Materials (CHTM). The materials can vary in thickness from $0.1 \mu\text{m}$ to $10 \mu\text{m}$ and can be produced in a variety of compounds and mixtures. Thin films have several advantages over bulk material: the ferroelectric can be switched at lower voltages since the material is thinner, the films may be grown or sputtered onto a wide variety of cathode geometries, and lastly, it may be possible to reduce the resultant electron beam divergence after emission.[5]

This paper summarizes the effort to date beginning with a brief discussion of the theory of ferroelectric emission in sec. 2. Section 3 describes the method of measuring the polarization (P-E) characteristics of the material. A discussion of the fabrication of the thin films is given in sec. 4 and a description of the triode experiments is given in sec. 5. The design and simulation of a low emittance gun is presented in sec. 6 followed by concluding remarks.

2-Theory of Ferroelectronics

Ferroelectric materials are polar dielectrics that undergo a change of spontaneous polarization under the influence of an applied electric field. Like ferromagnetic materials, ferroelectrics have domains, exhibit hysteresis loops, and show Curie-Weiss behavior near the phase transition temperatures.[6] The displacement in a polar material is expressed as:

$$\mathbf{D} = \epsilon_0 \mathbf{E} + \mathbf{P}, \quad (1)$$

where the polarization may be expanded as:

$$\mathbf{P} = \epsilon_0 \chi_e \mathbf{E} + \mathbf{P}_s + \mathbf{P}_d. \quad (2)$$

The first term is the polarizability of the material, the second term \mathbf{P}_s describes the polarization due to the spontaneous alignment of the domains, and the last term is the polarization due to defects in the material [4]. For a given remanent polarization in the material, there will be a bound surface charge density which is expressed as:

$$q_{sb} = |\mathbf{P}|_{\text{surface}} \quad [\text{C}/\text{m}^2]. \quad (3)$$

Under normal conditions, the bound surface charge is screened by free charges. If the material undergoes a rapid change in polarization, then a large uncompensated charge will be generated at the surface. The electric field is high enough ($100\text{--}10,000 \text{ kV}/\text{cm}$) to extract carriers bound in the surface of the material. If conditions are arranged such that these carriers are negative, then the electrons will be accelerated into the diode gap.

The various methods of inducing a rapid change in the polarization include [4]:

- (1) heating or cooling across a phase transition boundary from or to the ferroelectric (FE) state,
- (2) transitions between the FE phase and the antiferroelectric (AFE) or paraelectric (PE) phases by applying pulsed stress,
- (3) transitions between the AFE or PE phases and the FE phase by applying a pulsed electric field,
- (4) partial reversal of P_r inside the ferroelectric phase by applying high voltage pulses, and
- (5) illumination by laser light (photo assisted domain switching).

It is most advantageous to apply method (4) for repetition rate applications. This technique was initially selected for this research program. A second option is to heat the material close to the phase transition, then apply a pulsed electric field to switch the material into the PE or AFE phase. With this combination of methods (1) and (3) no cooling of the material between pulses is necessary so that it is consistent with rep-rate operation. A further enhancement of emission can possibly be obtained by adding laser light illumination.

3-Polarization Curves

The hysteresis of a ferroelectric material is determined by plotting the polarization of the material as a function of the applied electric field. One method of performing this method is the Sawyer-Tower loop circuit (Fig. 1). [6] Capacitor C_t must be linear and should have a capacity much higher than the material under test. The vertical and horizontal voltages are written as:

$$V_x = Ed \text{ and}$$

$$V_y = \frac{1}{C_t} \int_0^t i(t) dt, \quad (4)$$

where d is the thickness of the material. Assuming that the loop current is a uniform displacement current, the vertical voltage may be rewritten as:

$$V_y = \frac{1}{C_t} \int_0^t \frac{dD}{dt} A dt = \frac{DA}{C_t}, \quad (5)$$

where A is the conduction area. Substituting Eq. (1) for the displacement gives

$$V_y = \frac{A}{C_t} (\epsilon_0 E + P). \quad (6)$$

Finally, substituting V_x/d for E and solving for P gives

$$P = V_y \frac{C_t}{A} - V_x \frac{\epsilon_0}{d}. \quad (7)$$

As long as C_t is large, the second term in Eq. (7) can be ignored and the vertical and horizontal voltages can be related to the polarization and electric field using

$$P = V_y \frac{C_t}{A} \text{ and } E = \frac{V_x}{d}. \quad (8)$$

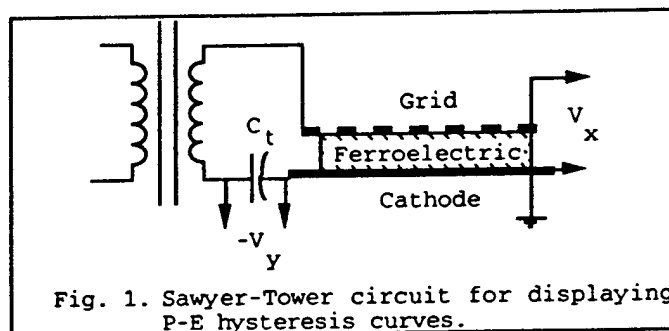


Fig. 1. Sawyer-Tower circuit for displaying P-E hysteresis curves.

The hysteresis curves are obtained with the materials mounted in the triode experiment. This step is to insure that there is good electrical contact with the material being tested. From the hysteresis curves, the remanent polarization P_r is determined from the vertical intercept, and the coercive field E_c is determined from the horizontal intercept. Hysteresis curves will be collected at temperatures up to the Curie temperature. Tests on a 0.25 mm PLZT wafer yielded the P-E curve shown in Fig. 2. This result most likely indicates a minor hysteresis loop. Attempts to increase the coercive field and drive the material into hard saturation resulted in electrical breakdown.

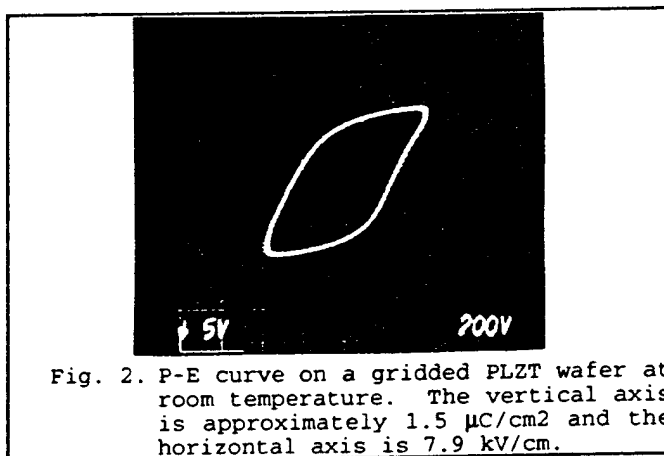


Fig. 2. P-E curve on a gridded PLZT wafer at room temperature. The vertical axis is approximately $1.5 \mu\text{C}/\text{cm}^2$ and the horizontal axis is $7.9 \text{ kV}/\text{cm}$.

4-Manufacturing Thin Films

The ferroelectric films are produced with an ion beam sputtering method (Fig. 3). The beam source is a Kaufman Ion Gun which provides independent control of beam energy and current. The ion gun is capable of

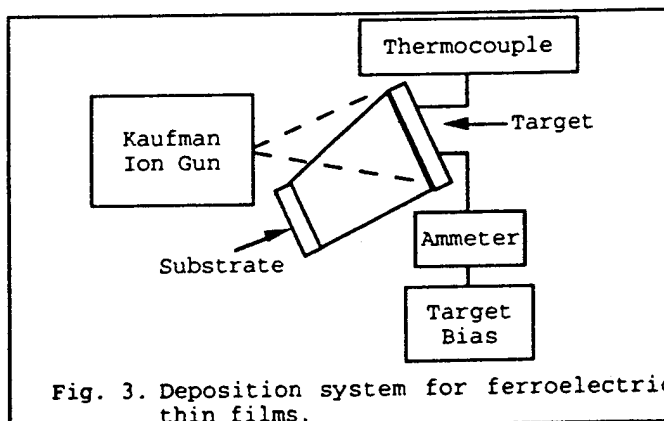


Fig. 3. Deposition system for ferroelectric thin films.

sputtering with an inert ion (Ar) beam or a reactive ion (O₂) beam. The sputtering target is a single composite (28/0/100) PLZT. The films are deposited onto a flat stainless steel substrate which has been coated with platinum. After deposition, the films are annealed in an oxygen furnace for half an hour at 650°C.

The CHTM laboratory also deposits gold electrodes onto the ferroelectric samples. The metallization is deposited using electron beam evaporation. The grid is patterned with standard photolithography/wet etch techniques. The electrode pattern is circular with 200 μ m apertures and a 200 μ m separation.

5-Triode Experiments

The purpose of the triode experiments is to determine the emission current density and charge limit of several different ferroelectric compounds. These results will determine the emittance of the cathode. A key aspect of this part of the research is to compare the performance of the thin film ferroelectric materials to the bulk materials. A parallel plane triode tube (Fig. 4) has been constructed for this task. The triode is a demountable vacuum tube assembled with 7 cm stainless steel flanges. An ion pump is used to evacuate the tube to 10^{-9} Torr. The grid flange is isolated from the cathode with a ceramic adapter and the anode is separated with a 25 cm glass tube. A tungsten filament heater is suspended inside a 1.9 cm stainless steel tube which is connected to cathode potential. The material under test is attached to a cap on top of the heater tube. Grid connections are made from the top of the sample to four stainless steel posts which are connected to the grid flange.

The experiment is operated as a grid modulated hard tube pulser. The anode potential can be varied from 10-30 kV and the grid is energized with a transmission line pulser. The ferroelectric material is pre-poled with the polarizing vector pointing into the triode. Pre-poling is accomplished by heating the material above the Curie temperature and cooling down through the transition with a DC field across the material.

Electrical contacts to the bulk samples have been problematic. Connections are sensitive to mechanical stress due to the brittle nature of 0.25 mm ceramic wafers. The gold metallization adhered poorly to the ceramic. The grid pulled away from the sample when wires were bonded to the metallization. A conductive epoxy was used to glue foil contacts to the grid. However, the adhesive was too fragile for the mechanical stresses during the triode assembly. Planned improvements include roughening the surface of the ceramic to increase the surface tension with the gold metallization, and annealing the metallization at 200 °C after deposition. The mechanical mounting of the wafers has been redesigned to minimize the stress on the ceramic.

Initial tests on thin films were inconclusive. The grid contacts were shorted to the cathode in several cases. This problem could be caused by: 1) the film becoming

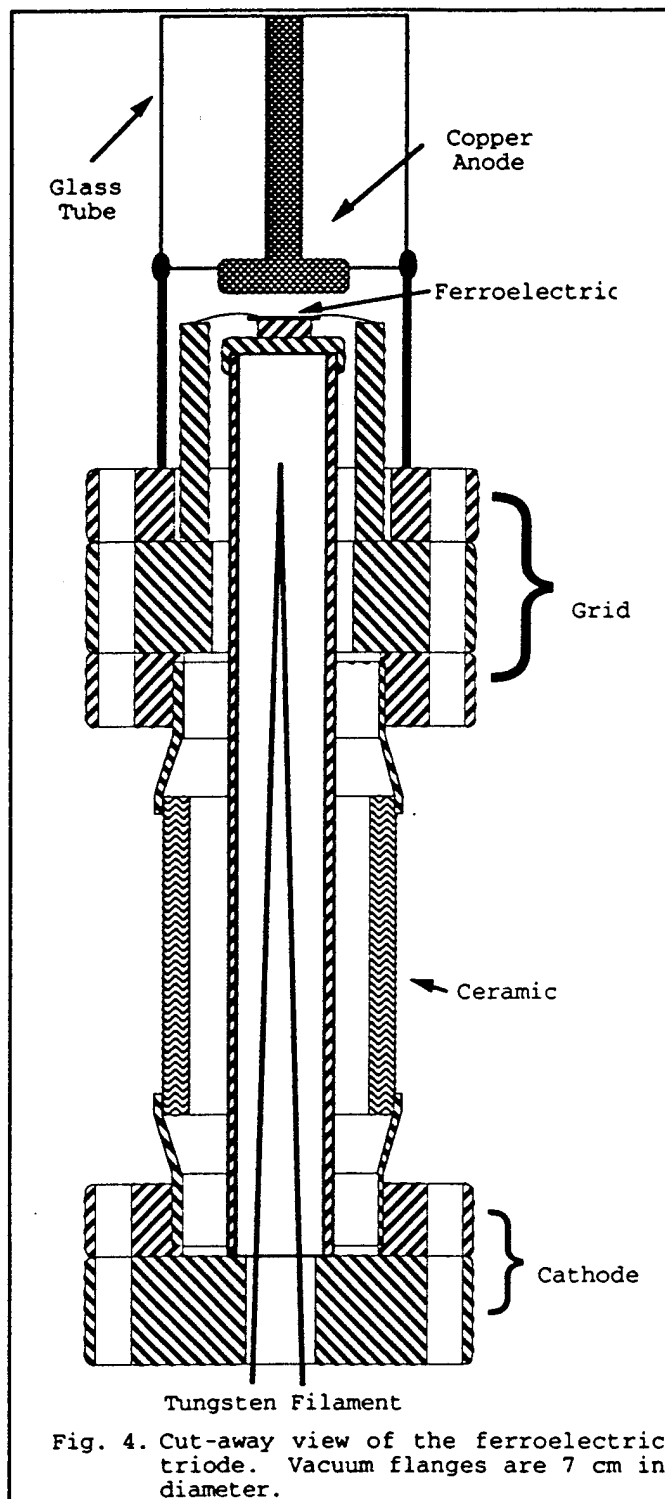


Fig. 4. Cut-away view of the ferroelectric triode. Vacuum flanges are 7 cm in diameter.

scratched during assembly or 2) breakdown of the film due to static discharge during handling.

6-Ferroelectric Gun Design

The electron gun design is based on a Pierce gun configuration for low emittance operation. The design was analyzed using EGUN and the gun parameters for a 10 kV anode voltage are given in Table 1. A schematic of the ferroelectric gun is given in Fig. 5. The grid will be connected to the focusing

electrode which must be held at ground potential. The ferroelectric will be energized with a negative cathode pulse.

Table 1. Electrical Parameters of the Ferroelectric Pierce Gun

Current Density	35 A/cm ²
Current	25.2 A
Perveance	25.2 μ Perv
Emittance	9.81 mm-mrad

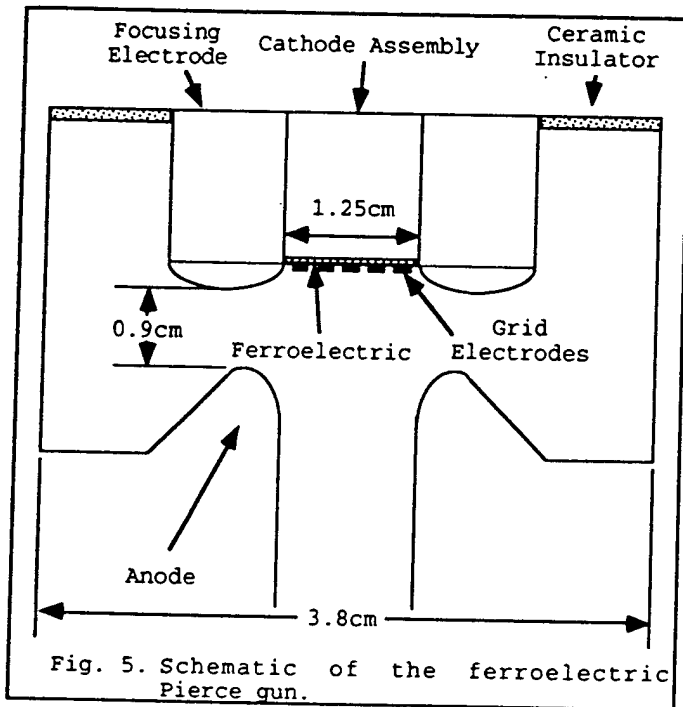


Fig. 5. Schematic of the ferroelectric Pierce gun.

The beam line will include diagnostics to determine beam emittance and energy spread for the ferroelectric cathode. The magnetic transport system consists of a quadrupole triplet and a spectrometer magnet. Phosphorus screens will be used to determine the beam spot, and hence emittance. The spectrometer magnet with a profilometer will determine the center energy and energy spread of the beam. A schematic of the beam line is given in Fig 6. The quadrupoles have a 4.06 cm effective length, 13 cm aperture, and field strength at the pole piece of 720G for a current of 1 A.

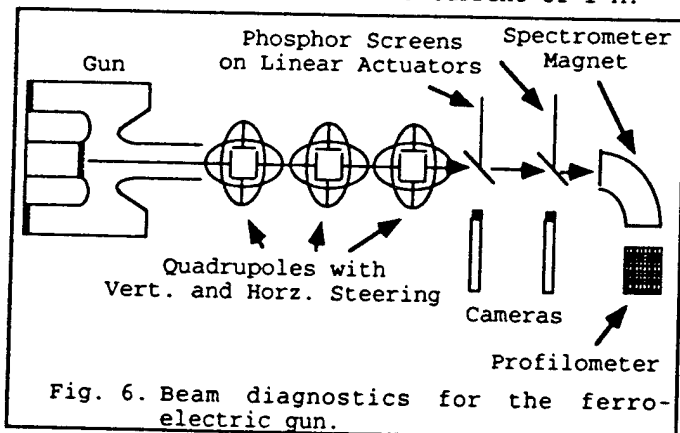


Fig. 6. Beam diagnostics for the ferroelectric gun.

7-Summary

A vacuum triode experiment has been assembled to study the emission from thin film and bulk ferroelectric materials. Significant problems have been encountered with mounting and connecting the bulk material to the triode. Redesign of the triode will include a stress-free holder for the ceramic and adhesion of the metallization to the samples will be improved. Fabrication of thin films has been performed, but the electrical characterization of this material is inconclusive at this time. The design of a low emittance Pierce gun using the ferroelectric cathode is complete as well as a design for a diagnostic system to determine beam quality. This work is expected to lead to improved performance of long pulse backward wave oscillators.

Acknowledgments

The authors wish to extend their gratitude to R. L. Terry and M. S. Anderson for help with the machining, assembly and maintenance of the experiment and to Bill Wilbanks for help in CHTM. The PLZT samples were supplied by Bruce Tuttle of Sandia National Laboratories and Jay Saxton of Motorola (Ceramic Products Division).

References

- [1] H. Gundel, J. Handerek and H. Reige, "Time-dependent electron emission from ferroelectrics by external pulsed electric fields," *J. Appl. Phys.* **69**, (2), pp. 975-982, (1991).
- [2] H. Gundel, H. Reige and E. J. N. Wilson, "Copious Electron Emission From PLZT Ceramics with a High Zirconium Concentration", *Ferroelectrics*, **100**, pp. 1-16 (1989).
- [3] J. D. Ivers, L. Schachter, J. A. Nation, G. S. Kerslick and R. Advani, "Electron-beam diodes using ferroelectric cathodes," *J. Appl. Phys.* **73**, (6), pp.2667-2671, (1993).
- [4] H. Gundel, "Electron Emission by Nanosecond Switching in PLZT," *Integrated Ferroelectrics*, **2**, pp. 207-220 (1992).
- [5] H. Gundel (private communication, 1993)
- [6] J. C. Burfoot and G. W. Taylor, *Polar Dielectrics and Their Applications*, Los Angeles: University of California Press, 1979.

Repeatable electron emission from (Pb,La)(Zr,Ti)O₃ ferroelectric cathodes using direct-current reset

T. C. Cavazos, W. L. Wilbanks, C. B. Fleddermann, and D. A. Shiffler
*Electrical and Computer Engineering Department, University of New Mexico,
Albuquerque, New Mexico 87131*

(Received 14 March 1994; accepted for publication 12 September 1994)

The use of ferroelectric (Pb,La)(Zr,Ti)O₃ as a cathode material is investigated. It has been suggested in the literature that by rapidly changing or reversing the spontaneous polarization in the ferroelectric, a large charge imbalance can be produced at the surface of the material. The field from this charge imbalance extracts bound carriers from the cathode. An approach to achieving this polarization change by using a negative bias field to preset the material prior to switching is discussed in this letter. This bias field can also be used to control the bound surface charge on the material. Emission currents on the order of 100 mA are observed and the emitted charge is on the order of 30 nC. Measurable emission occurs only when the material is driven into saturation. © 1994 American Institute of Physics.

Ferroelectric cathodes have attracted interest as electron emitters for a variety of applications.¹⁻⁴ Such cathodes have been shown to be capable of large electron emission currents in excess of the Child-Langmuir space charge limited current.¹⁻⁴ Further, the cathodes are ceramics, can operate in low or high vacuum, and do not require a heater. Previous results have demonstrated electron emission from samples which have been prepoled by slowly cooling the material from above the Curie temperature in the presence of an electric field.¹⁻⁴ This letter describes research done to characterize the emission process from (Pb,La)(Zr,Ti)O₃ (PLZT) on which no macroscopic prepoling was performed. A technique for using a bias voltage to control the emission process is introduced.^{5,6} Our results show that the emission process depends upon the initial state of the cathode material and that measurable emission occurs only when the material is near the saturation polarization. The ultimate goal of this work is to develop a new class of cathodes for microwave tubes as well as other vacuum electronic and microelectronic devices.

The experimental setup consists of a ferroelectric sample placed in the triode configuration shown in Fig. 1. A gold circular grid, 1.27 cm in diameter, with 20% transmission forms the emitting surface on top of the PLZT wafer. The thickness of the wafer is 0.33 mm and the grid and plate are separated by 2.7 cm. The cathode contact on the back of the wafer is grounded. The triode is evacuated to 10⁻⁹ Torr with an ion pump. A bias voltage is applied to the grid to produce a preset dipole moment in the sample and the pulsed coercive field is applied through a coupling capacitor. In this manner a charge imbalance is produced at the surface by rapidly reversing the polarization. A dc voltage of up to 20 kV is connected between the plate and the cathode contact. Current viewing resistors (CVRs) provide measurements of the grid current and plate current with voltage measurements obtained using resistive dividers.

For these experiments commercial grade PLZT 9/65/35 was used. The surface was polished to a quality suitable for electro-optics applications and had no macroscopic polarization. Figure 2 shows a sample hysteresis curve taken at 60 Hz excitation frequency. The remanent polarization is 1.5

μC/cm² while the coercive electric field is 4 kV/cm. At saturation, the polarization P_{sat} , is about 4.5 μC/cm² corresponding to an electric field E_{sat} , of 12 kV/cm. Pulsed measurements show little deviation in E_{sat} and P_{sat} from the 60 Hz ac values.

In the experiments outlined in this letter, the conditions for electron emission are obtained by rapidly reversing the polarization of the material. Initially, a bias voltage is used to produce a known polarization within the material and this field is reversed by pulse charging the polar dielectric with a transistor drive (see Fig. 1). This configuration allows one to change the initial position of the material on the hysteresis curve prior to the application of the forward drive. Therefore, control of the state of the cathode in a known and easily quantified fashion is possible. Experiments were performed with no bias voltage and with a bias voltage present. When no bias voltage was applied, current emission was erratic, although when emission did occur it happened at roughly the 100 mA level. When preset with a bias voltage, current at the 100 mA level was seen for every grid pulse. Thus, it can be concluded that the bias voltage positioned the ferroelectric in the correct state for emission.

Figure 3 shows the grid voltage and grid current and Fig. 4 shows plate current during two typical shots with a bias voltage present. Note the change in slope of the grid voltage

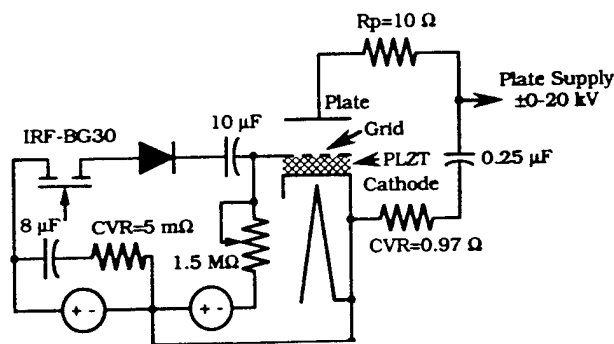


FIG. 1. Triode circuit with a solid state grid drive.

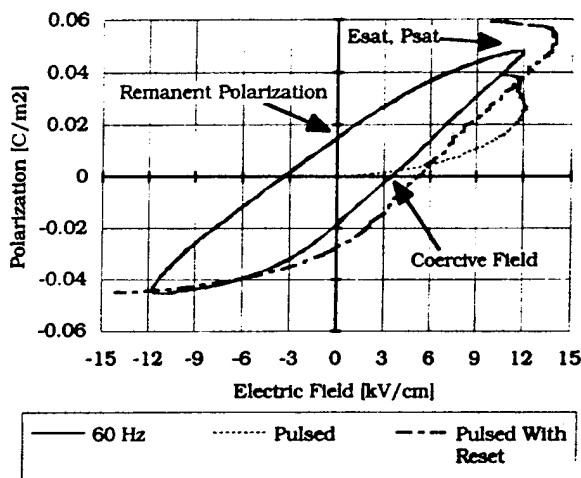


FIG. 2. Hysteresis of 965/35 PLZT wafer for ac and pulsed excitation.

as the ferroelectric saturates. From these traces, one can see that the leading edge of the emission current pulse begins just before the ferroelectric is saturated and measurable emission ends as the material comes out of saturation. Hence, the electron emission occurs during a nonlinear portion of the hysteresis curve where the relative dielectric constant switches from a maximum value to a saturation value close to one.

The charge emitted from the PLZT versus the applied electric field at the grid is plotted in Fig. 5. Ten measurements were taken at peak electric fields ranging from 6 to 14 kV/cm and the results are plotted with a best fit line. The emitted charge is measured by integrating the current to the plate. The graph indicates that more charge is emitted as the field at the grid increases and that there is a threshold field of about 8 kV/cm below which no charge is emitted. It is important to note that for each case, the reverse field is equal in magnitude to the forward field. In other words, the PLZT is excited from $-E_{\text{sat}}$ to $+E_{\text{sat}}$ during the grid pulse. The bound surface charge that is available for emission is determined by the magnitude of the initial polarization, which is proportional to $-E_{\text{sat}}$. The graph in Fig. 5 suggests a strong link between the bound surface charge and the charge emitted. As

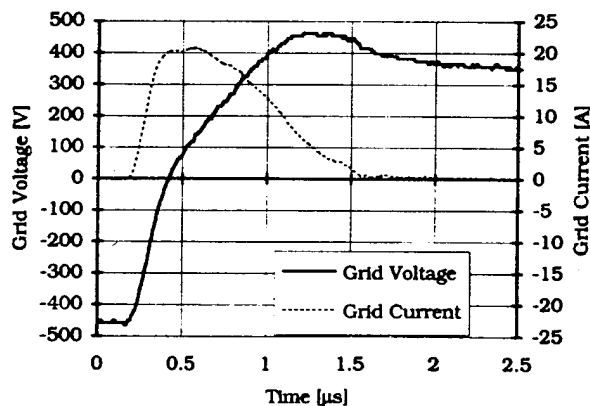


FIG. 3. Excitation voltage and current at the grid.

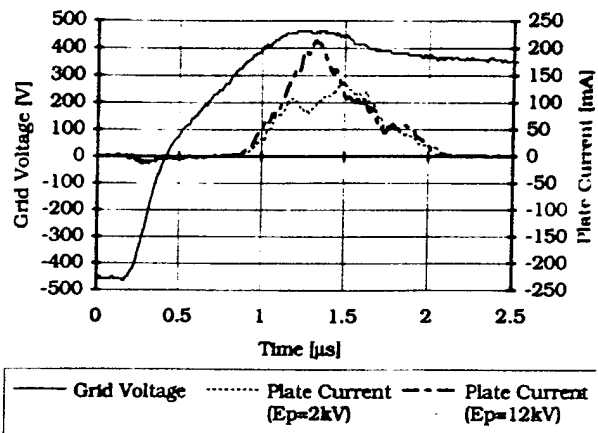


FIG. 4. Two typical plate current wave forms for plate voltages of 2 and 12 kV plotted with the grid voltage vs time.

the field applied to the grid increases, the spread in the measured emitted charge increases. This effect correlates with variations in the width of the emitted current pulse. Although the current pulse begins consistently as the ferroelectric saturates, the emission interrupts irregularly as the material comes out of saturation.

These experiments have demonstrated several characteristics of 9/65/35 PLZT emission. First, the initial state of the PLZT clearly affects the emission process since the current depends on the bias voltage. To demonstrate this observation, a pulsed hysteresis curve for the no bias case is included in Fig. 2. The slope and position of the curve at the end of the pulse suggest that the material is switching from remanence back to saturation. Under these conditions, emission from the PLZT was sporadic. The pulsed hysteresis curve for the negative dc bias case more closely matches the bottom-half of the 60 Hz P - E curve. With this excitation, regular emission is observed. Second, emission can be achieved by using a bias voltage to set the initial macroscopic polarization. Furthermore, by changing the bias, one can change the emitted charge. Finally, measurable emission occurs only when the ferroelectric becomes saturated, or in other words, when the rate of change of the relative dielectric constant with respect to the applied electric field is a maximum. The introduction of the bias potential is an important addition to ferroelectric cathodes. For cathodes with no initial macroscopic polarization, one can now effectively gate the charge as well as

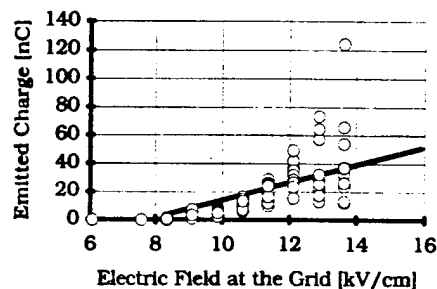


FIG. 5. Total charge emitted from the PLZT vs the field applied to the grid.

change the state of the cathode material. By using the bias voltage, it is shown that the emission does not require a sample with an initial macroscopic polarization. A change or reversal of the polarization induced strictly by applied electric fields is sufficient to achieve emission. These results also indicate that the emitted charge depends on the initial polarization. The ferroelectric cathode thus comprises a charge gated source. This behavior is different from most other cathodes.

The authors wish to thank Dr. Duane Dimos of Sandia National Laboratory and Jay Saxton of Motorola, Inc. for supplying the bulk PLZT used in this study. The authors

extend their thanks to Lee Terry of UNM for experimental support and Dr. J. Gahl and Dr. E. Schamiloglu for their assistance. This research is supported by AFOSR Grant No. F49620-94-1-0087DEF.

- ¹H. Gundel, J. Handerek, and H. Riege, *J. Appl. Phys.* **69**, 975 (1991).
- ²J. D. Ivers, L. Schachter, J. A. Nation, G. S. Kerslick, and R. Advani, *J. Appl. Phys.* **73**, 2667 (1993).
- ³L. Schachter, J. D. Ivers, J. A. Nation, and G. S. Kerslick, *J. Appl. Phys.* **73**, 8097 (1993).
- ⁴S. P. Bugaev and G. A. Mesyats, *Zh. Tekh. Fiz.* **37**, 1855 (1967).
- ⁵J. Asano *et al.*, *Jpn. J. Appl. Phys.* **32**, 4284 (1993).
- ⁶H. Gundel and A. Meineke, *Ferroelectrics* **146**, 29 (1993).
- ⁷H. Gundel, *Integrated Ferroelectrics* **2**, 207 (1992).

Investigation of Electron Emission from Bulk (Pb,La)(Zr,Ti)O₃ Ferroelectric Ceramics*

T. Cavazos, W. Wilbanks, C. Fleddermann, D. Shiffler

Electrical and Computer Engineering Department
University of New Mexico
Albuquerque, NM 87131

Abstract

Improvements in cathode technology represent one means of enhancing high power microwave tube performance. Of particular interest are low temperature cathodes which provide high current density electron beams. Our research focuses on the application of ferroelectric materials as an electron source. We are investigating two competing theories to explain the mechanism of emission from the material. The first method invokes a large charge imbalance induced by rapidly changing the polarization of the material (1). This charge imbalance accelerates screening charges (electrons) into the A-K gap. The second theory stipulates that an intense electric field at the periphery of the grid electrode vaporizes metallic protrusions of the grid (2). These explosions provide carriers as well as neutralize the space charge of the cathode.

Experiments are conducted using a demountable high vacuum triode with bulk (300 μm - 1 cm) (Pb,La)(Zr,Ti)O₃ (PLZT). The ferroelectric PLZT samples under test are gridded with an evaporated gold film which is patterned with circular apertures. This grid is excited by a solid state driver which erects a field of 15 kV/cm in about 1 μs . A DC bias voltage is used to reset the polarization of the material after each shot. Preliminary results indicate that this reset voltage greatly enhances the reliability of the electron emission. A DC voltage (up to ± 20 kV) applied to the anode accelerates any carriers liberated from the material. Hysteresis measurements are also conducted *in situ* to determine the dielectric properties of the candidate materials. Preliminary results of these experiments are presented.

Introduction

The copious emission of electrons from ferroelectrics has attracted interest in the use of these materials as cathodes in a variety of applications (1-5). Since these emitters are ceramics, they can be operated in high or low vacuum. The materials require little or no heating and have been shown to be capable of electron emission currents in excess of the Child-Langmuir space charge limited current (1-5). Recent results have demonstrated electron emission from samples which possess a macroscopic electric polarization obtained by prepoling the material (1-5). Ferroelectric materials are prepoled by heating the material past the Curie Temperature and

slowly cooling the material back through the transition boundary with a poling field applied to the dielectric. This paper describes the emission from (Pb,La)(Zr,Ti)O₃ (PLZT) in samples with no macroscopic pre-poling. A technique is presented for using a bias voltage to control the emission process (6-7). The results of these experiments indicate that by changing the initial polarization of the material the emission process can be controlled. Furthermore, measurable emission occurs only when the material is near the saturation polarization. These cathodes are capable of repetition rate operation.

Experiment

The experimental setup is shown in Fig. 1. The ferroelectric sample is placed in a triode configuration that is evacuated to 10^{-9} Torr. The grid and plate of the triode are separated by 2.7 cm. A gold circular grid, 1.27 cm in diameter, with 20% transmission forms the emitting surface on the front of the PLZT wafer; the wafer thickness is 0.33 mm. The contact on the back of the wafer is grounded for these experiments. A bias voltage is applied to the grid to produce a preset dipole moment in the sample. The pulsed coercive field is applied to the grid through a coupling capacitor. A charge imbalance at the cathode surface is produced by rapidly reversing the polarization through the application of the coercive field. An DC voltage of up to 20 kV is connected between the plate and the cathode contact. The grid and plate currents are measured using current viewing resistors (CVRs) and the plate current is determined using resistive dividers.

For these experiments, commercial grade PLZT 9/65/35 was used. The surface was polished to optical quality with no initial macroscopic polarization. Fig. 2 shows a sample hysteresis curve taken at 60 Hz excitation frequency. The remanent polarization is $1.5 \mu\text{C}/\text{cm}^2$ while the polarization at saturation, P_{sat} , is $4.5 \mu\text{C}/\text{cm}^2$. The coercive electric field is 4 kV/cm with the corresponding saturation electric field, E_{sat} , being 12 kV/cm. Pulsed measurements on the time scale used for the experiment show little deviation in E_{sat} and P_{sat} from the 60 Hz values.

Application of Reset

To obtain electron emission, the polarization of the ferroelectric must be rapidly reversed. A known polarization is

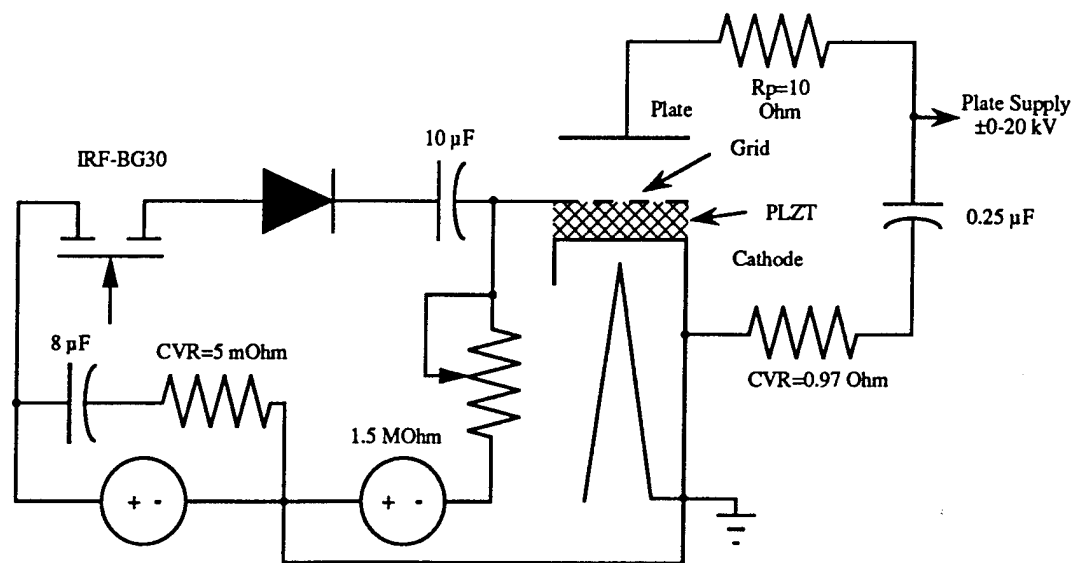


Fig. 1. Vacuum triode circuit with FET excitation circuit.

set in the wafer using the bias voltage. This field is then reversed by pulse charging the polar dielectric with the transistor drive shown in Fig. 1. Using this technique, the initial state of the ferroelectric can be changed in a quantifiable fashion prior to the application of the forward drive voltage.

Experiments have been performed with no bias voltage (no initial polarization) and with a bias voltage present. In the case of no bias voltage, emission was erratic. When performing experiments were repeated with the bias voltage, current was seen for every grid pulse. The currents measured were on the order of 100 mA. Thus, it can be concluded that the bias voltage placed the ferroelectric in the correct state for

emission.

The grid voltage and current are shown in Fig. 3 and the plate current during two typical shots in which a bias voltage was present is shown in Fig. 4. As the ferroelectric saturates, there is a change in the rate of rise of the grid voltage. This change corresponds to the change in the dielectric constant of the ferroelectric as the voltage exercises the P-E curve. The emission current pulse begins just before the ferroelectric saturates and ends as the material comes out of saturation. These results suggest that the electron emission occurs during a nonlinear portion of the hysteresis curve in which the relative dielectric constant of the material switches from its maximum value to a saturation value close to one.

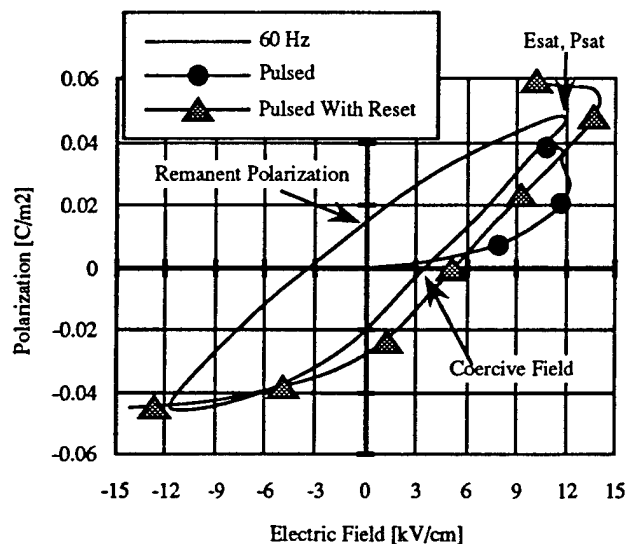


Fig. 2. Hysteresis curve for 9/65/35 PLZT material for pulsed and AC excitation.

The charge emitted from the PLZT into the vacuum

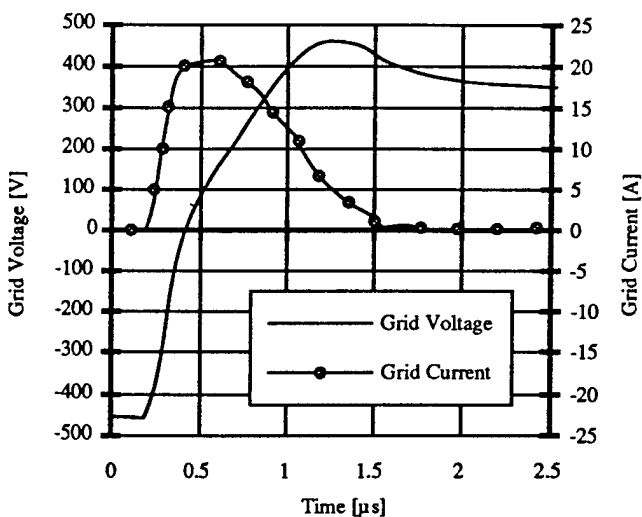


Fig. 3. Excitation current and voltage at the grid electrode.

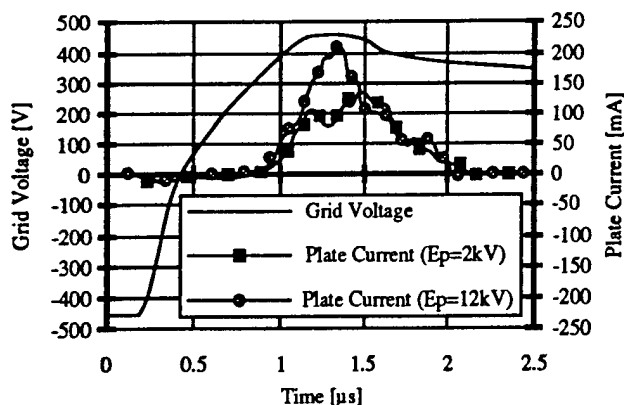


Fig. 4. Typical plate current waveforms for accelerating voltages of 2 kV and 12 kV plotted with the grid voltage versus time.

region was measured versus the applied field at the grid. These measurements are plotted with a best fit line in Fig. 5. For each case, ten measurements were taken at peak electric fields ranging from 6-14 kV/cm and the bias field is equal to the magnitude of the pulsed field. Several features of ferroelectric emission are evident from this figure. First, more charge is emitted as the field at the grid is increased. Next, a threshold field of about 8 kV/cm exists below which no charge is emitted. This threshold field is about halfway between the coercive and saturation electric fields. During each cycle, the PLZT is excited from $-E_{sat}$ to $+E_{sat}$ during the grid pulse. Since the initial bound surface charge depends upon $-E_{sat}$, Fig. 5 suggests a strong link between the bound surface charge (which is equal to the initial polarization) and the charge emitted to the plate. Finally, note that as the grid field increases, the spread in the measured emitted charge increases. This effect corresponds to variations in the width of the emitted current pulse. While the current pulse begins consistently as the ferroelectric saturates, the trailing edge of the emission occurs irregularly as the material comes out of saturation.

The ferroelectric material has also been operated in a repetition rate mode at up to four Hertz. The repetition rate was limited to prevent damage to the sample. The current in each

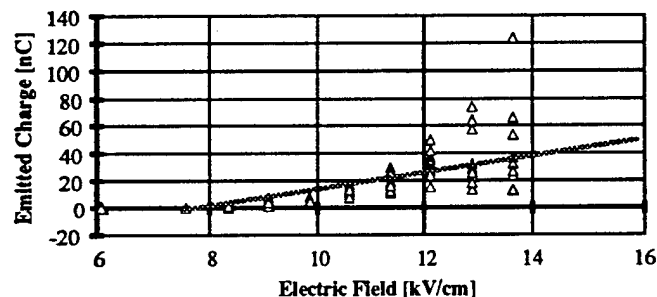


Fig. 5. Total charge emitted from the ceramic versus the peak field applied to the grid.

pulse remained at the level seen in the single shot experiments, or about 100 mA. Throughout the course of the testing, no conditioning effects were observed. The lifetime of the cathodes was limited by arcs in the grid-plate region. When an arc occurred, the triode would "latch on", which caused the ferroelectric to be severely damaged.

Summary of Results

These experiments have demonstrated several characteristics of 9/65/35 PLZT emission. First, the emission process is strongly dependent on the initial polarization of the cathode. This initial state is varied using the bias voltage. A pulsed hysteresis curve for the no-bias case plotted in Fig. 2 to demonstrate this observation. At the end of the pulse, the slope and position of the curve indicate that the material is switching from remanence to saturation. As stated above, emission was erratic under these conditions. The hysteresis curve for the pulsed excitation with negative DC bias more closely matches the 60 Hz P-E curve. Under these conditions, the emission was detected on every shot. Secondly, a bias voltage can be used to control the emission process. The effect of the bias is to change the bound surface charge and hence the available screening charges on the sample. Therefore, by changing the bias, the quantity of emitted charge can be changed. Finally, measurable emission is seen only when the ferroelectric becomes saturated. In other words, emission occurs when the rate of change of the relative dielectric constant with respect to the applied electric field is a maximum.

Future Experiments

A second Ion pump has been added to differentially pump on the anode. This should improve the grid-anode vacuum and reduce the inclination of arcs. The sample holder has been redesigned to limit the mechanical stresses on the material under test. A thicker material (1 mm) composed of lead/zirconium/titanium (PZT) will be tested next. This is a "harder" ferroelectric material with a coercive field of 8 kV/cm. The peak fields necessary to drive this material into saturation is on the order of 25 kV/cm. To achieve higher peak voltages on the thicker samples, a new driver has been developed. The new circuit directly couples the DC bias field to the grid and the reversing field is coupled with a pulse transformer.

Conclusions

The utilization of a bias potential is an important addition to the operation of ferroelectric cathodes. The application of the bias allows the charge to be gated in a quantifiable fashion. By using the bias voltage, it is shown that the emission does not require a sample with an initial macroscopic polarization. It is sufficient merely to reverse

the polarization using an applied electric field. These results also indicate that the emitted charge is related to the initial polarization. A biased ferroelectric cathode has thus been demonstrated as a gated source which can be operated in a repetition rate mode.

Acknowledgments

The authors wish to thank Dr. Duane Dimos of Sandia National Laboratory and Jay Saxton of Motorola, Inc. for supplying the bulk PLZT used in this study. The authors extend their thanks to Lee Terry of UNM for experimental support and Drs. J. Gahl and E. Schamiloglu for their assistance. This research is supported by AFOSR grant #F49620-94-1-0087DEF.

References

- (1.) H. Gundel, J. Handerek, and H. Riege, "Time-dependent electron emission from ferroelectrics by external pulsed electric fields." *J. Appl. Phys.*, vol. 69, pp. 975-982, 15 January 1991.
- (2.) S. P. Bugaev and G. A. Mesyats, "Study of the mechanism of a pulsed breakdown over the surface of a dielectric in vacuum." *Zh. Tekh. Fiz.*, vol. 37, pp. 1855-1960, 1967
- (3.) J. D. Ivers, L. Schachter, J. A. Nation, G. S. Kerslick, and R. Advani, "Electron-beam diodes using ferroelectric cathodes." *J. Appl. Phys.*, vol. 73, pp. 2667-2671, 15 March 1993.
- (4.) L. Schachter, J. D. Ivers, J. A. Nation, and G. S. Kerslick, "Analysis of a diode with a ferroelectric cathode." *J. Appl. Phys.*, vol. 73, pp. 8097-8110, 15 June 1993.
- (5.) H. Gundel, "Electron Emission by Nanosecond Switching in PLZT." *Integrated Ferroelectrics*, vol. 2, pp. 207-220, 1992.
- (6.) H. Gundel and A. Meineke, "First Simultaneous Observation of Electron Emission From and Switching Current Transient in PZT Ferroelectric Ceramics." *Ferroelectrics*, vol. 146, pp. 29-35, 1993.
- (7.) J. Asano, S. Iwaski, M. Okuyama, Y. Hamakawa, "Electron Emission from PZT Ceramic by External Pulsed Electric Fields -Pulse Voltage Dependence of Emitted Charge-." *Jpn. J. Appl. Phys.*, vol. 32, pp. 4284-4287, September 1993.

Appendix F: Paper in Print Pertaining to Suppression of Vacuum Breakdown

Suppression of vacuum breakdown using thin-film coatings

C. S. Mayberry, B. Wroblewski, E. Schamiloglu, and C. B. Fleddermann

Department of Electrical and Computer Engineering, University of New Mexico,
Albuquerque, New Mexico 87131

(Received 27 May 1993; accepted for publication 17 June 1994)

Thin-film metal and metal oxide coatings ion sputter deposited onto the cathode electrode of a parallel-plate high-voltage gap were found to suppress electron emission in high vacuum. Electric fields as high as 60 kV/mm have been sustained across a 1 mm gap for pulse durations of 10 μ s. Lesser electric fields were sustained for pulse durations exceeding 10 ms. The behavior of 500 nm thick coatings was independent of the type of coating used, whereas the breakdown voltage for thinner coatings depended upon the material and the deposition conditions. The breakdown properties of various coatings, as well as a discussion of the suppression of electron emission is presented.

The ability to sustain large electric fields across metal electrodes in vacuum is an important consideration in pulsed power applications.¹ Previous researchers have attempted to improve the breakdown characteristics of metal electrodes by coating them with various dielectrics including epoxy, oil, and polymers.¹⁻⁶ Although these coatings led to improved performance, little work was done to understand the mechanisms that increase the threshold voltages for initiating breakdown.

This paper describes the results of an experimental investigation to increase the threshold breakdown voltages and sustained pulse durations across planar stainless-steel electrodes in high vacuum ($P_{\text{base}} < 4 \times 10^{-8}$ Torr). A solid anode electrode and thin-film coated 80% transparent mesh cathode were used. Films were deposited on the cathode mesh using ion-beam sputter deposition. The electrode material and the experimental configuration were selected as part of a study of a planar liquid metal ion source.⁷ In addition, the choice of coating materials was motivated by initial studies of coatings for use in high-power microwave sources.⁸

The experimental apparatus, shown in Fig. 1, consists of an A-K gap in a stainless-steel vacuum chamber. A cryogenic pump was used to achieve the base pressure. The anode is made of polished stainless steel, 2.54 cm square. The broad area cathode is an 80% transparent stainless-steel mesh. The cathode is adjustable over the anode to a minimum gap spacing of 1.00 ± 0.12 mm. A voltage pulse is applied to the anode from a 0.733 μ F capacitor through a spark gap switch. The pulse rise time is less than 1 μ s. The voltage pulse was terminated with a crowbar spark gap switch across the capacitor. The typical A-K gap used was 1 mm and voltages from 20 to 65 kV were applied. Additional information on the hardware can be found in Ref. 9.

A common theme of the various breakdown theories reported in the literature suggests that anything that can be done to blunt microprotrusions and to remove loose particles adhering to electrode surfaces should improve the breakdown characteristics of the gap. Toward that end we first polished the anode with a high-speed polishing wheel and jewelers rouge. (Of course this could not be applied to the delicate cathode mesh.) Both of the electrodes were washed with isopropyl alcohol, methanol, and finally with acetone.

After the electrodes were installed, the gap was sprayed with No. 40 synthetic air to remove any dust that may have settled on the surfaces. The intent of these procedures was to remove as many microparticles from the electrodes as possible, and to minimize the formation of monolayers of oxygen and water. The chamber was pumped down to a final pressure of 4×10^{-8} Torr before any voltages were applied. These procedures alone resulted in breakdown occurring at 30 kV/mm within 50–100 μ s.

There are a number of *in situ* conditioning processes that can be applied to reduce the emitted current from microstructures.^{2,6} The gap can be subjected to a series of increasing dc voltages, allowing the prebreakdown currents to decay over a span of approximately 30 min. Alternatively, glow discharge cleaning can be employed; this takes advantage of the sputtering action of low-energy ions to knock off layers of contaminants. Discharge cleaning was performed on our experiment with no noticeable improvements, as our vacuum was very good to begin with and this method is generally useful for removing contaminants which keep the chamber pressures high.

Another conditioning method was used on our experiment to recover lost performance after a breakdown. Examination of the individual wires in the cathode mesh using an environmental scanning electron microscope (ESEM) showed that a typical mesh wire has channels running along its axis; these grooves are most likely due to imperfections in the die used to pull the wire. The ESEM also showed that even after cleaning, several microparticles were still present on the wire. These imperfections led to prebreakdown at relatively low voltages. By reducing the applied voltage, increasing the pulse duration, and repeatedly pulsing the gap until breakdown no longer occurs, we were able to regain some of the performance of the gap prior to breakdown. This procedure is thought to blunt the microprotrusions and clean the surface, thus reducing electron emission levels.

The maximum electric field and pulse duration achieved without breakdown using the above procedures was 30 kV/mm for 100 μ s. A great advance over these results was made by sputter depositing thin-film coatings onto the cathode mesh. Figure 2 shows a comparison of the breakdown voltages for different coatings, all grown to a thickness of

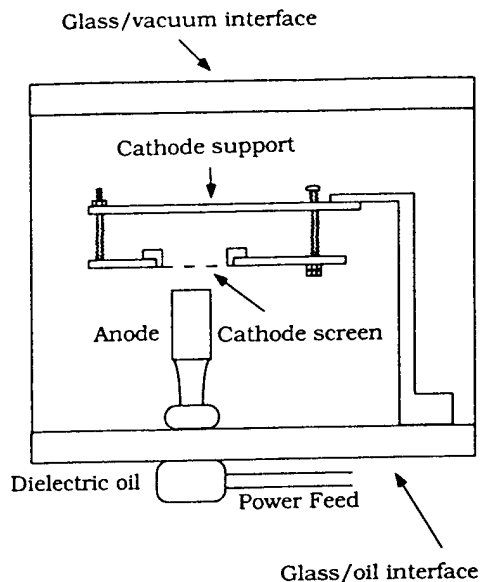


FIG. 1. Schematic of the experimental setup (not drawn to scale).

500 nm. Films were deposited using ion-beam sputtering with a 2.5 cm diameter Kaufman gun. Typically, the ion gun was run with a beam voltage of 750 V and a beam current of 30 mA. Metal films were deposited using an argon-ion beam, and oxides were deposited using mixed Ar/O₂ beams. Sputter targets were either metals or stoichiometric oxides, depending on the film to be deposited. The coatings in Fig. 2 are compared with a bare stainless mesh on the left. It is clear from the figure that coating the cathode increases the threshold breakdown voltage for all materials except TiN, and that TiO₂ and SnO₂ performed the best. All experiments described below were performed using TiO₂ coatings.

To determine whether the increase in the breakdown electric field after thin-film coating is due to burial of the microprotrusions left by the manufacturing process, SEM pictures were taken after the thin-film deposition process. The screens, as shown in Figs. 3(a) and 3(b), reveal a

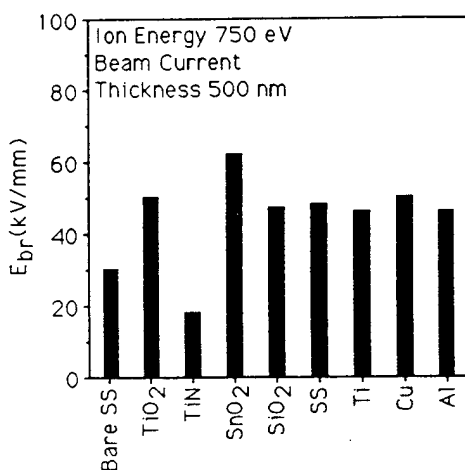


FIG. 2. Maximum breakdown electric fields for several types of ion-beam sputter-deposited coatings.

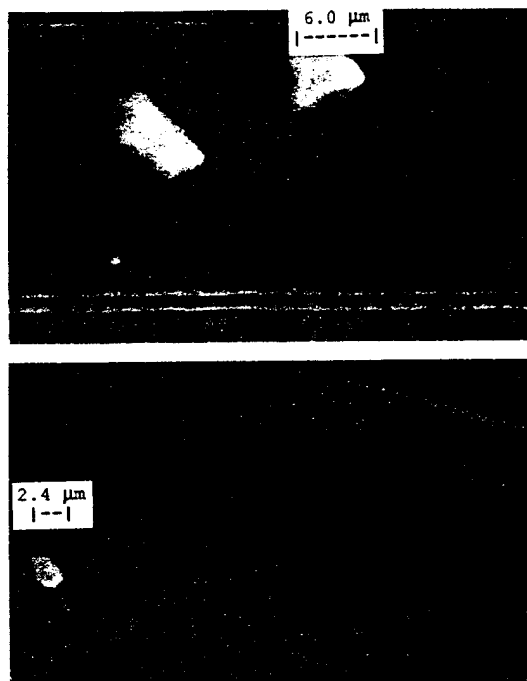


FIG. 3. SEM photographs of (a) a bare stainless-steel mesh and (b) mesh coated with 500 nm of sputter-deposited stainless steel.

smoother surface for the coated screen. The results obtained were repeatable and suggest that a sputter-deposited surface of approximately 500 nm thickness is smoother than the bare surface. All of these coatings achieved a peak electric field of about 50 kV/mm. We have found that there are a large variety of coatings (both metal and dielectric) which, when grown to at least 500 nm, yield a large increase in the breakdown electric field by creating a smoother surface, thus reducing electron emission from the cathode.

Thinner films (200 nm) showed a variation of breakdown electric field with a change in the deposition conditions. Specifically, we varied the oxygen content of the sputter gas mixture used during film growth, with all other ion-beam parameters held constant. Breakdown field as a function of oxygen content of the beam is shown in Fig. 4 for TiO₂ films. (Rutherford backscattering measurements on these films confirmed that all were stoichiometric TiO₂.) This plot indicates that the breakdown electric field varies markedly with oxygen content while a plot for a TiO₂ film at a thickness of 500 nm, also shown in Fig. 4, is independent of the deposition conditions. It is widely known that the index of refraction, grain size, and packing density of oxide films vary with the oxygen partial pressure during deposition, and that the index of refraction is indicative of changes in the latter two properties.^{10,11} We have measured the index of refraction of our deposited films as a function of oxygen content of the ion beam; our results agree with the experimental findings in Ref. 10. Therefore, it is apparent that the breakdown electric field for thin films (200 nm) is more sensitive to the film properties, while for 500 nm thick films, merely burying surface microprotrusions becomes the dominant mechanism in achieving the larger breakdown electric fields.

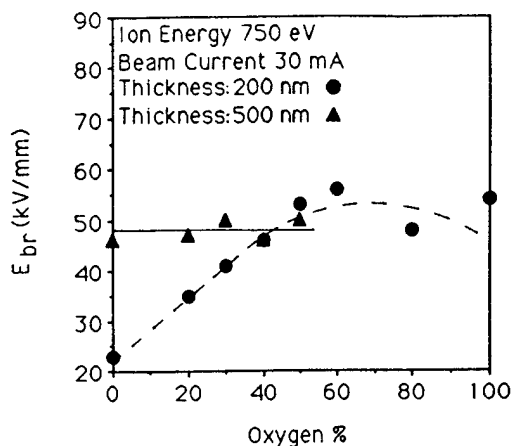


FIG. 4. Plot of breakdown electric field as a function of the oxygen content of the sputtering gas for film thicknesses of 200 and 500 nm.

The breakdown behavior of Ti/TiO₂ layered structures deposited on the cathode screen was also investigated. Two of this type of film were studied: one was a 100 nm thick pure titanium layer deposited on the screen, followed by a 100 nm thick TiO₂ layer (grown using 50% oxygen in the ion beam) for a total layer thickness of 200 nm; the other was a similar structure with 300 nm of Ti with 200 nm of TiO₂ for a total thickness of 500 nm. For the 300/200 film, the breakdown field was 52 kV/mm, which is comparable to the fields measured for 500 nm Ti and TiO₂ films. In this case the presence of the dielectric is insignificant as is expected for the thicker films, and the breakdown field increase is due to the burying of imperfections. However, the 100/100 film had a breakdown field of 44 kV/mm. This is significantly higher than the breakdown field for a 200 nm thick pure Ti film (the 0% oxygen value in Fig. 4), showing that for thin films where the effect of covering up cathode imperfections is not as significant, the presence of even a thin dielectric layer can cause measurable improvement in the breakdown behavior of the cathode.

The results of this study indicate that thin-film coatings of metals or metal oxides can yield a factor of 2 increase in the breakdown characteristics of parallel-plate stainless-steel electrodes in high vacuum. The study found that the breakdown electric field for 200 nm thick coatings was dependent on the grain size or packing density of the film, whereas the breakdown field for 500 nm thick coatings was independent of the material properties. To achieve the highest breakdown field, the oxygen content of the background gas should be 50% or higher for 200 nm thick films, or 500 nm thick films should be applied. It is important to note that these coatings are not robust. While some level of performance can be regained after a breakdown event, generally the coated cathode screen will have to be replaced if the application cannot tolerate a large variation in breakdown electric field.

The authors would like to thank Dr. V. I. Rakhovsky for useful discussions on the total voltage effect, and R. L. Terry for providing technical assistance with the experimental hardware. In addition, they would like to thank S. Droes for performing the Rutherford backscattering measurements. This research was supported by Sandia National Laboratories Contract No. 69-5698, and partially supported by AFOSR Grant No. F49620-92J-01 57P00001.

¹ See, for example, articles in *Proceedings of the 15th International Symposium on Discharges and Electrical Insulation in Vacuum*, edited by D. König (IEEE, Berlin, 1992), Catalog No. 92CH3191-2.

² R. V. Latham, *High Voltage Vacuum Insulation, The Physical Basis* (Academic, NY, 1981).

³ J. C. Anderson, *J. Vac. Sci. Technol.* **9**, 1 (1972).

⁴ E. W. Gray, *J. Appl. Phys.* **58**, 132 (1985).

⁵ G. B. Frazier, *Proceedings of the 2nd International Pulsed Power Conference* (IEEE, New York, 1979), p. 127.

⁶ R. J. Noer, *Appl. Phys. A* **28**, 1 (1982).

⁷ C. S. Mayberry, E. Schamiloglu, and G. W. Donohoe (unpublished).

⁸ D. Shiffler, T. Cavazos, L. Moreland, C. Fleddermann, J. Gahl, and E. Schamiloglu, *Bull. Am. Phys. Soc.* **37**, 1540 (1992).

⁹ C. S. Mayberry, M. S. thesis, University of New Mexico, 1993.

¹⁰ H. K. Pulker, G. Paesold, and E. Ritter, *Appl. Opt.* **15**, 2986 (1976).

¹¹ S. Schiller, G. Beister, W. Sieber, G. Schirmer, and E. Hacker, *Thin Solid Films* **83**, 239 (1981).